DEVELOPMENT OF GOLD NANOPARTICLE-BASED THERANOSTIC AGENTS FOR MOLECULAR IMAGING AND CANCER THERAPY

A Dissertation
Presented to
The Academic Faculty

by

Bo Pang

In Partial Fulfillment
of the Requirements for the Degree
Doctor of Philosophy in the
Wallace H. Coulter
Department of Biomedical Engineering

Georgia Institute of Technology
Emory University
May 2017

DEVELOPMENT OF GOLD NANOPARTICLE-BASED THERANOSTIC AGENTS FOR MOLECULAR IMAGING AND CANCER THERAPY

Approved by:

Dr. Qiushi Ren, Advisor
Department of Biomedical Engineering
Peking University

Dr. Zhifei Dai
Department of Biomedical Engineering
Peking University

Dr. Younan Xia, Co-Advisor
Department of Biomedical Engineering
Georgia Institute of Technology

Dr. Changhui Li
Department of Biomedical Engineering
Peking University

Dr. Mingyuan Gao
Institute of Chemistry
Chinese Academy of Science

Date Approved: March 3, 2017

ACKNOWLEDGEMENTS

I have received advice and support from a number of individuals during my Ph.D. study. First of all, I would like to thank my advisor, Professor Qiushi Ren, for his guidance and support, and for introducing me to the scientific community. In particular, I would like to express my gratitude to him for always being resourceful in both scientific research and my career development. I would like to express my deepest appreciation to my co-advisor, Professor Younan Xia, for providing me with valuable guidance, research ideas and discussions, as well as continuously encouragement to improve my work. The knowledge and skills I learnt from him have been proven to be extremely helpful. And the dedication as well as professionalism he represents will definitely encourage me through my whole career. I would also like to express my appreciation to Professor Dong Qin for her advice.

I have been fortunate to have the chances to collaborate with some excellent talents, without whom my research works might never be achieved. I would like to thank Professor Yongjian Liu at Washington University in St. Louis for his support in radiochemistry and nuclear imaging, Dr. Yongfeng Zhao for the discussion on experiment design, Professor Zhi-Yuan Li from Chinese Academy of Sciences for the theoretical simulations of UV-vis extinction spectra, Dr. Jiahe Tian from Chinese PLA General Hospital for his support in nuclear imaging instrumentation.

I would also like to express my gratitude to all group members who have inspired me along the graduate school. I would like to thank Dr. Yu Shrike Zhang, Dr. Wenying Liu and Professor Lei Zhang for general biomedical engineering, Professor Tianmeng Sun for *in vitro* experiments. I would like to thank Professor Yucai Wang, Aleksey Ruditskiy, Dr. Yi Wang,

Dr. Yiqun Zheng, Miaoxin Yang for their help on the syntheses of nanoparticles, Dr. Jinho Park for inductively coupled plasma mass spectrometry. I would also thank Xiangxi Meng and Kedi Zhou for their support to my experiment.

Finally, I would like to express my deepest appreciation to my parents, Jianguo Pang and Shufeng Liu, for their selfless love and support, as well as unwavering faith in me.

TABLE OF CONTENTS

LIST OF FIGURES

LIST OF ABBREVIATIONS

PET	Positron Emission Tomography
PET/CT	Positron Emission Tomography/ X-Ray C
SPECT	Single-Photon Emission Computed Tomography
SPECT/CT	Single-Photon Emission Computed Tomography/X-Ray CT
TEM	Transmission Electron Microscope
CTAB	Hexadecyltrimethylammonium Bromide
CTAC	Hexadecyltrimethylammonium Chloride
AA	Ascorbic Acid
LSPR	Localized Surface Plasmon Resonance
UV-vis-NIR	Ultraviolet-Visible-Near Infrared
PEG	Poly(Ethylene Glycol)
anti-EGFR	anti-Epidermal Growth Factor Receptor
DOTA	1,4,7,10-Tetraazacyclododecane-1,4,7,10-Tetraacetic Acid
CCR5	C-C Chemokine Receptor 5
RGD	Arg-Gly-Asp
SERS	Surface-Enhanced Raman Scattering
CCL5	Chemokine (C-C motif) Ligand 5
DAPTA	D-Ala1-Peptide T-Amide
PVP	Poly(Vinyl Pyrrolidine)
3D-FDTD	Three-Dimensional Finite-Difference Time-Domain
Radio-TLC	Radioactive Thin Layer Chromatography
DPBS	Dulbecco’s Phosphate Buffered Saline

MTT	3-(4,5-Dimethylthiazol-2-yl)-2,5-Diphenyltetrazolium Bromide
ICP-MS	Inductively Coupled Plasma Mass Spectrometry
%ID/g	Injected Dose per Gram of Tissue
EPR	Enhanced Permeation and Retention
SUV	Standard Uptake Value
^{18}F-FDG	^{18}F-Flourodeoxyglucose
H&E	Hematoxylin and Eosin
DMSO	Dimethyl Sulphoxide
DMEM	Dulbecco's Modified Eagle Medium
Radio-ITLC	Radioactive Instant Thin Layer Chromatography
PBS-T	0.1% Tween-20 in PBS
GM	Göppert-Mayer
CCK-8	Cell Counting Kit-8
DiO	3,3'-dioctadecyloxacarbocyanine, perchlorate
ICP-AES	Inductively Coupled Plasma-Atomic Emission Spectrometer
FPLC	Fast Protein Liquid Chromatography
MWCO	Molecular Weight Cut-off
ECM	Extracellular Matrix
EDC	(1-Ethyl-3-(3-Dimethylaminopropyl)Carbodiimide Hydrochloride)
NHS	N-Hydroxysuccinimide
PCM	Phase-Change Material

SUMMARY

This research explored the use of Au nanoparticles on molecular imaging and cancer theranostics, with focuses on the fabrication of new materials, the incorporation of new medical isotope, as well as new labeling and detecting techniques.

The first part focuses on the synthesis and characterization of PdCu@Au core-shell tripods and their application in cancer theranostics. Innovative radiolabeling technique was also developed to incorporate Cu-64 into the crystal lattice of the PdCu@Au tripods for improved radiolabeling stability. Novel biomarker of C-C chemokine receptor type 5 was selected to target triple negative breast cancer. With characteristic localized surface plasmon resonance in the near infrared range, positron emission tomography guided photothermal therapy was also demonstrated. In addition, the PdCu@Au tripods demonstrated a much brighter two-photon luminescence than that from Au nanorods, with a 3.6 ± 0.9 times larger two-photon action cross section and comparable quantum yield.

The second part focuses on the use of Au-199 as a new medical isotope for the improvement of imaging quality of single-photon emission computed tomography. With Au-199 incorporated into the crystal lattice of nanoparticles improved radiolabeling stability was demonstrated.

The final part demonstrated the use of Arg-Gly-Asp peptide-conjugated Au nanorods for radio-sensitization in radio therapy. This radio-sensitization effect was proofed to be the result of decreased expression level of $\alpha_v\beta_3$ integrin and increased G_2/M arresting in cell cycle.

CHAPTER 1. INTRODUCTION

Cancer poses a great threat to public health worldwide with increasing incidence and high mortality rate.[1] Though the spending on research and patient care increases dramatically in the past years causing growing burden to the society, the mortality rates have shown little improvement for patient with most types of cancer.[2] The newly developed therapeutics and combination of standard therapeutics could only provide modest contribution to the survival rate and patient's welfare.[2] On the other hand, statistics shows an improved survival rates when the cancer were diagnosed at an early stage.

Clinical imaging techniques are playing important roles in cancer diagnosis by providing precise positional and anatomical information that is critical to the treatment. However, the traditional anatomical imaging modalities could provide little biological information with unsatisfied sensitivity and selectivity, which brought difficulties to the diagnosis and staging of cancer.[3] Imaging modalities such as positron emission tomography (PET) and single-photon emission computed tomography (SPECT), possess the capability to reveal biological processes at cellular and molecular level, and were termed as molecular imaging modalities.[4] In combination with screening approaches, molecular imaging could help to detect the molecular alterations, which indicate the incidence of cancer, at its curable early stage. This technology also allows the evaluation and adjustment of treatment plans when the treatments are still in process. Imaging probes with high affinity in selecting molecular targets are needed in molecular imaging to generate and amplify the signals required for the imaging instrument.[4] In a typical imaging approach, engineered probes are introduced *via* systematic administration to circulate

through the entire body. By binding to the designed molecular targets at a high affinity, the probes could concentrate at the lesion enabling the detection of disease. Thus the design and development of novel molecular imaging probes would greatly affect the diagnoses on both the sensitivity and the selectivity.

Nanomedicine is a rapidly advancing field of research that is anticipated to bring in many new opportunities for more effective diagnosis and treatment of diseases.[5] In cancer nanomedicine, imaging probes and therapeutic agents are increasingly integrated with nanoparticles engineered with optimal sizes, shapes, and surface properties, to increase their solubility, prolong their blood circulation half-life, improve their biodistribution as well as targeting selectivity, aiming at the ultimately reduction of side effects. Engineered nanoparticles could serve as novel drug delivery system and theranostic platform, helping to solve a number of issues associated with conventional therapeutic agents, including their toxicity, nonspecific distribution, unsatisfied targeting capability, as well as poor water solubility.[5]

Among the different kinds of nanomedicine, Au nanoparticle-based nanomedicine possesses unique properties such as bio-inertness, readily tuned optical properties, as well as easily conjugated surface in addition to the shared merits across nanomedicine.[6] Many types of engineered Au nanoparticles have been demonstrated as platforms for various biomedical applications.[7] The usages of Au nanoparticles in various biomedical applications such as optical sensing, optical imaging, drug delivery, and cancer therapy have been demonstrated.[6] The use of Au nanoparticles for cancer theranostics in combination with traditional medicine has also been extensively investigated. Though these various kinds of biomedical applications have been reported for Au nanoparticles,

their application in radiology and nuclear medicine is still rarely reported, partially limited by the accessibility to the facilities and equipment.

The current research focuses on the improvement of the properties of nanomaterials, by synthesizing new nanomaterials with novel composition and morphology. With improved composition and morphology, nanomaterials could obtain better biodistribution profiles to effectively detect tumor at a lower dose. Nanomedicines are also developed as multi-function platforms capable of carrying out various tasks sequentially, to diagnose and treat cancer during the same course of treatment. In that way, the benefit of the nanomedicine could be multiplied, and the side effects could be relatively reduced, as lower doses would be needed for the same procedures.

Here, I selectively highlight some of the latest progresses in the field of Au nanoparticle-based nanomedicine with the focuses on their synthesis, optical properties, radiolabeling methods, as well as their applications in PET imaging, photothermal therapy and radiotherapy. The aim of this summary is to provide the reader with basic ideas on the current status, instead of a comprehensive review of this field.

1.1 Synthesis of Au Nanoparticles and Their Properties

The research of using Au nanoparticle for biomedical applications has experienced a rapid advancement as the result of the quick development of solution-phase syntheses of Au nanoparticles. Represented by the synthesis of conventional Au nanoparticle, Au nanorods, nanocages, and nanoshells, various kinds of Au nanoparticle could be prepared with well controlled size, shape at high purity (Figure 1.1).[6] The underlying mechanisms

to direct and control the growth of anisotropic Au nanoparticles were also proposed and studied.

1.1.1 Synthesis of Au Nanoparticles

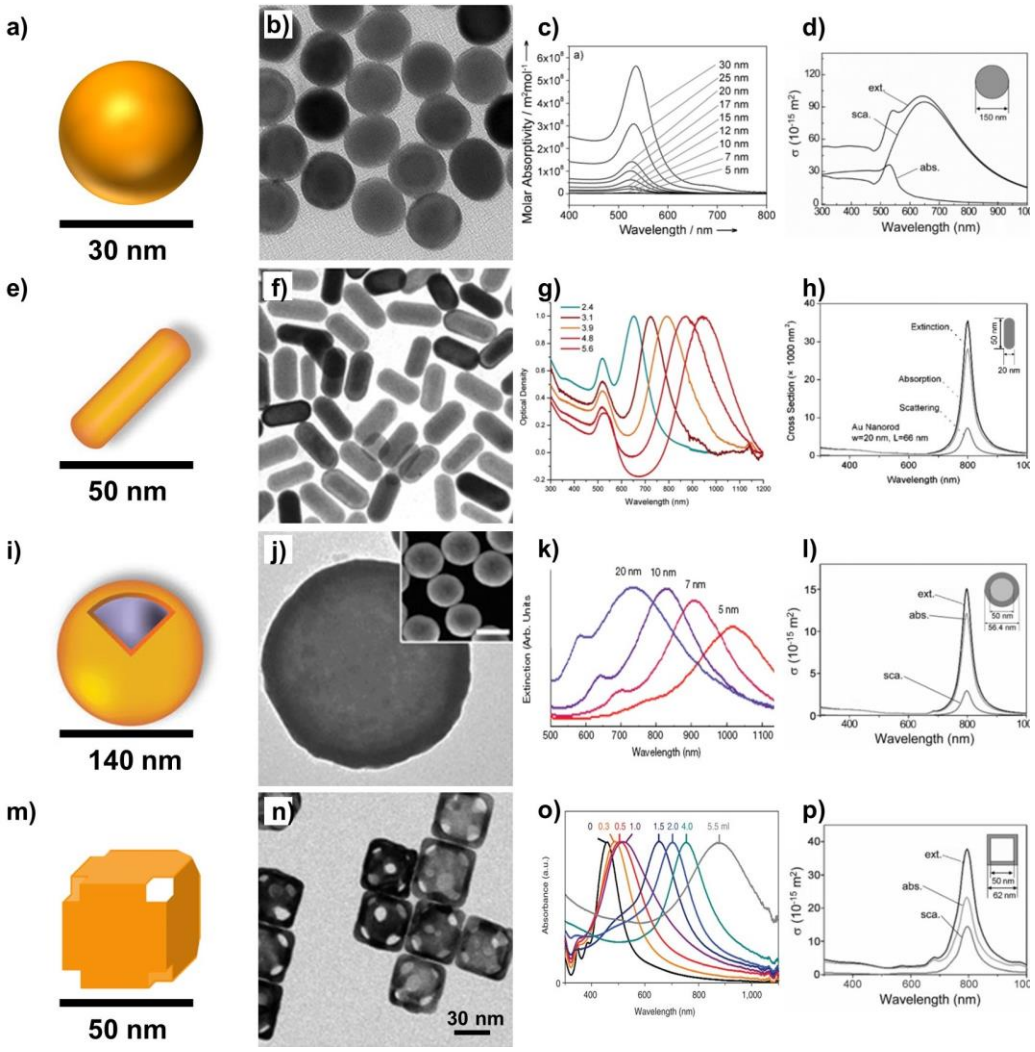

Figure 1.1. A schematic diagram illustrating the structure of a) Au nanospheres, e) Au nanorods, i) Au nanoshells,[8] and m) Au nanocages. The transmission electron microscope (TEM) image of b) Au nanopheres,[9] f) Au nanorods,[10] j) Au nanoshell,[11] and n) Au nanocages.[12] Experimental UV-vis spectra results showing the capability of tuning the spectrum of c) Au nanospheres,[9] g) Au nanorods,[13] k) Au nanoshell,[14] and o) Au nanocages.[15] The simulation of localized surface plasmon of d) Au nanospheres,[16] h) Au nanorods, l) Au nanoshells, and p) Au nanocages.[17]

Conventional Au nanoparticles are the first kind of Au nanoparticle ever developed, tracing back to the discovery of "fine particles" by Michael Faraday.[18] They are typically polycrystalline nanostructure with quasi-spherical shapes. With the absence of perfect-shaped single crystal Au nanospheres, conventional Au nanoparticles were also termed as "Au nanospheres" for a long period of time. Currently, conventional Au nanoparticles are prepared by the Turkevich method or Brust method and their variations. In the Turkevich method, $HAuCl_4$ is reduced in an aqueous solution by sodium citrate, which also served as the colloidal stabilizer.[19, 20] By varying the molar ratio of $HAuCl_4$ to sodium citrate, the final product could be prepared at different sizes with reasonable uniformities in size distribution and morphology. But these uniformities are largely affected by the pH value or the sequence for introducing the reagents.[21, 22] In the Brust method, $HAuCl_4$ is reduced by $NaBH_4$ in an organic phase (typically toluene) with thiol (typically dodecanethiol) as capping agent.[23] With the help of phase-transfer agent (typically tetraoctylammonium bromide) $HAuCl_4$ is dispersed in the organic phase into reverse micelles. The reverse micelles could limit the growth of Au nanoparticles and stabilize the as prepared nanoparticle from aggregation. The size of the Au nanoparticles produced by this synthesis is controlled by the molar ratio between $HAuCl_4$ to the thiol, but affected by the temperature and aging time. Though the size of the conventional Au nanoparticles can often be tuned in a wild range (upto 180 nm) by additional rounds of seed-mediated growth after the initial synthesis, the uniformity of size and morphology is still not ideal.[24]

Recently, our group established the synthesis of single crystal Au nanospheres with well-defined circular shape.[9, 25] In this synthesis, a seed-mediated growth approach is employed with initial seeds prepared by reducing $HAuCl_4$ with $NaBH_4$ in the presence of

hexadecyltrimethylammonium chloride (CTAC). To prepare Au nanospheres of upto 17 nm, additional Au is coated by subjecting the initial seeds to additional rounds of overgrowth in the solution containing $HAuCl_4$, CTAC, and ascorbic acid (AA). By increasing the rounds of overgrowth while controlling the reaction rate by the dropwise addition of $HAuCl_4$, Au nanospheres of upto 150 nm could be synthesized with a narrow size distribution and good uniformity in morphology.

The synthesis of anisotropic Au nanoparticles has long been a heated research topic, as the growth of anisotropic structure is difficult to be initiated and controlled. Till recently, many kinds of method have been proposed for the synthesis of Au nanorods.[6] Among the different methods, the seeded-growth approach has become the most popular approach for its simplicity in procedure and high product uniformity. Initially developed by Murphy and co-workers and improved by El-Sayed and Nikoobakht, the typical synthesis involved two major steps: the preparation of initial seeds and the overgrowth of initial seeds to nanorods.[26, 27] In the original protocol developed by Murphy and co-workers, the initial seeds are prepared by reducing $HAuCl_4$ with $NaBH_4$ in the presence of sodium citrate as colloidal stabilizer.[26] In the modified protocol, the sodium citrate is substituted by hexadecyltrimethylammonium bromide (CTAB) for a better control of size and crystallinity of the seeds.[27] The as prepared initial seeds will then be subjected to overgrowth in the growth solution typically containing $HAuCl_4$, AA, CTAB, and $AgNO_3$. The aspect ratio could easily be tuned by varying the molar ratio of $HAuCl_4$ to the initial seeds and the amount of Ag^+ presented in the system. Additional rounds of overgrowth could also be employed for the preparation of Au nanorods with higher aspect ratio.[27]

The Au nanoshell is the first kind of Au nanoparticle developed with tunable optical properties. The synthesis of Au nanoshells involves the coating of Au layer on a dielectric core material. As the makes of dielectric core and Au layer are so different, the surface modification of core materials and the attachment of Au seeds become the critical step in the synthesis. In the well-known synthesis developed by Halas and co-workers, SiO_2 colloidal spheres prepared by the Stöber method are used as core materials for the synthesis.[28] An amino-terminated saline (typically aminopropyltriethoxysilane) is introduced to functionalize the surface of SiO_2 with amino groups for the easy attachment of Au nanoparticle seeds. These attached Au seeds could serve as the nucleation sites for further deposition of Au via chemical reduction. A mild reductant would typically be used to control the rate of the reaction to a low level. With more Au deposited on the nucleation sites, the isolated Au patches become to coalesce and finally generate a uniform shell. It is worth mention that the Au nanoshells still possess a solid core/shell structure that is less favorable for biomedical applications.

Different from the Au nanoparticles mentioned above, Au nanocages are featured with hollow interior and porous walls. This features provides Au nanocages with tunable localized surface plasmon resonance (LSPR) peaks, and could be used for the delivery and controlled release of drug.[29] The synthesis of Au nanocages was pioneered by Xia group along with the development of Ag nanoparticles.[15, 30] With Ag nanocubes as the sacrificing templets, Au is deposited on the surface of Ag nanocubes *via* the galvanic replacement reaction at nanoscale. After the formation of completed coated Au nanoboxes, holes become to open up at the walls by the dealloy process leading to the formation of Au nanocages. During the typical synthesis, $HAuCl_4$ is dropwisely introduced to the

suspension of Ag nanocubes with the help of syringe pump, while the spectra are continuously monitored by ultraviolet–visible-near infrared (UV-vis-NIR) spectroscopy. That allows the tight control over the particle morphology and optical properties.

1.1.2 Outstanding Properties of Au Nanoparticles

Besides the properties shared across all the nanoparticle species, Au nanoparticles also possess excellent optical and chemical properties associated with the Au element and their structures.

In general, the optical properties of Au nanoparticles include the LSPR properties and the photoluminescence properties. For Au nanoparticles containing less than 300 Au atoms (~2 nm), they are often termed as Au clusters, as their crystal structures are often unstable and undefined.[6] At the same time, their energy structures demonstrate discrete energy levels which more or less resemble that of the molecule species. These energy structure provides the Au clusters with good photoluminescence properties, which have been found valuable in the application of bioimaging and biosensing. For Au nanoparticles larger than 2 nm, their discrete energy levels evolve into the band energy structure commonly seen in metals.[6]

The band energy structure presented in Au nanoparticles allows the continuous relaxation of excited electron to their ground state, which is, in general, unfavorable to the presence of photoluminescence. However, the band structure allows the free movement of electron across the metal that promotes the LSPR phenomenon.[6] When an incident light shine on to the Au nanoparticle, the LSPR occur as a result of collective oscillation of the free electrons in response to the varying electromagnetic field induced by light. When the

frequency of incident light matches the natural frequency of the electron oscillation, a resonance will occur. By varying the material, dielectric constant of the surroundings, as well as the size and morphology of the nanoparticles, the LSPR peak of Au nanoparticles could be readily tuned in a wide range to fit the requirement of biomedical applications. In general, anisotropic structure with non-spherical, hollow, and nanoshell morphology could give out LSPR peaks in the visible to NIR range.[6] With the strong LSPR peaks, these Au nanoparticles have found tremendous application in biosensing, imaging, controlled drug release, and cancer therapy.[6]

Recently, researchers also discovered the two-photon and multi-photon luminescence properties from the above mentioned plasmatic Au nanostructures.[6, 31] They have been employed as contrast agents for two-photon microscopy in both *in vitro* and *in vivo* applications. However, the underlying connection between the LSPR and two-photon luminescence properties is often ignored. It is proofed that, different from the organic dyes that absorb two coherent photons at the same time, the plasmatic Au nanorods in fact sequentially absorb two photons with an actual intermediate state in between (Figure 1.2).[32] The actual energy level of the intermediate state is provided by the *sp* energy band, while the LSPR could enhance the absorption of incident photons.

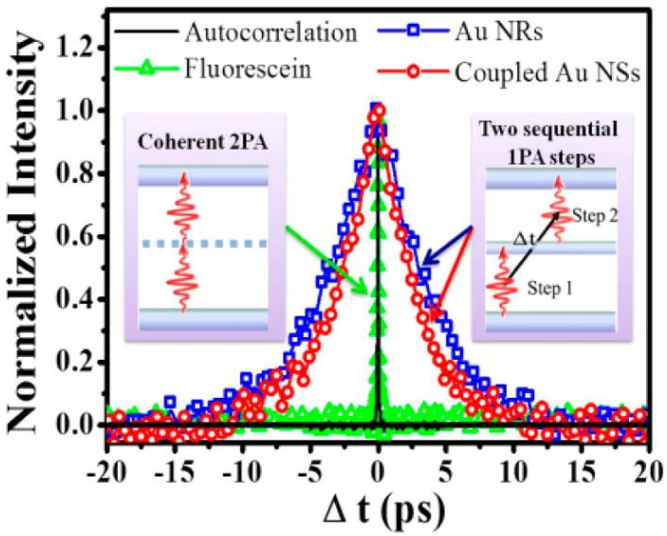

Figure 1.2. Fluorescence lifetime assay of Au nanorods (blue trace), flourescein (green trace), and coupled Au nanospheres (red trace). The excitation schematic illustration of the excitation process of coherent two-photon excitation (left inset) and two sequential one-photon excitations (right inset).

In addition to the optical properties, Au nanoparticles also possess bioinert but easily modified surface. In the contest of biomedical applications, the bio-inertness is presented as good chemical stability, low reactivity to the molecules in biological systems, and low acute toxicity.[6] The inert nature of Au, which is well known for a long period of time from the jewelry industry, is still preserved at the nanoscale. At the meantime, the inert surface presented on the Au nanoparticles could also be readily modified by the thiol containing compounds *via* the gold−thiolate bond. The gold−thiolate bond holds a relative high bond energy of 184 kJ/mol providing a stable binding for the conjugated molecules.[33] By varying the chemical groups grafted on the thiol species, we could readily prepare the Au surface with desired properties. An outstanding example is the establishment of poly(ethylene glycol) (PEG) modification of Au nanoparticles. The presence of PEG chains prevents the rapid adsorptions of serine proteins providing a much favorable kinetics for prolonged circulation and improved biodistribution profiles.[6, 8] In addition, the PEG

coated on the surface of Au nanoparticles could further serve as platform for further conjugation of functional motifs (such as antibodies, peptides, and dyes) to introduce and improve the functions of Au nanoparticles.

1.2 Application of Au Nanoparticles in Cancer Theranostics

After years of development, Au nanoparticles have been utilized in almost every field of biomedical application such as: bio-sensing, optical and nuclear imaging, targeted delivery and controlled release of drug, cancer theranostics.[6, 8] Due to the larger number of published works, I selectively summarize the applications in: 1) two-photon and multi-photon luminescence imaging; 2) radiolabeling and nuclear imaging; as well as 3) photothermal therapy and radiotherapy.

1.2.1 Application of Au Nanoparticles in Two-Photon Luminescence Imaging.

The two-photon and multi-photon luminescence effects take the advantage of non-linear absorption of photons by the Au nanoparticles under high-intensity coherent pulsed laser. Comparing to the widely used single-photon excitation confocal microscopy, two-photon and multi-photon microscopy possess smaller focal points as a result of the requirement of high intensity laser. This provides the imaging method with improved axial resolution, which could be used for optical section of cells. The laser used for the excitation typically has a wavelength in the NIR region in order to let the emission spectra fall into the visible range. This range of excitation wavelength also fit into the “transparent window” of biological tissue, helping to reduce background signals from autofluorescence and to increase the penetration depth in biological tissue.

The two-photon microscopy has been used for the tracking of Au nanoparticles during the uptake by cells. With the example of Au nanocages, our group studied the uptake process of monoclonal antibody (anti-epidermal growth factor receptor, anti-EGFR) conjugated Au nanocages by the U87MG glioblastoma cells.[34] With a commercial two-photon microscope equipped with a Ti:sapphire laser centered at 800 nm, the influence of incubation time, incubation temperature, size of the Au nanocages, and the presence of antibodies were systematically studied. It was found that anti-EGFR could greatly enhance the uptake of Au nanocages by promoting the attachment and internalization of nanoparticle *via* the antibody-antigen interactions and receptor-mediated endocytosis. With a good stability and biocompatibility, Au nanocages could be stably labeled into living cells for upto 4 weeks, allowing the *in vitro* tracking of cells. Our group further demonstrated the *in vivo* tracking of human mesenchymal stem cells.[35] Currently, Au nanoparticles could be imaged at a single particle level both *in vitro* and *in vivo*.

To avoid the photothermal destruction of cells during the imaging process, the use of three-photon excitation for photoluminescence imaging was also explored.[36] By exciting the Au nanocages with laser of 1290 nm, the photothermal effect could be greatly suppressed as the LSPR peak was averted. The destruction of living cells, represented by the blebbing of cell membrane, was only observed with the two-photon microscopy with excitation wavelength centered at 800 nm.

1.2.2 Radiolabeling and Nuclear Imaging Applications of Au Nanoparticles

As a well-known molecular imaging modality, PET possesses the capability to quantify the whole-body distribution of targeted molecules, revealing details about the

undergoing biological functions. In the field of nanomedicine, PET has been widely used for the evaluation of tumor targeting capabilities, biodistribution profiles, as well as pharmacokinetics of nanoparticles.[6] As a typical example, our group compared the biodistribution and pharmacokinetics of Au nanocages with two different edge lengths.[37] The PEGylated Au nanocages of 30 and 55 nm in edge length were conjugated with 1,4,7,10-tetraazacyclododecane-1,4,7,10-tetraacetic acid (DOTA) and labeled with Cu-64. Compared to their 55 nm counterparts, Au nanocages of 30 nm in edge length were found to have a prolonged blood retention and lower uptake by the mononuclear phagocyte system. Accordingly, the 33 nm Au nanocages were also found to demonstrate a high tumor accumulation and a centralized intratumoral distribution in a EMT-6 murine mammary carcinoma model (Figure 1.3).

In a typical process, β^+ emitting radionuclides are required to covalently bond or chelated to the surface of nanoparticles to give out detectable signals. However, the stability of radiolabeling and the alternation of surface properties are always concerns for the traditional labeling approach.[38] The unstable labeling could result in the detachment of radionuclides, giving out higher background signals along with biased biodistribution and pharmacokinetics data. In order to overcome these issues, a new radiolabeling approach was recently developed to incorporate the radionuclides into the crystal lattice of nanoparticles. Recently Liu and co-workers developed the Cu-64 labeled AuCu alloyed nanoparticles of 2.5 and 9.4 nm, and evaluated their biodistribution as well as systemic clearance properties.[38, 39] The nanoparticles were prepared by the direct reduction of $HAuCl_4$ with $^{64}Cu^{2+}$ presented in the system. It is found that the AuCu alloyed nanoparticles all have good radiolabeling stability in biological environment and could be

accumulated in the tumor region *via* passive targeting. At the meantime, the 2.5 nm alloyed particles also exhibit good systemic clearance with up to 77.0 % of the injected dose cleared collectively from feces and urine, 48 h postinjection.

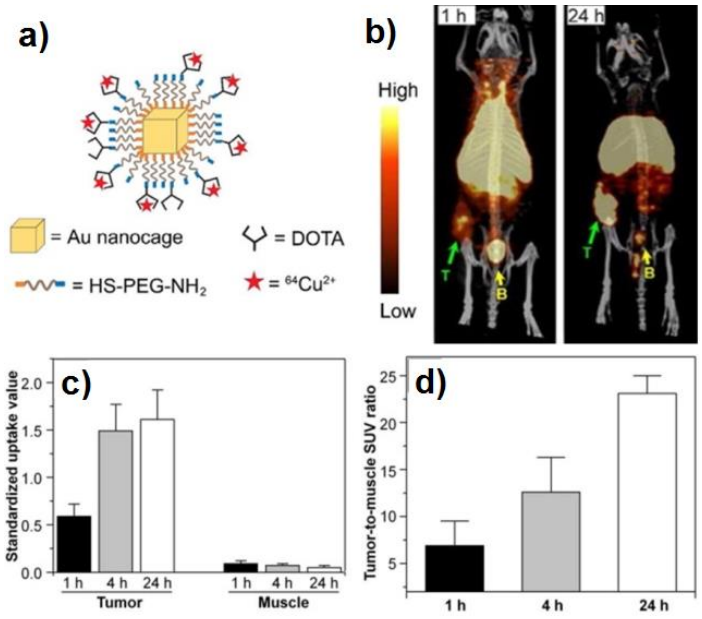

Figure 1.3. a) A schematic showing the radiolabeling technology with DOTA chelator, and the ^{64}Cu chelated Au nanocages; b) PET/CT images showing the passive targeting capability of the 30 nm ^{64}Cu-DOTA-PEG-Au nanocages with EMT-6 tumor model at 1, and 24 h postinjection. T, tumor; B, bladder. b) Standardized uptake values in tumor and muscle tissue at different time points. d) Comparison of standardized uptake values between tumor and muscle at different time points.

However, the controlling of size and morphology of the radionuclide-doped Au nanoparticles is still of great challenges.

1.2.3 Photothermal Therapy and Radiotherapy with Au Nanoparticles

After the first demonstration of Au nanoparticle-mediated photothermal therapy conducted with Au nanoshells in 2003, an increasing number of works have been published on the use of Au nanoparticles as transducers for photothermal therapy.[40, 41] In these researches, Au nanoparticles are typically engineered with LSPR peaks in the NIR region

and large absorption cross sections to minimize the destruction of health tissue while optimizing the photothermal generation. With *in vivo* tumor targeting capability, Au nanoparticles could also increase the selectivity in photothermal therapy. El-Sayed and co-workers demonstrated the use of anti-EGFR antibody conjugated Au nanorods for *in vitro* photothermal therapy.[13] It is proofed that with Au nanorods on the surface of cancer cells, the power density of incident laser required for photothermal destruction was greatly reduced from over 76 W/cm2 to 25 and 19 W/cm^2 for HSC cells and HOC cells, respectively. In another study, our group demonstrated the *in vivo* photothermal therapy of human glioblastoma with the use of PEGylated Au nanocages.[42] After systematic administration of PEGylated Au nanocages, photothermal treatment was conducted under laser irradiation at 0.7 W/cm^2. The local temperature in the tumor lesion were rapidly elevated to over 50 °C leading to a decrease of tumor metabolic activity by 70%. The mechanism of photothermal destruction of cells was also studied. It has been demonstrated that the cell membrane cavitation could be the main cause of cell death. By disrupting actin filaments, and further, the connections between the cell membrane and cytoskeleton, cells were leaded into apoptosis after treatment.[43]

Similar to the role in photothermal cancer therapy, Au nanoparticles have also been employed to enhance the therapeutic effects of radiotherapy.[6] In general, radiotherapy takes effect by the direct or indirect ionization of DNA, causing irreversible damages. In the indirect approach, which is the dominating approach in X-ray-based radiotherapy, photoelectrons and Auger electrons were generated as a result of the interaction of X-ray with matter. These free electrons could ionize the surrounding water molecules producing free radicals, which then ionize and damage the cellular DNA. Taking advantage of the

high Z-number of Au, Au nanoparticles could enhance the attenuation of X-ray producing more free electrons. However, after the publication of many works the detailed mechanism of the radiosensitizing effect and the resistance from the cells remain unclear.

1.3 Scope of This Work

Despite the large number of pre-clinical research and enormous investment of research fund, only a few Au nanoparticle-based medicines have been approved for clinical trials.[7] The application in real-world clinics is still limited by several issues. First, the unsatisfactory biodistribution was found for most kinds of Au nanoparticles, resulting in relatively low accumulation in tumor lesion and inevitably significant accumulation in major organs. Second, Au nanoparticles with a hydrodynamic diameter larger than 8 nm could not be effectively cleared from body. Third, the long-term effects of Au nanoparticles still demand throughout investigation. The concern of adverse effect brought by the clearance and long term accumulation of the off-targeted nanomedicine are still needed to be addressed. The decision of whether to put a nanomedicine into clinical use has become a tradeoff between the clinical benefit and the side effect.

This dissertation was dedicated to the integration of molecular imaging technology and the latest nano-chemistry with focuses on nanoparticle engineering, incorporation of novel isotope, as well as the development of new tumor targeting technology. Work accomplished in this dissertation made important progresses towards the ultimate goal of clinical application of Au nanoparticle for cancer theranostics. To achieve this goal, plenty of effort still needs to be devoted.

In chapter 2, I developed Cu-64 doped PdCu@Au tripods for PET-guided photothermal treatment of triple negative breast cancer. I developed the controlled synthesis of PdAu@Cu tripods and demonstrated their excellent optical properties and photothermal generation capability. I also stably labeled Cu-64 into the crystal lattice of the tripods giving them the capability PET probes. A high tumor accumulation was also observed in targeting a new biomarker (C-C chemokine receptor 5, CCR5) in triple negative breast tumor model.

In chapter 3, I studied the use of PdCu@Au tripods for two-photon luminescence imaging. Based on our current understanding on the connection between the energy structure, LSPR property, and the two-photon luminescence property, I verified the existence of bright two-photon luminescence in PdCu@Au tripods. I benchmarked their two-photon luminescence property to the organic dyes and Au nanorods, finding a much larger two-photon action cross section.

In chapter 4, I develop Au-199 integrated Au nanoparticles for targeted SPECT cancer imaging. I chemically fixed Au-199 into the lattice of Au nanospheres for an improved radiolabeling with higher stability. After the measurement of labeling rate and radiochemistry purity, I also tested the *in vivo* tumor targeting capability of labeled Au nanospheres. I introduced Au-199 as a suitable medical isotope for SPECT imaging as its emitted γ photon could be imaged with the commercial available SPECT with the existing setting for ^{99m}Tc.

In chapter 5, I developed Arg-Gly-Asp (RGD) peptide-conjugated Au nanorods for radio-sensitization in radio therapy. I obtained highly uniform RGD-conjugated Au

nanorods, and testified their capability to enhance therapeutic effect of radiotherapy *via in vitro* radiotherapy. I further studied the process and mechanism of the radiosensitization effect. It is found that the RGD-conjugated Au nanorods could reduce the resistance to radiotherapy by lowering the expression level of $\alpha_v\beta_3$ integrin, while increasing the portion of cells arrested in G_2/M phase.

In chapter 6, I summarize this dissertation by highlighting the innovations of the works presented in the dissertation, and illustrate some of the potential impacts of these works. Future works are also proposed in two directions: the further integration of functionality, and the fabrication of biodegradable Au nanomaterials. These two directions are dedicated to the elevation of clinical benefit and the reduction of side effects, respectively.

1.4 References

[1] Stewart, B.W.; Wild, C.P. *World Cancer Report 2014*. International Agency for Research on Cancer, Lyon, France 2014.

[2] Etzioni; R.; Urban, N.; Ramsey, S.; Mcintosh, M.; Schwartz, S.; Reid B.; *et al*. The case for early detection. *Nat. Rev. Cancer* **2003**, 3, 243–252.

[3] Fass, L. Imaging and cancer: a review. Mol. Oncol. **2008**, 2, 115–152.

[4] Weissleder, R.; Mahmood, U.; Molecular imaging. *Radiology* **2001**, 219, 316–333.

[5] Farokhzad, O.C.; Langer, R. Impact of nanotechnology on drug delivery. *ACS Nano* **2009**, 3, 16–20.

[6] Yang, X.; Yang, M.; Pang, B.; Vara, M.; Xia, Y. Gold nanomaterials at work in biomedicine. *Chem. Rev.* **2015**, 115, 10410–10488.

[7] Sun, T.; Zhang, Y.S.; Pang, B.; Hyun, D.C.; Yang, M.; Xia, Y. Engineered nanoparticles for drug delivery in cancer therapy. *Angew. Chem. Int. Ed.* **2014**, 53, 12320–12364.

[8] Dreaden, E.C.; Alkilany, A.M.; Huang, X.; Murphy, C.J.; El-Sayed, M.A. The golden age: gold nanoparticles for biomedicine. *Chem. Soc. Rev.* **2012**, 41, 2740–2779.

[9] Zheng, Y.; Ma, Y.; Zeng, J.; Zhong, X.; Jin, M.; Li, Z-Y; *et al*. Seed-mediated synthesis of single-crystal gold nanospheres with controlled diameters in the range 5–30 nm and their self-assembly upon dilution. *Chem. – Asian J.* **2013**, 8, 792–799.

[10] Cho, E.C.; Liu, Y.; Xia, Y. A simple spectroscopic method for differentiating cellular uptakes of gold nanospheres and nanorods from their mixtures. *Angew. Chem. Int. Ed.* **2010**, 49, 1976–1980.

[11] Wang, H.; Brandl, D.W.; Nordlander, P.; Halas, N.J. Plasmonic nanostructures: artificial molecules. *Accounts Chem. Res.* **2007**, 40, 53–62.

[12] Cobley, C.M.; Chen, J.; Cho, E.C.; Wang, L.V.; Xia, Y. Gold nanostructures: a class of multifunctional materials for biomedical applications. *Chem. Soc. Rev.* **2011**, 40, 44–56.

[13] Huang, X.; El-Sayed, I.H.; Qian, W.; El-Sayed, M.A. Cancer cell imaging and photothermal therapy in the near-infrared region by using gold nanorods. *J. Am. Chem. Soc.* **2006**, 128, 2115–2120.

[14] West, J.L.; Halas, N.J. Engineered nanomaterials for biophotonics applications: improving sensing, imaging, and therapeutics. *Ann. Rev. Biomed. Eng.* **2003**, 5, 285–292.

[15] Skrabalak, S.E.; Au, L.; Li, X.; Xia, Y. Facile synthesis of Ag nanocubes and Au nanocages. *Nat. Protoc.* **2007**, 2, 2182–2190.

[16] Cho, E.C.; Kim, C.; Zhou, F.; Cobley, C.M.; Song, K.H.; Chen, J.; *et al*. Measuring the optical absorption cross sections of Au−Ag nanocages and Au nanorods by photoacoustic imaging. *J. Phys. Chem. C* **2009**, 113, 9023–9028.

[17] Hu, M.; Chen, J.; Li, Z-Y.; Au, L.; Hartland, G.V.; Li, X.; *et al*. Gold nanostructures: engineering their plasmonic properties for biomedical applications. *Chem. Soc. Rev.* **2006**, 35, 1084–1094.

[18] Faraday, M. The Bakerian Lecture: Experimental relations of gold (and other metals) to light. *Philos. Trans. R. Soc. London* **1857**, 147, 145–181.

[19] Turkevich, J.; Stevenson, P.C.; Hillier, J. A study of the nucleation and growth processes in the synthesis of colloidal gold. *Discuss. Faraday Soc.* **1951**, 11, 55–75.

[20] Frens, G. Particle size and sol stability in metal colloids. *Colloid Polym. Sci.* **1972**, 250, 736–741.

[21] Ojea-Jiménez, I.; Bastús, N.G.; Puntes, V. Influence of the sequence of the reagents addition in the citrate-mediated synthesis of gold nanoparticles. *J. Phys. Chem. C* **2011**, 115, 15752–15757.

[22] Ji, X.; Song, X.; Li, J.; Bai, Y.; Yang, W.; Peng, X. Size control of gold nanocrystals in citrate reduction: the third role of citrate. *J. Am. Chem. Soc.* **2007**, 129, 13939–13948.

[23] Brust, M.; Walker, M.; Bethell, D.; Schiffrin, D.J.; Whyman, R. Synthesis of thiol-derivatised gold nanoparticles in a two-phase liquid-liquid system. *J. Chem. Soc., Chem. Commun.* **1994**, 801–802.

[24] Rodríguezfernández, J.; Pérezjuste, J.; Fj, G.D.A.; Lizmarzán, L.M. Seeded growth of submicron Au colloids with quadrupole plasmon resonance modes. *Langmuir* **2006**, 22, 7007–7010.

[25] Zheng, Y.; Zhong, X.; Li, Z.; Xia, Y. Successive, Seed-mediated growth for the synthesis of single-crystal gold nanospheres with uniform diameters controlled in the range of 5–150 nm. *Part. Part. Syst. Char.* **2014**, 31, 266–273.

[26] Jana, N.R.; Gearheart, L.; Murphy, C.J. Seed-mediated growth approach for shape-controlled synthesis of spheroidal and rod-like gold nanoparticles using a surfactant template. *Adv. Mater.* **2001**, 13, 1389–1393.

[27] Nikoobakht, B.; El-Sayed, M.A. Preparation and growth mechanism of gold nanorods (NRs) using seed-mediated growth method. *Chem. Mater.* **2003**, 15, 1957–1962.

[28] Oldenburg, S.J.; Averitt, R.D.; Westcott, S.L.; Halas, N.J. Nanoengineering of optical resonances. *Chem. Phys. Lett.* **1998**, 288, 243–247.

[29] Pang, B.; Yang, X.; Xia, Y. Putting gold nanocages to work for optical imaging, controlled release and cancer theranostics. *Nanomedicine (Lond.)* **2016**, 11, 1715–1728.

[30] Sun, Y.; Xia, Y. Shape-controlled synthesis of gold and silver nanoparticles. *Science* **2002**, 298, 2176–2179.

[31] Gao, N.; Chen, Y.; Li, L.; Guan, Z.; Zhao, T.; Zhou, N.; *et al*. Shape-dependent two-photon photoluminescence of single gold nanoparticles. *J. Phys. Chem. C* **2014**, 118, 13904–13911.

[32] Jiang, X-F.; Pan, Y.; Jiang, C.; Zhao, T.; Yuan, P.; Venkatesan, T.; *et al*. Excitation nature of two-photon photoluminescence of gold nanorods and coupled gold nanoparticles studied by two-pulse emission modulation spectroscopy. *J. Phys. Chem. Lett.* **2013**, 4, 1634–1638.

[33] Love, J.C.; Estroff, L.A.; Kriebel, J.K.; Nuzzo, R.G.; Whitesides, G.M. Self-assembled monolayers of thiolates on metals as a form of nanotechnology. *Chem. Rev.* **2005**, 105, 1103–1170.

[34] Au, L.; Zhang, Q.; Cobley, C.M.; Gidding, M.; Schwartz, A.G.; Chen, J.; *et al*. Quantifying the cellular uptake of sntibody-conjugated Au nanocages by two-photon microscopy and inductively coupled plasma mass spectrometry. *ACS Nano* **2009**, 4, 35–42.

[35] Zhang, Y.S.; Wang, Y.; Wang, L.; Wang, Y.; Cai, X.; Zhang, C.; *et al*. Labeling human mesenchymal stem cells with gold nanocages for *in vitro* and *in vivo* tracking by two-photon microscopy and photoacoustic microscopy. *Theranostics* **2013**, 3, 532–543.

[36] Tong, L.; Cobley, C.M.; Chen, J.; Xia, Y.; Cheng, J-X. Bright three-photon luminescence from gold/silver alloyed nanostructures for bioimaging with negligible photothermal toxicity. *Angew. Chem. Int. Ed.* **2010**, 49, 3485–3488.

[37] Wang, Y.; Liu, Y.; Luehmann, H.; Xia, X.; Brown, P.; Jarreau, C.; *et al*. Evaluating the pharmacokinetics and *in vivo* cancer targeting capability of Au nanocages by positron emission tomography imaging. *ACS Nano* **2012**, 6, 5880–5888.

[38] Zhao, Y.; Sultan, D.; Detering, L.; Cho, S.; Sun, G.; Pierce, R.; *et al*. Copper-64-alloyed gold nanoparticles for cancer imaging: improved radiolabel stability and diagnostic accuracy. *Angew. Chem.* **2014**, 126, 160–163.

[39] Zhao, Y.; Sultan, D.; Detering, L.; Luehmann, H.; Liu, Y. Facile synthesis, pharmacokinetic and systemic clearance evaluation, and positron emission tomography cancer imaging of ^{64}Cu-Au alloy nanoclusters. *Nanoscale* **2014**, 6, 13501–13509.

[40] Cheng, L.; Wang, C.; Feng, L.; Yang, K.; Liu, Z. Functional nanomaterials for phototherapies of cancer. *Chem. Rev.* **2014**, 114, 10869–10939.

[41] Hirsch, L.R.; Stafford, R.J.; Bankson, J.A.; Sershen, S.R.; Rivera, B.; Price, R.E.; *et al*. Nanoshell-mediated near-infrared thermal therapy of tumors under magnetic resonance guidance. *P. Natl. Acad. Sci. USA* **2003**, 100, 13549–13554.

[42] Chen, J.; Glaus, C.; Laforest, R.; Zhang, Q.; Yang, M.; Gidding, M.; *et al*. Gold nanocages as photothermal transducers for cancer treatment. *Small* **2010**, 6, 811–817.

[43] Tong, L.; Zhao, Y.; Huff, T.B.; Hansen, M.N.; Wei, A.; Cheng, J.X. Gold nanorods mediate tumor cell death by compromising membrane integrity. *Adv. Mater.* **2007**, 19, 3136–3141.

CHAPTER 2. CU-64 DOPED NANOTRIPODS FOR PET-GUIDED PHOTOTHERMAL TREATMENT OF CANCER

In this chapter, I elaborate the innovative works around the controlled synthesis of PdCu@Au core-shell tripods. As the anisotropic Au nanostructures are difficult to be prepared at high purity, the PdCu@Au tripods are the first in their kind, having a novel tripod structure. With the development of new material, I successfully integrated the PET contrast enhancement capability to this material by incorporating Cu-64 into the crystal lattice of the nanoparticles. I then demonstrated the use of PdCu@Au tripods as both contrast agents for PET imaging and photothermal transducers for photothermal therapy of cancer, through the PET guided photothermal therapy of triple negative 4T1 tumor.

2.1 Introduction

One of the research frontier in the field of Au nanoparticle-based nanomedicine is the syntheses of Au nanoparticles of new morphology, aiming at the optimization of their properties according to the requirement of various applications. Associated with tunable LSPR peaks, anisotropic Au nanoparticles (*e.g.* Au nanorods) have attracted extensive research attentions on their controlled synthesis and applications.[1-3] As outstanding examples of anisotropic Au nanoparticles, branched Au nanoparticles, such as stars and flowers, have been widely explored in surface-enhanced Raman scattering (SERS) as the electromagnetic field could be greatly enhanced at their tips.[2, 4] With a structural similarity between the single tip/arm of branched Au nanoparticles and Au nanorods, branched Au nanoparticles often possess LSPR peaks that could be feasibly tuned into NIR region

similar to that of Au nanorods.[5] That property facilitated their *in vivo* applications as this LSPR peak matches the "transparent window" of human tissues, helping to achieve a deeper penetration for optical imaging and photothermal therapy.[6, 7] In addition, branched Au nanoparticles are also observed to have large optical cross section, which is orders of magnitude higher than that of organic dyes, at the resonance condition of LSPR. Taken together, their extraordinarily LSPR properties, tunable peak and larger optical cross section, greatly facilitated their applications as theranostic agents in bio-imaging, delivery and triggered release of drug, as well as photothermal cancer treatment.[8, 9, 10, 11]

Apart from the optical properties, the biodistribution profiles and pharmacokinetics of Au nanoparticle-based cancer nanomedicine were also greatly affected by the morphology of the Au nanoparticles. Their tumor targeting capability, intratumoral distribution, as well as toxicity will, in turn, be affected.[2, 12, 13] that makes the preparation of branched Au nanoparticles more attractive for biomedical applications. Although significant research effort has been dedicated, the controlled synthesis of branched Au nanoparticles remains to be challenging for solution phase-synthesis.[1] The typical synthesis involves the initiation of anisotropic growth at multiple sites or the aggregation of particle seeds, before the directed growth of arms. Still, the directed growth of the tips/arms may often require the help from CTAB *via* a similar mechanism of the growth of Au nanorods, which would leave highly toxic residues.[1-3]

In spite of the enormous number of works published on Au nanoparticles, the radiolabeling techniques of Au nanoparticles still require further research attention. Tough having unique LSPR peaks and large optical cross sections for optical imaging, a stable radiolabeling is always necessary so that the nanoparticles could be tracked *in vivo* using

clinical accessible nuclear imaging modalities such as PET and SPECT. The most widely used radiolabeling technology is to chemically bond or chelate radionuclides with the help of functional compounds or chelating ligands. Though radionuclides could be labeled to Au nanoparticles of any size and shape *via* this approach, the stability of radiolabeling always remains as a concern.[14] In recent works, radionuclides like Cu-64 has been reported to be directly doped into the crystal lattice of Au nanostructures such as Au nanospheres and clusters for an improved radiolabeling stability.[15, 16, 17] However, the morphology of Cu-64 doped Au nanoparticles can hardly be controlled to have an anisotropic structure. And the Cu-64 radionuclides could still be leached out as de-alloy could happen to the Cu atoms on the surface of particles.

In this chapter, I demonstrated the facile preparation of PdCu@Au core-shell tripods and their use as multifunction theranostic agents for PET guided photothermal therapy. The PdCu@Au tripods were prepared *via* a seed-mediated growth approach to have an average arm length of 42 nm. The PdCu bimetallic tripods recently developed by our group were employed as the templets for the conformal coating of Au.[18] The coating of Au leads to the formation of the featured LSPR peaks, while enclosed the Cu atoms into the cores protecting them from de-alloying. By varying the thickness of Au coating layer, the LSPR peaks of PdCu@Au tripod could continuously be tuned from 1000 to 800 nm. As the incorporation of Cu-64 (half-life = 12.7 h, β^+ = 17%) was achieved by partially substituting $CuCl_2$ precursor with $^{64}CuCl_2$ directly during the synthesis of PdCu bimetallic tripods, this labeling approach provides PdCu@Au tripods with superior stability for accurate PET imaging and the capability for a number of theranostic applications.[15, 13, 16, 17, 19]

Aside from the great reduction of mortality rate for certain types of cancer, new cancer biomarkers are still needed to improve the diagnostic accuracy, and to monitor cancer progression for personalized medicine with the help of molecular imaging.[20, 21, 22] Among the various cancer biomarkers, the CCR5 is of great potential to be a theranostic target, as the role of C-C chemokine ligand 5 (CCL5)/CCR5 axis in promoting cancer progression has recently been proofed.[23-25] As a cancer progression biomarker, they are clinically testified to be up-regulated in both primary tumor lesion and the metastases sites, especially in triple negative breast cancer.[26, 27] In order to enable the PdCu@Au tripods with better tumor targeting efficiency, I conjugated a ligand (D-Ala1-peptide T-amide, DAPTA) to the surface of tripods to actively target triple negative cancer.[28] I further assessed the biodistribution profiles and tumor targeting capabilities of the targeted PdCu@Au tripods in comparison to their non-targeted counterparts in 4T1 triple negative breast cancer mouse model. The use of this novel class of Au nanoparticle as a multifunctional platform for PET guided photothermal cancer treatment was also demonstrated.

2.2 Results and Discussions

2.2.1 Synthesis and Characterization of PdCu@Au Tripods

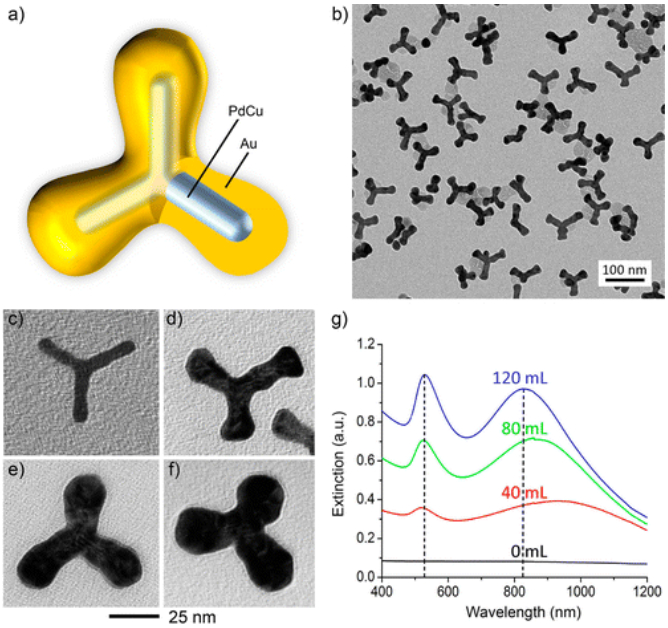

Figure 2.1. The morphology and LSPR property of PdCu@Au tripods. a) A schematic illustration of the structure of PdCu@Au tripod. b) The TEM image showing the PdCu@Au tripods obtained by conformal coating of Au by reacting 120 mL 0.5 mM $HAuCl_4$ with 1 mL of PdCu tripods. Panel (c-f) show the TEM images of individual tripods at different stage of Au coating by varying the amount of 0.5 mM $HAuCl_4$ introduced to each 1 mL of PdCu tripods. The amount of $HAuCl_4$ corresponding to panel c-f are 0, 40, 80, and 120 mL, respectively. g) The UV-vis-NIR spectra corresponding to the samples of c-f, showing a readily tuned longitudinal LSPR peak from 1000 to 800 nm.

As shown in Figure 2.1a, the PdCu@Au tripod possesses a PdCu bimetallic core with a layer of Au conformably coated. The TEM image of a typical sample are demonstrated in Figure 2.1b. To better control the morphology of PdCu@Au tripods, I employed a two-step process in the synthesis that starts with the preparation of PdCu bimetallic tripods, followed by the conformal coating of Au layers *via* chemical deposition. The PdCu bimetallic tripods used in the experiment, which have uniform size and arm number, were first prepared *via* a synthesis recently reported by our group.[18] In this synthesis, the chemical reduction of Na_2PdCl_4 by AA was conducted in aqueous solution containing $CuCl_2$ and KBr, with poly(vinyl pyrrolidine) (PVP, MW ≈ 55,000) as colloidal

stabilizer at 80 °C. The arm length of the PdCu tripods could be controlled by varying the amount of KBr as well as the reaction time.[18] In this study, I focus on the use of PdCu tripods with arm length about 25 nm as they can control the overall lateral dimension below 50 nm while maintaining a good uniformity in size and shape. As shown in Figure 2.2, the as prepared PdCu tripods were measured to have an average length (l) of 24.8 ± 4.6 nm along with an average diameter (d) of 5.8 ± 0.4 nm for their arms. For the incorporation of Cu-64, trace amount of $^{64}CuCl_2$ with controlled radioactivity was introduced to the aforementioned synthesis while keeping all other experimental conditions the same. Excess radioactivity was washed off before Au coating.

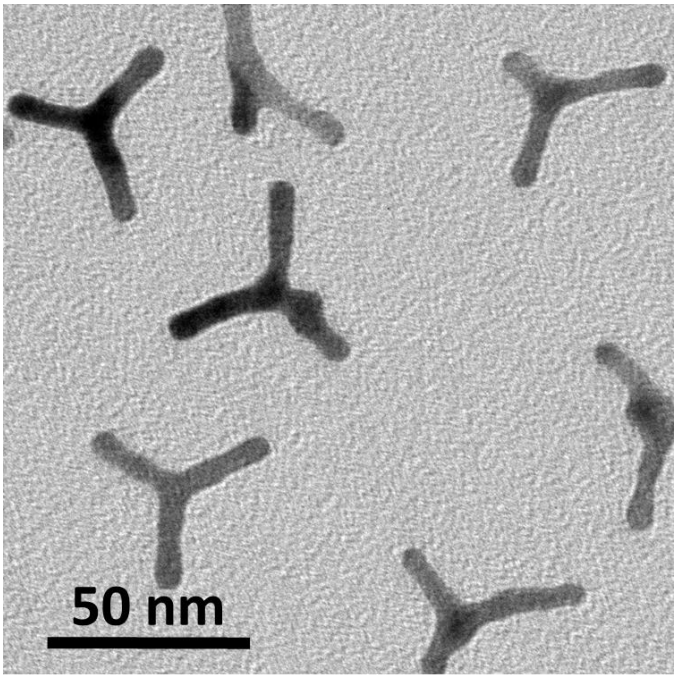

Figure 2.2. TEM image of the non-radioactive PdCu alloy tripods. The arms of PdCu tripods are uniform in length and diameter.

The as prepared PdCu tripods were then subjected to conformal coating of Au by titrating $HAuCl_4$ into the aqueous suspension of PdCu tripods in the presence of AA and PVP. With the dropwise addition of $HAuCl_4$, the thickness of the Au coating layer

increased gradually up to a thickness of about 8 nm. By controlling the amount of $HAuCl_4$ solution (0.5 mM) introduced to each 1 mL of PdCu tripods, a series of TEM images were taken to illustrate the morphology change of the tripods during a typical coating process (Figure 2.1, c-f). During the coating process, the tripod morphology PdCu tripod templets could be preserved. However, limited to the preferential deposition of Au atoms on the tips and the low surface diffusion rate, the arms of tripods became tapered along with the Au coating. At the same time, LSPR peaks of tripods began to show up with a transverse peak at *ca.* 530 nm and a longitudinal peak shifting from *ca.* 1000 nm to *ca.* 800 nm, along with the titration process (Figure 2.1g). This shifting LSPR peak could also be used to monitor the extent of reaction when the UV-vis-NIR spectra were frequently monitored during the reaction. In the present study, I prepared PdCu@Au tripods with a longitudinal LSPR peak at *ca.* 810 nm by immediately stopped the titration when the longitudinal LSPR peak reached 810 nm. This titration process typically took 120 mL of 0.5 mM $HAuCl_4$ for the conversion of each 1 mL of PdCu tripod templets. Observed by TEM, these PdCu@Au tripods were found to have an average arm length (l) about 42.2 ± 6.4 nm and an average arm diameter (d) of 21.7 ± 4.5 nm.

To quantify the absorption to extinction ratio of the PdCu@Au tripods, I further calculated the LSPR spectra of the tripods using the three-dimensional finite-difference time-domain (3D-FDTD) simulation.[64] In the numerical model, the PdCu tripod was set to hold an arm length of 25 or 35 nm with an arm diameter of 6 nm. As shown in Figure 2.3, with the coating layer varied from 2 to 8 nm, their longitudinal mode of LSPR peaks was observed to blue-shift from over 100 nm to visible range, which is in good agreement with the experimental observation. However, we only observed a broad longitudinal mode

of LSPR peaks as the result of polydispersity and random orientations of the particles in a real sample. The absorption to extinction ratio of the PdCu@Au tripod were also determined to be about 90 %, at 810 nm by the numerical result, indicating a great potential of biomedical application of photothermal cancer therapy.[2, 3, 11]

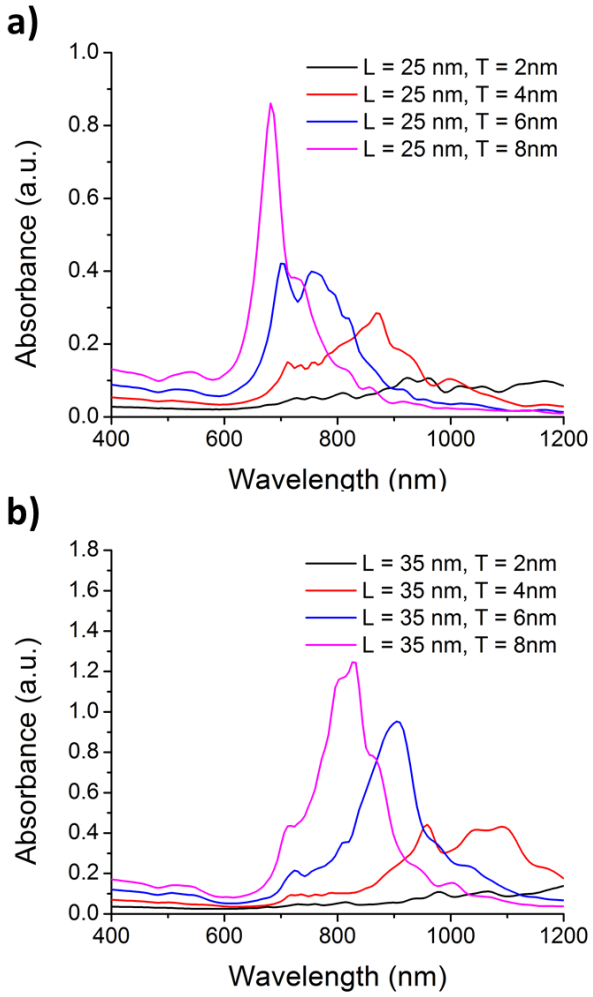

Figure 2.3. The extinction spectra calculated using 3D-FDTD method. The model of PdCu@Au tripods is set to have different arm lengths (l), with thickness in Au coating (t). The spectra are obtained with l=25 nm (a) and l=35 nm (b), at various t values. The diameter of the arms of PdCu bimetallic tripod (d) was set to 6 nm for all calculation.

To assess the *in vitro* labeling efficiency and chemical purity of Cu-64 doped PdCu@Au tripods, I measured the free $^{64}Cu^{2+}$ in the suspension of Pd^{64}Cu@Au tripods

using radioactive thin layer chromatography (Radio-TLC). As shown in Figure 2.4, no free $^{64}Cu^{2+}$ ions could be observed directly from Radio-TLC trace. It is indicated that the incorporation of Cu-64 was successful, thus all the radioactivity was found only in the tripods. The sample of Cu-64 doped Pd^{64}Cu@Au tripods was also observed using TEM after the complete decay of radionuclides to directly analyze their morphology. As demonstrated in Figure 2.5, in a period of up to 90 days, the structural integrity and morphology of PdCu@Au tripods maintained, when preserved in Dulbecco's phosphate buffered saline (DPBS), showing no noticeable changes during the decay. From the TEM images, the arm length and diameter of the decayed Pd^{64}Cu@Au tripods were measured to be 44.5 ± 5.8 nm and 21.5 ± 1.9 nm, respectively, by averaging 50 independent measures. These measures were comparable to the values obtained from the non-radioactive PdCu@Au tripods synthesized with the same procedure without the introduction of $^{64}CuCl_2$ (Figure 2.1b). This result also demonstrated that the formation of complete conformal coating of Au could help to prevent the de-alloying process from happening, by isolate the PdCu bimetallic cores from the oxidization and dissolution caused by the environment. This Au coating also provides the tripods with an inert while easily functionalized surface for further conjugation.[8, 12]

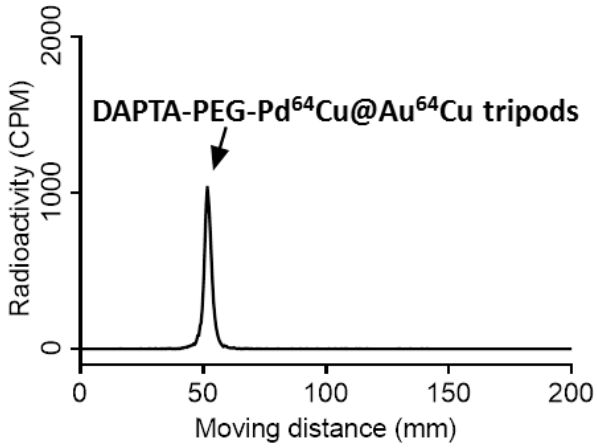

Figure 2.4. The Radio-TLC result of the Cu-64 doped $Pd^{64}Cu$@Au tripods (shown as DAPTA-PEG-$Pd^{64}Cu$ @$Au^{64}Cu$). The trace shows a single peak with low moving distance indicating that the radioactive Cu-64 was completely enveloped in the tripods with no free or dissociated Cu-64 observed.

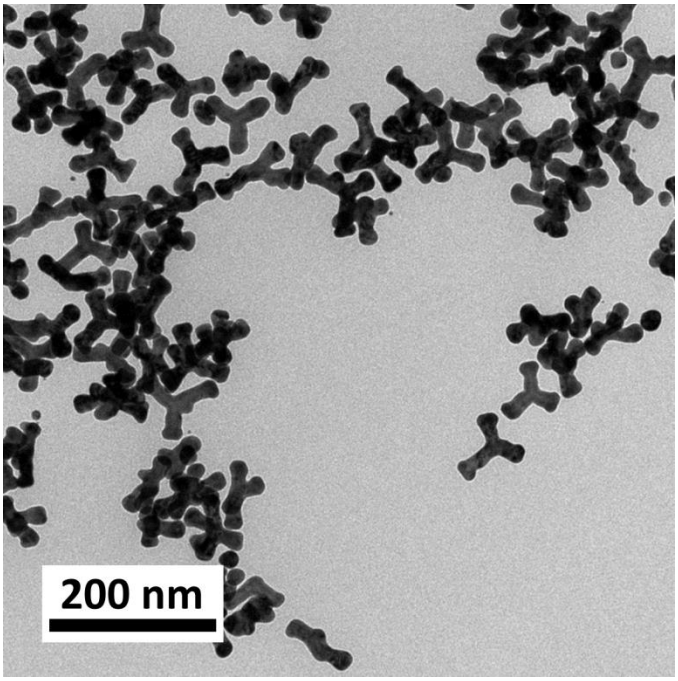

Figure 2.5. The TEM images showing the typical sample of Cu-64 doped PEGylated $Pd^{64}Cu$@Au tripods after 90 days of decay (170 half-life) in DPBS. Protected by the Au coating layer, the integrity and morphology of $Pd^{64}Cu$@Au were fully retained.

2.2.2 Evaluation of Photothermal Effect In Vitro

To demonstrate the photothermal generation capability and to assess their efficiency, I quantified the photothermal heating profiles of aqueous suspension of PdCu@Au tripods for different particle concentration under various laser irradiation conditions. In this study, PdCu@Au tripods were dispersed in 100 μL of DPBS to a final concentration of 0−400 pM and transferred into different wells on a 96-well plate. The suspensions were then irradiated with a diode laser with central wavelength at 808 nm and power intensity varied in the range of 0.25−1.0 W/cm^2. The increase in temperature was monitored simultaneously by an infrared camera (Infrared Camera, Beaumont, TX). The photothermal heating profiles were obtained as Figure 2.6. In a typical process, the temperature of the PdCu@Au suspension raised rapidly at the beginning of irradiation before leveling off at over 5 min. The photothermal heating of PdCu@Au suspension also shows a power and concentration dependent feature. Under the power intensity of 1 W/cm^2, a large rise in temperature was observed from samples containing 100 and 400 pM PDCu@Au tripods with a temperature increase of 11.8 and 33.4 °C, respectively. This result suggests that the PdCu@Au tripods possess the photothermal generation capability to drastically elevate the local temperature in biological tissue causing irreversible damages to cancerous cells through hyperthermia (41−48 °C) or ablation (>48 °C). [30] Comparing to the data harvested at same experimental conditions, I benchmarked the photothermal generation capability to that of Au nanocages[31] and Au nanohexapods,[32] previously reported by our group. It is shown that PdCu@Au tripods hold a comparable photothermal generation capability to that of Au nanocages as well as hexapods, which could be of great potential for biomedical applications.

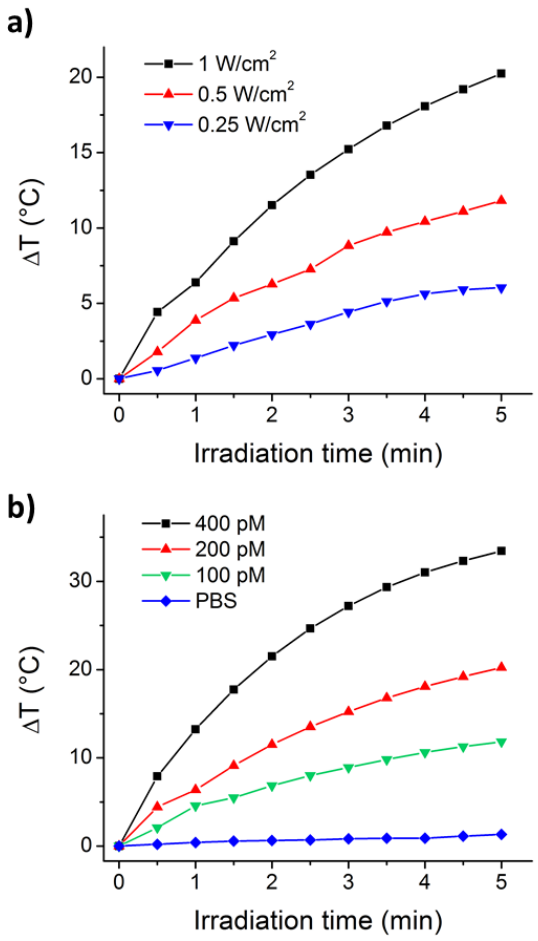

Figure 2.6. The assessment of photothermal generation capability of PdCu@Au tripods. a) Plots of the temperature at different laser intensity, showing the power dependent behavior for aqueous suspensions containing 200 pM PdCu@Au tripods. b) Plots of the temperature at different particle concentration, showing the concentration dependent behavior for aqueous suspensions irradiated by laser at power density of 1 W/cm^2.

2.2.3 Evaluation of Cell Toxicity and Cell Uptake In Vitro

Before using PdCu@Au tripods for *in vivo* applications, I assessed their cytotoxicity *in vitro* with a standard cell proliferation assay using 3-(4,5-dimethylthiazol-2-yl)-2,5-diphenyltetrazolium bromide (MTT) on 4T1 breast cancer cells. The cell viability was quantified after 24 h of incubation for both PEGylated PdCu@Au tripods and DAPTA-conjugated tripods, at various particle concentration in the range of 6.25 to 800 pM. As

shown in Figure 2.17, compared with the control group, no significant decrease of cell viability was observed for both experimental groups up to a high particle concentration of 400 pM. This cytotoxicity level is also comparable to other kinds of Au nanoparticles reported previously.[3] At a higher concentration, the DAPTA-conjugated group demonstrates a slightly lower cell viability, but the difference between the two groups is not statistically significant. It is worth pointing out that the Pd and Cu presented in the PdCu@Au tripods are often considered to be heavy metals that are highly toxic to organism when they are oxidized and leached as ions. However, the complete coating of Au layers could help to protect the PdCu bimetallic cores, preventing them from oxidization and de-alloy. The short-term cytotoxicity could then be reduced to a negligible level.

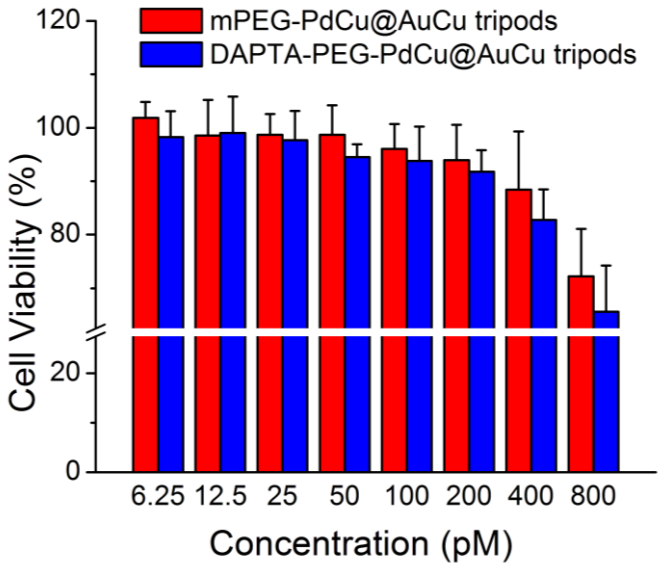

Figure 2.7. Cell proliferation test of 4T1 breast cells. Cell viability was derived by normalizing the cell viability from PEGylated and DAPTA-conjugated groups to the control group, after 24 h of incubation. Error bars stands for the standard errors with n = 3.

Following the assessment of cytotoxicity, I further tested the *in vitro* targeting efficiency of DAPTA-conjugated PdCu@Au tripods to 4T1 triple negative breast cancer cells. By incubating with tripods of both kinds of surface modification side by side on the same 24-well plates, the cells were allowed to uptake the PdCu@Au tripods for different periods of times. To calculate the particle concentration, the metal contents were measured by inductively coupled plasma mass spectrometry (ICP-MS) after the cells were washed, harvested, and digested by aqua regia. It is shown that the DAPTA-conjugated PdCu@Au tripods have a high cancer targeting efficiency ($p < 0.001$, $n = 3$), with $19.5 \pm 1.1 \times 10^3$ particles/cell at 24 h of incubation. This value almost triple the amount of particles observed in the uptake of PEGylated group that is $7.3 \pm 1.7 \times 10^3$/cell (Figure 2.8). This result confirms the enhancement in tumor targeting capability brought by the conjugation of DAPTA toward the CCR5.

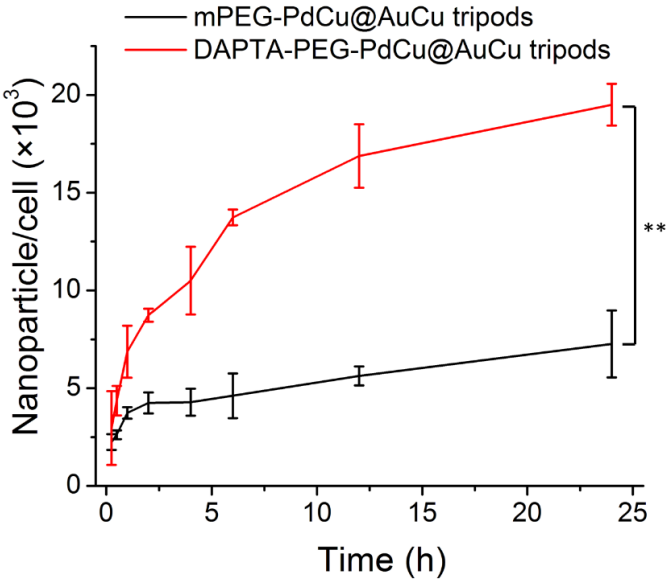

Figure 2.8. A comparison of the uptakes of the non-radioactive non-targeted and CCR5-targeted tripods core-shell by 4T1 cells after incubation for different periods of time. Error bars are standard errors with n = 3. ** p < 0.005.

2.2.4 Evaluation of Biodistribution

The *in vivo* biodistribution and tumor targeting experiment was then conducted with PdCu@Au tripods with or without the conjugation of DAPTA peptides in 4T1 tumor-bearing mice models. Figure 2.9 demonstrated the biodistribution profiles of DAPTA-conjugated PdCu@Au tripods along with their non-targeted counterparts at different time points. Both kinds of the nanoparticles showed good blood retention for a time period up to 24 h, post intravenous injection through tail vein. The PEGylated PdCu@Au tripods demonstrated a higher blood retention at all three time points 36.9 ± 0.7 percentage of the injected dose per gram of tissue (%ID/g) and 33.5 ± 2.6 %ID/g at 1 and 4 h, respectively. The corresponding blood retention was measured to be 31.0 ± 1.6 %ID/g and 24.3 ± 1.8 %ID/g for the DAPTA-conjugated tripods. At the same time, a significant clearance from mononuclear phagocyte system (liver and spleen) was also observed for tripods with both kinds of surface modification, in consisting with other kinds of Au nanoparticles.

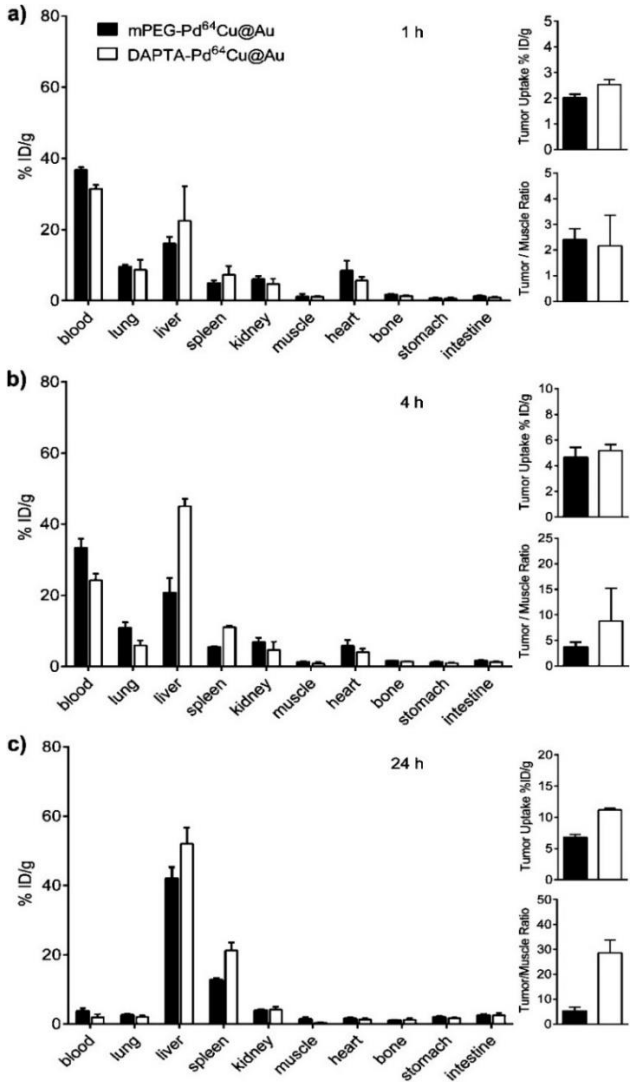

Figure 2.9. Biodistribution and tumor targeting of the Cu-64 doped $Pd^{64}Cu$@Au tripods with or without DAPTA peptide conjugation a t1 (a), 4 (b), and 24 h (c) post injection.

As shown in Figure 2.9 a and b (right panels), PdCu@Au tripods with both kinds of surface modifications were observed to have comparable tumor uptake as well as the tumor to muscle ratios at 1 and 4 h post injection. This result is in good agreement with our previous study, that the necessary time duration to establish a good passive targeting through the enhanced permeation and retention (EPR) effect is 4-6 h.[14] The effect of active targeting was only observed to bring modest improvement to the targeting of cancer, with

5.19 ± 0.47 %ID/g (vs. 4.64 ± 0.80 %ID/g for non-targeted tripods) accumulated in tumor at 4 h. It is also demonstrated that the main mechanism for the tumor uptake of PdCu@Au tripods is still the EPR effect in the first few hours after the injection, regardless of their surface modification. However, the active targeting effect brought by DAPTA peptides was clearly demonstrated at 24 h, with 11.2 ± 0.22 %ID/g of tripods accumulated in the tumor sites, significantly higher than that of the non-targeted groups (6.83 ± 0.42 %ID/g) or the targeting efficiency for other types of non-targeted Au nanoparticles.[3] Importantly, the selectivity in tumor targeting was also improved by DAPTA conjugation that could be observed from the elevated tumor-to-blood ratio of 5.70 ± 2.63 and tumor-to-muscle ratio of 28.6 ± 5.27 of the DAPTA-conjugated PdCu@Au tripods. These number were 2.1-fold and 4.4-fold higher than the measure from PEGylated tripods (1.82 ± 0.43, $p < 0.05$ and 5.28 ± 1.45, $p < 0.005$, respectively), clearly illustrating the feasibility using CCR5 as new cancer biomarker, as well as the effectiveness of the targeting technology.

2.2.5 PET Imaging

In addition, I further preformed the *in vivo* PET imaging to quantitatively assess the feasibility using $Pd^{64}Cu$@Au tripods as contrast agents for cancer diagnosis. The experiment was conducted on 4T1 tumor bearing mice models 24 post injection. Both groups of the PdCu@Au tripods were find to highly accumulate in tumor sites as well as liver and spleen in agreement with the biodistribution data mentioned beforehand (Figure 2.10a.). The non-targeted PdCu@Au tripods demonstrated a heterogeneous distribution in tumor with a standard uptake value (SUV) of 1.47 ± 0.16 and tumor-to-muscle ratio of 4.84 ± 0.67 (Figure 2.10 b and c, respectively). With DAPTA conjugated to the PdCu@Au tripods, the SUV on tumor site was increased by 50% to 2.18 ± 0.16 comparing to their

PEGylated counterpart. The selectivity in tumor targeting was also increased, represented by the high tumor-to-muscle ratio of 32.7 ± 4.19, which was almost seven times as high as that from the PEGylated tripods. The outstanding tumor targeting selectivity of the targeting technology was also testified by a competitive blocking experiment where DAPTA-conjugated non-radioactive tripods were injected along with the DAPTA-conjugated radioactive tripods at a molar ratio of 9 : 1 (non-radioactive : radioactive). The tumor uptake and tumor-to-muscle ratio were significantly reduced (1.59 ± 0.05, $p < 0.005$ and 7.89 ± 1.40, $p < 0.001$, respectively), which confirmed the feasibility as well as the high efficiency and selectivity of using DAPTA peptides to target novel cancer biomarker of CCR5. It is worth pointing out that there were very low signals from the bladder of all mice indicating a reduced renal clearance during the entire study and outstanding stability. This result also testifies the reliability of the radiolabeling strategy reported previously.[33]

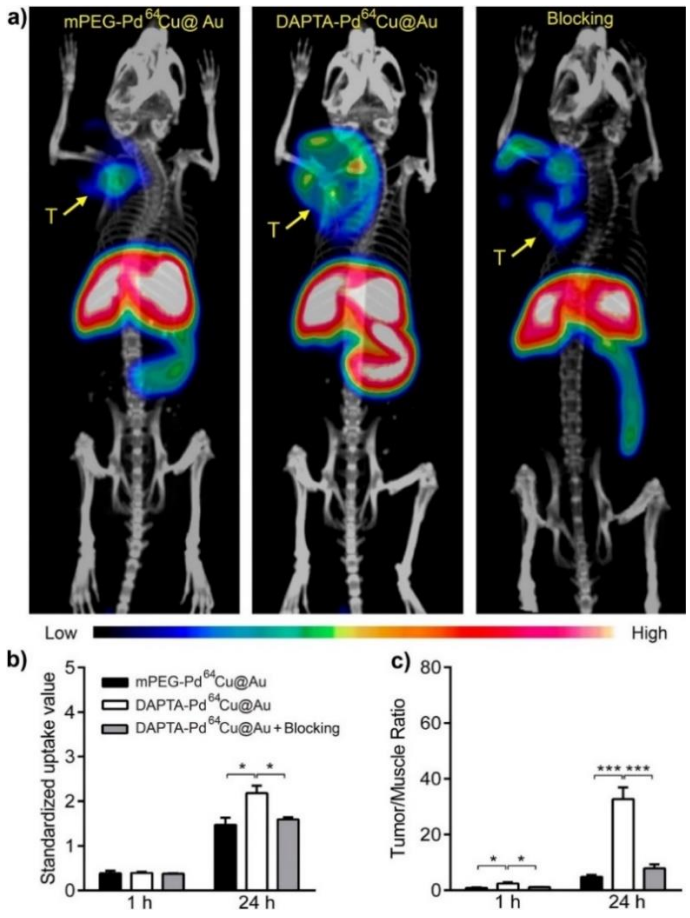

Figure 2.10. Micro PET/CT images of 4T1 tumor-bearing mouse injected with a) Cu-64 doped DAPTA-conjugated $Pd^{64}Cu$@Au tripods (left); Cu-64 doped PEGylated $Pd^{64}Cu$@Au tripods (middle); DAPTA-conjugated $Pd^{64}Cu$@Au tripods with 9 times of non-radioactive counterpart as blocking (right). Each mouse was injected with 3.7 MBq radionuclides. PET scanning was performed at 24 post-injection. T: tumor; L: liver. b) The SUV in tumor sites calculated from the PET/CT images by summing up the SUV in selected region of interest. c) Tumor-to-muscle SUV ratios calculated from the PET/CT images. * $p < 0.05$; *** $p < 0.001$.

As the intratumoral distribution could greatly affect the drug delivery efficiency of nanoparticles, I further assessed the intratumoral distribution of the Cu-64 doped $Pd^{64}Cu$@Au tripods using autoradiography. Tumors were collected from the mice after PET imaging at 24 h post injection and sectioned into 40 μm slices. As shown in Figure 2.11, the autoradiography images showed a heterogeneous intratumoral distributions for

PdCu@Au tripods with or without DAPTA conjugation, in good consistence with the results revealed by PET images.

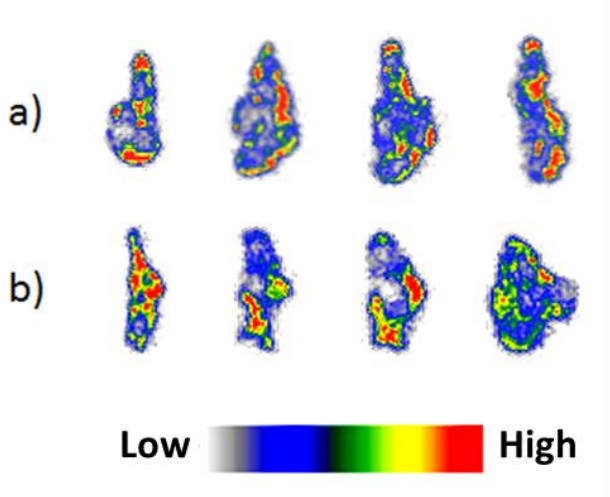

Figure 2.11. The heterogeneous intratumoral distributions shown by auto-radiography of the tumor slices. a) DAPTA-conjugated PdCu@Au tripods, and b) non-targeted PEGylated tripods.

2.2.6 CCR5-Targeted Photothermal Cancer Treatment Guided by PET Imaging

As a critical next step for theranostic agents, the use of imaging result as guidance to the treatment needs to be demonstrated. Following this direction, I illustrated the photothermal therapy of cancer under the guidance of CCR5-targeted PET imaging in 4T1 tumor bearing mice model. After the PET imaging at 24 h post-injection, the tumor bearing mice injected with 0.47 mg radioactive and 4.23 mg non-radioactive DAPTA-conjugated PdCu@Au tripods were subjected to photothermal treatment. According to the quantitative PET imaging result, about 0.33 ± 0.08 mg of PdCu@Au tripods could be delivered to tumor site, given the tumor uptake of 7.29 ± 0.23 %ID/g. As shown in Figure 2.12 a, the whole body thermographic images taken by IR camera reveals a quick increase of temperature at the tumor site under irradiation of 808 nm laser at 1.2 W/cm^2. After 2 min of laser

irradiation, the temperature at the tumor sites dramatically increased by 21.8 °C and reached 60.7 ± 2.3 °C after 3 min (Figure 2.12b). This *in vivo* photothermal heating profile was much better comparing to our previous report on other kinds of Au nanoparticles.[3] At the same time, the saline injected control group only showed a modest increase in temperature (5.7 ± 2.5 °C) even after 10 min of irradiation.

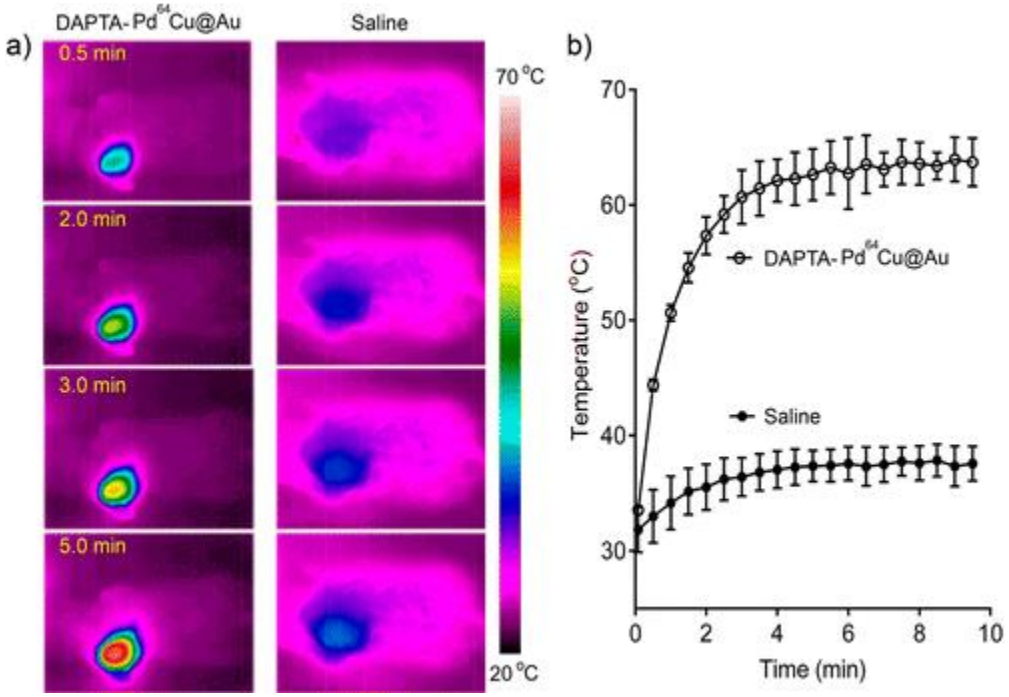

Figure 2.12. a) Whole body thermographs of the tumor-bearing mice during the process of photothermal therapy. The mice were either administrated with DAPTA-conjugated PdCu@Au tripods or saline. b) The photothermal heating profiles quantified from the thermographs, showing the temperature increase on tumor sites as a function of irradiation time. The power density of laser was 1.2 W/cm^2. Error bars stands for the standard errors from 3 mice.

The treatment effect of PET guided photothermal therapy were evaluated by PET imaging of ^{18}F-flourodeoxyglucose (^{18}F-FDG) to assess the tumor metabolism at 48 h post irradiation. The DAPTA-conjugated PdCu@Au tripod treated mice were shown to have a decreased tumor uptake of ^{18}F-FDG comparing to the saline injected control group (Figure

2.13a). By quantification of the SUV from PET images, the tumor bearing mice treated by DAPTA-conjugated tripods demonstrated a five-times lower ($p < 0.005$, $n = 3$) uptake of ^{18}F-FDG (0.13 ± 0.02), in contrast to that of the saline injected control mice (0.82 ± 0.21). This therapeutic effect evaluated by ^{18}F-FDG PET/CT was comparable to that reported previously using other kinds of Au nanoparticles.[3] However, this comparable treatment effect was achieved by DAPTA-conjugated PdCu@Au tripods with about 60 % less dosage of particle, in terms of mess dose, indicating an improved tumor targeting efficiency *via* the use of CCR5 as novel cancer biomarker and DAPTA as targeting ligand. Taken together, the DAPTA-conjugated PdCu@Au tripods possess comparable photothermal conversion efficiency to other kinds of Au nanoparticles,[34-36] along with a 50-60 % higher tumor uptake than their PEGylated counterparts in biodistribution and PET imaging, I demonstrated the proof-of-concept study of the use of CCR5 as novel cancer biomarker for the diagnosis and treatment of triple negative breast cancer in mice 4T1 breast cancer model. Future study should focus on the improvement of targeting efficiency as well as the optimization of treatment protocols aiming at the further reduction of the dose needed for PET imaging and cancer treatment.

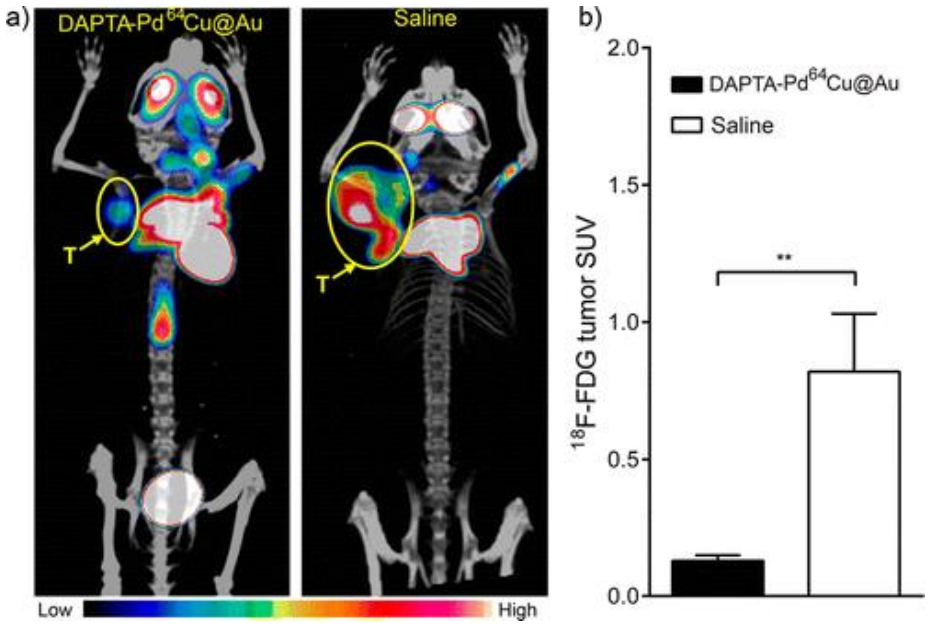

Figure 2.13. a) ^{18}F-FDG PET/CT imaging showing the metabolism of 4T1 triple negative breast cancer after photothermal treatment. A lower uptake of ^{18}F-FDG is shown in the mice administrated with DAPTA-conjugated tripods than that from the saline injected control group. b) The SUV of ^{18}F-FDG obtained from the PET/CT images with n=3. ** p < 0.005.

2.2.7 Biological Assessments

To verify the existence and assess the expression level of CCR5 on the 4T1 tumor model, I further preformed the biological assessments. As shown in Figure 2.14 a, the hematoxylin and eosin (H&E) staining shows the morphology of cancerous cells in the tumor tissue collected after 2 weeks of implantation. The up regulation of CCR5 was found on cell membranes and in nuclei indicated by the immunohistochemistry shown in Figure 2.14 b. This up regulation was also quantified by western blot and RT-PCR against the β-actin at 2 and 4 weeks post implant (Figure 2.14, c and d). The expression level of CCR5 was find to dramatically increased during the progression of tumor demonstrating a great potential to be a biomarker for cancer progression.

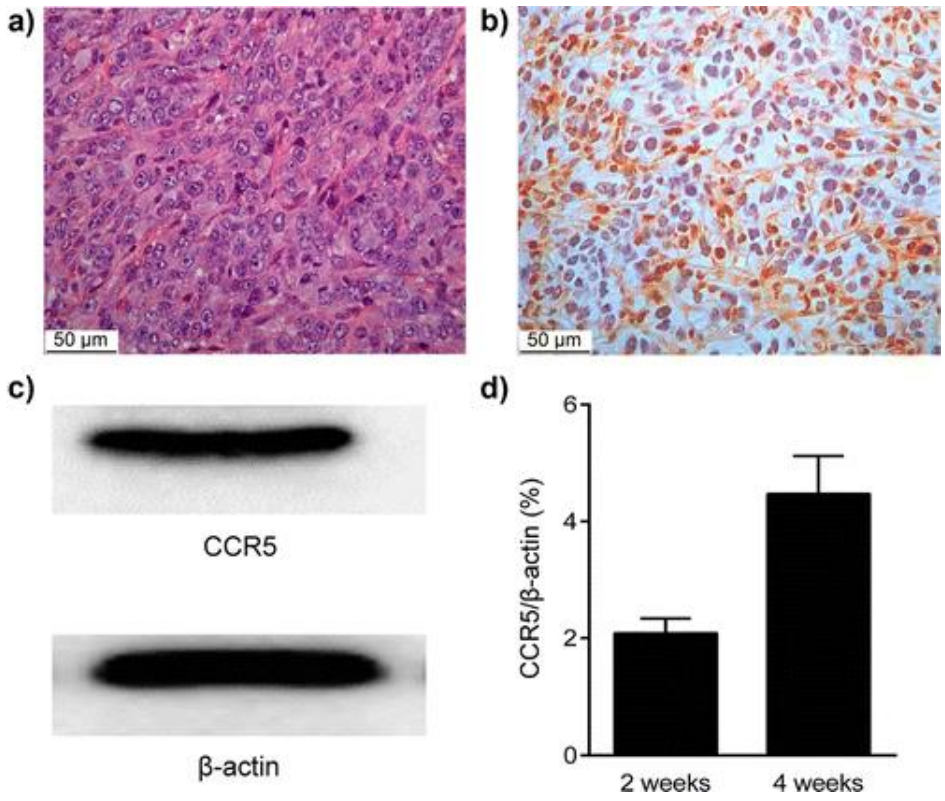

Figure 2.14. Biological data showing the up regulation of CCR5 in 4T1 tumor. (a) The morphology of 4T1-Luc primary cancer cells shown by H&E staining at 2 weeks. (b) Immunohistochemistry staining of tumor cells for CCR5 (brown) and hematoxylin (blue) at 2 weeks. The expression of CCR5 was shown at both the membranes and nuclei of the cells. (c) The elevated expression of CCR5 verified by western blot in 4T1 tumor cells. (d) Quantitative RT-PCR data showing the increasing expression of CCR5 along the cancer progression in 4 weeks. Data was normalized against the expression of *β*-actin.

According to current research, CCL5 promotes the progression of diseases by recruiting inflammatory cells and modulating their activities through the interaction with CCR5.[37-40] As shown in preclinical studies, the pulmonary metastasis could be suppressed by antagonist blocking of CCR5, indicating a great potential on their use as therapeutic agents in addition to the role of cancer progression biomarker.[41, 42] This study illustrates the feasibility to target this novel biomarker in a triple negative breast cancer tumor model using DAPTA peptides conjugation. This work testifies that it is viable for the DAPTA

peptides conjugated PdCu@Au tripods to act as platforms for cancer diagnosis and treatment.

2.3 Summary

In this chapter, I demonstrated the controlled synthesis and surface modification of PdCu@Au tripods. With radioactive Cu-64 directly incorporated into the crystal lattice, the use of $Pd^{64}Cu$@Au tripods for targeted cancer imaging and PET guided photothermal therapy were also demonstrated. Their novel anisotropic structure allows them a readily tunable LSPR peak in the NIR range with a large absorption to scattering ratio validated by both numerical simulation and photothermal generation experiment. By the conformal coating of the PdCu tripod cores, the Cu-64 could be fixed into the crystal lattice of the tripods with outstanding stability, and the cytotoxicity could be controlled to a low level. When DAPTA peptides were conjugated, the PdCu@Au tripods could be specifically delivered to the tumor sight with the active targeting capability to CCR5. With the capability to be quantitatively monitored by PET imaging, the DAPTA-conjugated Cu-64 doped PdCu@Au tripods could be used to precisely diagnose cancer and to guide the therapy. In summary, I have demonstrated the capability of $Pd^{64}Cu$@Au tripods as a novel multifunctional platform for image-guided cancer theranostics.

2.4 Experimental

2.4.1 Chemicals and Reagents

Orthopyridyldisulfide-poly(ethylene glycol)-N-hydroxysuccinimide (OPSS-PEG_{5000}-SVA, MW ≈ 5,000) and poly(ethylene glycol)monomethyl ether thiol ($mPEG_{5000}$-

SH, MW ≈ 5,000) and were purchased from Laysan Bio (Arab, AL). DAPTA (D-A1STTTNYT-NH_2) were obtained as customized product from CPC Scientific (Sunnyvale, CA). Other chemicals and reagents, including Na_2PdCl_4 (99.998%), $CuCl_2 \cdot 2H_2O$, KBr, PVP (MW ≈ 55,000), AA, dimethyl sulphoxide (DMSO), MTT, and DPBS were obtained from Sigma-Aldrich (St. Louis, MO). All chemicals were used as received.

2.4.2 Synthesis of the PdCu Alloy Tripods

The PdCu bimetallic tripods were first synthesized following the protocol previously reported by our group.[18] In a typical synthesis, 3 mL of aqueous solution containing 3 mg $CuCl_2 \cdot 2H_2O$, 20 mg AA, 35 mg PVP, and 175 mg KBr were preheated in a 20 mL glass vial at 80 °C under magnetic stirring. After 10 min, 19 mg Na_2PdCl_4 in 1 mL ultrapure water was introduced into the reaction solution. The reaction was then allowed to carry on for 2 h at 80 °C with the cap of the vial loosely capped. The reaction was stopped by rapidly cooling down the vial in ice bath, and the product was collected and washed by centrifuge. After three times of washing (8500 g, 30 min) with ultrapure water, the product was re-dispersed into 4 mL of ultrapure water as stock suspension for further use. Radioactive $Pd^{64}Cu$ bimetallic tripods were synthesized with a similar procedure at a smaller scale (1/4 scale), by introduce trace amount of $^{64}CuCl_2$ during the preheating. Specifically, 1280 MBq of $^{64}CuCl_2$ was added into 0.75 mL of the preheated solution prior to the addition of 0.25 mL Na_2PdCl_4 (19 mg/mL). The purified radioactive $Pd^{64}Cu$ tripods was re-dispersed in 1 mL of ultrapure water and used as a stock suspension for Au coating. The $^{64}CuCl_2$ used in this synthesis was obtained from the CS-15 cyclotron

facility at the Washington University Medical School according to the published procedures.[43]

2.4.3 Synthesis of the Radioactive PdCu@Au Core-shell Tripods

The PdCu@Au tripods were obtained with or without radioactivity by the conformal coating of a Au shell on the surface of PdCu bimetallic tripod. With PVP as a colloidal stabilizer, $HAuCl_4$ was chemically reduced by AA in the suspension of PdCu bimetallic tripods. Specifically, in a 250 mL flask, each 1 mL of the stock suspension of PdCu tripods was added into 50 mL aqueous solution containing 1.4 g AA and 240 mg PVP under vigorous stir. Subsequentially, 0.5 mM $HAuCl_4$ was dropwisely added into the mixture at room temperature with the help of a syringe pump at 40 mL/h. The UV-vis-NIR spectra of the reaction suspension were frequently measured to monitor the position of its main LSPR peak. When the LSPR peak was blue-shifted to *ca.* 810 nm (120 mL $HAuCl_4$), the reaction was stopped. The product was then collected, washed with ultrapure water by centrifuge, and re-dispersed into 1 mL DPBS to a particle concentration of 12.1 nM (estimated from the ICP-MS and TEM data). The measurement of particle concentration was conducted by measure the total amount of Pd and Cu content in the suspension, as the size and shape of the PdCu alloy core are more uniform than the PdCu@Au particles.

2.4.4 Preparation of OPSS-PEG$_{5000}$-DAPTA

Before the surface modification, the OPSS-PEG_{5000}-DAPTA molecules were first synthesized by conjugating the DAPTA onto PEG N-Hydroxysuccinimide (NHS) ester derivative of OPSS-PEG_{5000}-SVA with their primary amine group. In a typical synthesis,

the OPSS-PEG_{5000}-SVA was mixed with DAPTA peptides in DPBS at a molar ratio of 1:5 to react overnight at 4 ºC. The resulted mixture was used without further purification.

2.4.5 Conjugation of PEG and PEG-DAPTA with the PdCu@Au Tripods

The PEGylation was conducted by incubating $mPEG_{5000}$-SH or a mixture of $mPEG_{5000}$-SH and OPSS-PEG_{5000}-DAPTA (molar ration of 5 : 1) with the stock suspension containing PdCu@Au tripods at a molar ration of (tripod : PEG = 1 : 100,000). In a typical process, 1 mL of the stock suspension was mixed with 4 mL of aqueous solution containing 7 mg of $mPEG_{5000}$-SH or a mixture of 1.6 mg OPSS-PEG_{5000}-DAPTA and 5.4 mg $mPEG_{5000}$-SH. The conjugation was allowed to react at room temperature overnight on shaker. Excess OPSS-PEG_{5000}-DAPTA and/or $mPEG_{5000}$-SH were removed from the product with three times of washing with ultrapure water. The product was harvested with centrifugation and re-dispersed in saline for animal study.

2.4.6 Numerical Simulation of the LSPR Spectra

The extinction spectra of PdCu@Au tripod was also studied by numerical simulation with the 3D-FDTD method to calculate the scattering and absorption spectra.[29] In this particular study, I only foucsd on the calculation of longitudinal mode of the LSPR peaks. In the modeling, the arm length of the PdCu bimetallic core was set to 25 or 35 nm, with a diameter of 6 nm. The spectra were calculated with Au shell thickness of 2 to 4, 6, and 8 nm for both arm lengths.

2.4.7 Evaluation of the Photothermal Effect In Vitro

To evaluate the photothermal generation capability of PdCu@Au tripods, 100 μL DPBS with (100−400 pM) or without PdCu@Au tripods were dispensed in separate wells on a 96-well plate. The suspensions were irradiated by a diode laser (λ = 808 nm, Power Technology, Alexander, AR) from the top at 0.25 to 1.0 W/cm^2, while the temperature changes were monitored with a NIR camera (ICI7320, Infrared Camera, Beaumont, TX). Series of images were captured and the average temperature was readout from the thermograph using IR Flash software (Infrared Camera, version 2.10).

2.4.8 Cell Culture

The 4T1 breast cancer cell line was purchased from the American Type Culture Collection (ATCC, Manassas, VA, USA). The cells were cultured using Dulbecco's Modified Eagle Medium (DMEM) with 10% fetal bovine serum and 1% penicillin/streptomycin, in a humidified atmosphere containing 5% CO_2 at 37 °C.

2.4.9 Cell Growth Inhibition Assay In Vitro

A standard MTT assay was performed to quantify the cytotoxicity of PdCu@Au tripods. In a typical experiment, 4T1 breast cancer cells were cultured in 96-well plate at a density of 1×10^4 cells/well. After washing with DPBS, 100 μL fresh culture medium containing PEGylated or DAPTA-conjugated PdCu@Au tripods were introduced to a final concentration of 6.25 to 800 pM. Subsequentially, 25 μL of MTT stock solution (5 mg/mL in DPBS) was added to each well after 24 h of incubation. The cells were washed with DPBS after 2 h of incubation. And the formazan crystals were then dissolved in 100 μL

extraction solution (40% isopropanol in DMSO, v/v %) at 37 °C. The absorbance at 570 nm were taken by plate reader (Infinite F200 Pro, Tecan, Switzerland) and normalized to the untreated control group.

2.4.10 Cell Uptake of the PdCu@Au Tripods Measured by ICP-MS

Cell uptake experiment were conducted on 24-well plates with 5×10^5 cells in each well. After washing with DPBS, 1 mL fresh culture medium containing PEGylated or DAPTA-conjugated PdCu@Au tripods were introduced to a final concentration of 200 pM. After 3 times of washing with DPBS, the cells were harvested at a series of time points. After the cells were dried, 300 μL aqua regia was added to completely digest the metal content in each sample. The metal contents of Au, Pd, and Cu were quantified using ICP-MS. Together with TEM measurement, the metal contents were converted to the particle numbers.

2.4.11 Mouse Tumor Model

The 4T1 tumor bearing mice model were prepared by injecting 100 μL saline containing 5×10^6 cells subcutaneously into the right fat pad of female BALB/c mice weighing 15−20 g (7-week old). The tumors were allowed to grow to a size of 200−300 mm^3 before further animal study. All the protocols for animal studies were approved by the Washington University Animal Studies Committee.

2.4.12 Pharmacokinetics and Biodistribution

In the pharmacokinetics and biodistribution study, each mouse was injected with 100 μL saline containing 47 μg PEGylayed or DAPTA-conjugated PdCu@Au tripods

(doped with 370 kBq Cu-64 /mouse) *via* the tail vein. At series time points (1, 4, and 24 h post injection), the mice were sacrificed by cervical dislocation after anesthesia. Organs of interest were than collected, weighed, and subjected to γ counting using a Beckman 8000 gamma counter (Beckman, Fullerton, CA). The weight-normalized dosage was calculated as percentage of the %ID/g for each kinds of organ.

2.4.13 PET Imaging of the PdCu@Au Tripods In Vivo

Before the PET imaging, PEGylayed or DAPTA-conjugated PdCu@Au tripods (3.70 MBq, 470 μg/mouse) were intravenously injected to two groups of 4T1 tumor-bearing mice (n = 3) in 100 μL saline. For the blocking group, the mice were intravenously injected with 100 μL of saline containing both radioactive (3.70 MBq) and non-radioactive DAPTA-conjugated PdCu@Au tripods at a molar ratio of 1 : 9, with total mass of 4700 μg/mouse. At a series of time points, PET/CT images were acquired with microPET Focus 220 (Siemens, Malvern, PA) or Inveon PET/CT system (Siemens, Malvern, PA). The PET instruments were cross-calibrated prior to the experiment. The tumor uptake of particles and SUV were determined from the images following our previous reported protocols.[3]

2.4.14 Autoradiographic Imaging

Tumors were dislocated from the mice after PET imaging (24 h post injection) and fixed in 4% paraformaldehyde. The tumors were frozen in optimal cutting temperature compound and sectioned into slices of 50 μm in thickness. The tumor slices were sealed to glass slides before subjecting to 2D autoradiography (InstantImager Electronic Autoradiography, Packard, Meriden, CT).

2.4.15 Targeted Photothermal Cancer Treatment In Vivo

After locate the tumor site with PET/CT imaging, the mice used for the blocking study were subjected to photothermal therapy. At 24 h post injection, the mice were anesthetized. The tumors were irradiated with a diode laser (λ = 808 nm, Power Technology, Alexander, AR) setting at 1.2 W/cm^2 for 10 min. The temperature profiles over the entire therapy were continuously monitored by NIR camera (ICI7320, Infrared Camera, Beaumont, TX). 4T1 tumor-bearing mice injected with 100 μL saline were employed as control.

2.4.16 Evaluation of Photothermal Treatment with ^{18}F-FDG PET/CT Imaging

The therapeutic effect of photothermal therapy was evaluated 24 h post treatment using ^{18}F-FDG (obtained from the Washington University cyclotron facility) PET/CT imaging to quantify the tumor metabolism. The mice were anesthetized and injected with 100 μL saline 3.7 MBq ^{18}F-FDG through the tail vein. At 1 h post injection, PET/CT images were acquired with microPET Focus 220 (Siemens, Malvern, PA) or Inveon PET/CT system (Siemens, Malvern, PA). The PET instruments were cross-calibrated prior to the experiment. The tumor uptake of ^{18}F-FDG and SUV were determined from the images following our previous reported protocols.[3]

2.4.17 Immunohistochemistry and Histologic Quantification

For the histochemistry assays, paraformaldehyde-fixed (24 h) and paraffin-embedded samples were sliced into a series sections of 5 μm thick. Before the antibody staining, a series of xylenes and graded alcohols treatments were conducted for the

deparaffinization and rehydration of specimens. Antigen retrieval pretreatment (10×10^{-3} m Tris, 1×10^{-3} m ethylenediaminetetraacetic acid, 0.05% Tween, and at pH = 9.0 for 10 min) was then conducted. To prevent nonspecific binding, all the slides were treated with 0.3% H_2O_2 for 30 min, and blocking serum for 1 h (Vectastain, Vector Laboratories, Burlingame, CA). Antibody staining was then carried out by incubating a primary antibody (anti-CCR5, 1 : 100 in blocking serum, Santa Cruz Biotechnology, Dallas, TX) at 4 °C overnight. After the staining of secondary antibody (Vector Laboratories) a horse radish peroxidase-based immunostaining kit (Vector Laboratories) was employed to develop a brown color. Counterstaining of nuclei was accomplished with hematoxylin for a blue color. Images were acquired with a light microscope (Leica Microsystems). Routine H&E staining was also performed on the slides to analyze the morphology of the tissue.

2.4.18 Real-time PCR Assay

The RNA was isolated using TRIzol (Invitrogen, Carlsbad, CA) following the manufacturer's protocol from 4T1-Luc tumors was used for real-time PCR. For the reverse transcription reactions, 1 µg RNA, random hexamer priming, and Superscript II reverse transcriptase (Invitrogen) were employed. Taqman assays (Invitrogen) and an EcoTM Real-Time PCR System (Illumina, San Diego, CA) were used to quantify the expression of CCR5 and *β*-actin with cycling conditions set as: 50 °C for 2 min, 95 °C for 21 s, and 60 °C for 20 s. The of *β*-actin was also quantified and used as a comparator for DD Ct calculations.

2.4.19 Western Blot

For the western blot, 4T1 tumors and organ tissues were frozen and homogenized in NP40 buffer (50 mM Tris pH 8.0, 150 mM NaCl, 1% NP-40) supplemented with protease inhibitor cocktail (Sigma-Aldrich, St. Louis, MO). The mixtures were centrifuged at 4 °C. before the supernatant, the protein extract, was collected and measured using the Bio-rad protein assay (Bio-rad, Hercules, CA). From each sample, 80 µg of proteins was separated on a sodium dodecyl sulfate sodium salt-polyacrylamide gel electrophoresis and then electrophoretically transferred onto nitrocellulose membrane (Bio-rad, Hercules, CA). The membranes were treated with PBS-T (0.1% Tween-20 in PBS) containing 5% non-fat milk powder for 1 h for the inhibition of non-specific binding. Antibody staining was carried out with rabbit anti-CCR5 antibodies (dilution 1 : 2500, Santa Cruz, Dallas, TX) at 4 °C overnight. Then, the membranes were developed with horseradish peroxidase-linked antirabbit IgG (dilution 1 : 5000; GE Healthcare Bio-Sciences, Pittsburgh, PA) for 45 min at room temperature after washing with PBS-T. The chemiluminescence were quantified with ECL substrate (GE Healthcare Bio-Sciences, Pittsburgh, PA) for 1 min, with images captured immediately. The expression level of β-actin was measured, and set as internal standard in parallel blots.

2.4.20 Instrumentation

The UV-vis-NIR spectra were acquired using a UV-vis-NIR spectrometer (Lambda 750, PerkinElmer, Waltham, MA) with wavelengths set to 400-1200 nm. Radio-TLC was conducted with radioactive instant thin layer chromatography (Radio-ITLC, Bioscan, Washington, DC). The size and morphology of nanoparticles were directly visualized with

TEM (Hitachi HT7700, Hitachi, Japan) operating at 120 kV. For the radioactive Cu-64 doped tripods, samples were left to decay for 90 days (170 half-lives) before deposited to nickel grid. The metal contents were measured by ICP-MS (NexION 300Q, PerkinElmer, Waltham, MA).

2.5 References

[1] Li, N.; Zhao, P.; Astruc, D. Anisotropic gold nanoparticles: synthesis, properties, applications, and toxicity. *Angew. Chem. Int. Ed.* **2014**, 53, 1756–1789.

[2] Yang, X.; Yang, M.; Pang, B.; Vara, M.; Xia, Y. Gold Nanomaterials at work in biomedicine. *Chem. Rev.* **2015**, 115, 10410–10488.

[3] Wang, Y.; Black, K.C.L.; Luehmann, H.; Li, W.; Zhang, Y.; Cai, X.; *et al*. Comparison study of gold nanohexapods, nanorods, and nanocages for photothermal cancer treatment. *ACS Nano* **2013**, 7, 2068–2077.

[4] Rodriguez-Lorenzo, L.; Alvarez-Puebla, R.A.; de Abajo, F.J.G.; Liz-Marzan, L.M. Surface enhanced raman scattering using star-shaped gold colloidal nanoparticles. *J. Phys. Chem. C* **2010**, 114, 7336–7340.

[5] Nikoobakht, B.; El-Sayed, M.A. Preparation and growth mechanism of gold nanorods (NRs) using seed-mediated growth method. *Chem. Mater.* **2003**, 15, 1957–1962.

[6] Ralph, W. A clearer vision for *in vivo* imaging. *Nat. Biotechnol.* **2001**, 19, 316–317.

[7] Jain, P.K.; Huang, X.; El-Sayed, I.H.; El-Sayed, M.A. Noble metals on the nanoscale: optical and photothermal properties and some applications in imaging, sensing, biology, and medicine. *Accounts Chem. Res.* **2008**, 41, 1578–1586.

[8] Dreaden, E.C.; Alkilany, A.M.; Huang, X.; Murphy, C.J.; El-Sayed, M.A. The golden age: gold nanoparticles for biomedicine. *Chem. Soc. Rev.* **2012**, 41, 2740–2779.

[9] Cobley, C.M.; Chen, J.; Cho, E.C.; Wang, L.V.; Xia, Y. Gold nanostructures: a class of multifunctional materials for biomedical applications. *Chem. Soc. Rev.* **2011**, 40, 44–56.

[10] Hu, M.; Chen, J.; Li, Z-Y.; Au, L.; Hartland, G.V.; Li, X.; *et al*. Gold nanostructures: engineering their plasmonic properties for biomedical applications. *Chem. Soc. Rev.* **2006**, 35, 1084–1094.

[11] Cho, E.C.; Kim, C.; Zhou, F.; Cobley, C.M.; Song, K.H.; Chen, J.; *et al*. Measuring the optical absorption cross-sections of Au-Ag nanocages and Au nanorods by photoacoustic imaging. *J. Phys. Chem. C* **2009**, 113, 9023–9028.

[12] Sun, T.; Zhang, Y.S.; Pang, B.; Hyun, D.C.; Yang, M.; Xia, Y. Engineered nanoparticles for drug delivery in cancer therapy. *Angew. Chem. Int. Ed.* **2014**, 53, 12320–12364.

[13] Black, K.C.L.; Wang, Y.; Luehmann, H.P.; Cai, X.; Xing, W.; Pang, B.; *et al*. Radioactive ^{198}Au-doped nanostructures with different shapes for *in vivo* analyses of their biodistribution, tumor uptake, and intratumoral distribution. *ACS Nano* **2014**, 8, 4385–4394.

[14] Wang, Y.; Liu, Y.; Luehmann, H.; Xia, X.; Brown, P.; Jarreau, C.; *et al*. Evaluating the pharmacokinetics and *in vivo* cancer targeting capability of Au nanocages by positron emission tomography imaging. *ACS Nano* **2012**, 6, 5880–5888.

[15] Zhao, Y.; Sultan, D.; Detering, L.; Luehmann, H.; Liu, Y. Facile synthesis, pharmacokinetic and systemic clearance evaluation, and positron emission tomography cancer imaging of ^{64}Cu-Au alloy nanoclusters. *Nanoscale* **2014**, 6, 13501–13509.

[16] Zhao, Y.; Sultan, D.; Detering, L.; Cho, S.; Sun, G.; Pierce, R.; *et al*. Copper-64-alloyed gold nanoparticles for cancer imaging: improved radiolabel stability and diagnostic accuracy. *Angew. Chem. Int. Ed.* **2014**, 53, 156–159.

[17] Sun, X.; Huang, X.; Yan, X.; Wang, Y.; Guo, J.; Jacobson, O.; *et al*. Chelator-free ^{64}Cu-integrated gold nanomaterials for positron emission tomography imaging guided photothermal cancer therapy. *ACS Nano* **2014**, 8, 8438–8446.

[18] Zhang, L.; Choi, S-I.; Tao, J.; Peng, H-C.; Xie, S.; Zhu, Y.; *et al*. Pd–Cu bimetallic tripods: a mechanistic understanding of the synthesis and their enhanced electrocatalytic activity for formic acid oxidation. *Adv. Funct. Mater*. **2014**, 24, 7520–7529.

[19] Wang, Y.; Liu, Y.; Luehmann, H.; Xia, X.; Wan, D.; Cutler, C.; *et al*. Radioluminescent gold nanocages with controlled radioactivity for real-time *in vivo* imaging. *Nano Lett.* **2013**, 13, 581–585.

[20] Stewart B.W.; Wild, C.P. *World Cancer Report 2014*. International Agency for Research on Cancer. Lyon, France 2014.

[21] Specht, J.M.; Mankoff, D.A. Advances in molecular imaging for breast cancer detection and characterization. *Breast Cancer Res.* **2012**, 14, 206.

[22] Mankoff, D.A.; Link, J.M.; Linden, H.M.; Sundararajan, L.; Krohn, K.A. Molecular imaging of cancer: from molecules to humans. *J. Nucl. Med.* **2008**, 49, 149S-163S.

[23] Banin Hirata, B.K.; Oda, J.M.; Losi Guembarovski, R.; Ariza, C.B.; de Oliveira, C.E.; Watanabe, M.A. Molecular markers for breast cancer: prediction on tumor behavior. *Dis. Markers* **2014**, 2014, 513158.

[24] Trop, I.; LeBlanc, S.M.; David, J.; Lalonde, L.; Tran-Thanh, D.; Labelle, M.; *et al*. Molecular classification of infiltrating breast cancer: toward personalized therapy. *Radiographics* **2014**, 34, 1178–1195.

[25] Schmadeka, R.; Harmon, B.E.; Singh, M. Triple-negative breast carcinoma: current and emerging concepts. *Am. J. Clin. Pathol.* **2014**; 141; 462–477.

[26] Velasco-Velazquez, M.; Pestell, R.G. The CCL5/CCR5 axis promotes metastasis in basal breast cancer. *Oncoimmunology* **2013**, 2, e23660.

[27] Soria, G.; Ben-Baruch, A. The inflammatory chemokines CCL2 and CCL5 in breast cancer. *Cancer Lett.* **2008**, 267, 271–285.

[28] Pang, B.; Zhao, Y.; Luehmann, H.; Yang, X.; Detering, L.; You, M.; *et al*. ^{64}Cu-doped PdCu@Au tripods: a multifunctional nanomaterial for positron emission tomography and image-guided photothermal cancer treatment. *ACS Nano* **2016**, 10, 3121–3131.

[29] Oubre, C.; Nordlander, P. Optical properties of metallodielectric nanostructures calculated using the finite difference time domain method. *J. Phys. Chem. B* **2004**, 108, 17740–17747.

[30] Jaque, D.; Martinez Maestro, L.; del Rosal, B.; Haro-Gonzalez, P.; Benayas, A.; Plaza, J.L., *et al*. Nanoparticles for photothermal therapies. *Nanoscale* **2014**, 6, 9494–9530.

[31] Tong, L.; Cobley, C.M.; Chen, J.; Xia, Y.; Cheng, J-X. Bright three-photon luminescence from gold/silver alloyed nanostructures for bioimaging with negligible photothermal toxicity. *Angew. Chem. Int. Ed.* **2010**, 49, 3485–3488.

[32] Wang, Y.; Black, K.C.L.; Luehmann, H.; Li, W.; Zhang, Y.; Cai, X.; *et al*. A comparison study of gold nanohexapods, nanorods, and nanocages for photothermal cancer treatment. *ACS Nano* **2013**, 7, 2068–2077.

[33] Zhao, Y.; Sultan, D.; Detering, L.; Cho, S.; Sun, G.; Pierce, R.; *et al*. Copper-64-alloyed gold nanoparticles for cancer imaging: improved radiolabel stability and diagnostic accuracy. *Angew. Chem.* **2014**, 126, 160–163.

[34] Zhao, J.; Wallace, M.; Melancon, M.P. Cancer theranostics with gold nanoshells. *Nanomedicine (Lond.)* **2014**, 9, 2041–2057.

[35] Hwang, S.; Nam, J.; Jung, S.; Song, J.; Doh, H.; Kim, S. Gold nanoparticle-mediated photothermal therapy: current status and future perspective. *Nanomedicine (Lond.)* **2014**, 9, 2003–2022.

[36] You, J.; Zhang, R.; Xiong, C.; Zhong, M.; Melancon, M.; Gupta, S.; *et al*. Effective photothermal chemotherapy using doxorubicin-loaded gold nanospheres that target EphB4 receptors in tumors. *Cancer Res.* **2012**, 72, 4777–4786.

[37] Pakianathan, D.R.; Kuta, E.G.; Artis, D.R.; Skelton, N.J.; Hebert, C.A. Distinct but overlapping epitopes for the interaction of a CC-chemokine with CCR1, CCR3 and CCR5. *Biochemistry* **1997**, 36, 9642–9648.

[38] Niwa, Y.; Akamatsu, H.; Niwa, H.; Sumi, H.; Ozaki, Y.; Abe, A. Correlation of tissue and plasma RANTES levels with disease course in patients with breast or cervical cancer. *Clin. Cancer Res.* **2001**, 7, 285–289.

[39] Azenshtein, E.; Luboshits, G.; Shina, S.; Neumark, E.; Shahbazian, D.; Weil, M.; *et al*. The CC chemokine RANTES in breast carcinoma progression: regulation of expression and potential mechanisms of promalignant activity. *Cancer Res.* **2002**, 62, 1093–1102.

[40] Yaal-Hahoshen, N.; Shina, S.; Leider-Trejo, L.; Barnea, I.; Shabtai, E.L.; Azenshtein, E.; *et al*. The chemokine CCL5 as a potential prognostic factor predicting disease progression in stage II breast cancer patients. *Clin. Cancer Res.* **2006**, 12, 4474–4480.

[41] Velasco-Velazquez, M.; Jiao, X.; De La Fuente, M.; Pestell, T.G.; Ertel, A.; Lisanti, M.P.; *et al*. CCR5 antagonist blocks metastasis of basal breast cancer cells. *Cancer Res.* **2012**, 72, 3839–3850.

[42] Velasco-Velazquez, M.; Xolalpa, W.; Pestell, R.G. The potential to target CCL5/CCR5 in breast cancer. *Expert Opin. Ther. Targets* **2014**, 18, 1265–1275.

[43] McCarthy, D.W.; Shefer, R.E.; Klinkowstein, R.E.; Bass, L.A.; Margeneau, W.H.; Cutler, C.S.; *et al*. Efficient production of high specific activity ^{64}Cu using a biomedical cyclotron. *Nucl. Med. Biol.* **1997**, 24, 35–43.

CHAPTER 3. NANOTRIPODS AS CONTRAST AGENTS FOR TWO-PHOTON LUMINESCENCE IMAGING

3.1 Introduction

In this chapter, I further demonstrate the application of PdCu@Au tripods in optical imaging with their outstanding two-photon-luminescence property. I have presented our recent study on the synthesis and LSPR properties of PdCu@Au tripods, as well as their application on photothermal cancer therapy. In this chapter, I focus our research on other optical properties of PdCu@Au tripods, like two-photon luminescence property as well as their use in optical imaging.

Anisotropic Au nanostructures have received extensive research attention as they hold excellent optical properties, which are inherited from their morphologies. Although the syntheses of a few anisotropic Au nanostructures (Au nanorods, nanocages, nanoshells) have been established, the synthesis of Au nanostructure with branched arms still need to be explored.[1, 2] As summarized in chapter 2, I developed the PdCu@Au core-shell nanostructure with a novel tripod morphology. Their LSPR peak could be continuously tuned from 1000 to 800 nm by varying the thickness of Au coating. With the signature LSPR spectra, they also demonstrate large absorption to extinction ratio and a good photothermal generation capability.

Two-photon luminescence imaging utilized the non-linear effect of contrast agent to absorb two coherent photons for the excitation of photoluminescence.[1] To meet the requirement of coherence and high intensity, a femtosecond laser with wavelength in NIR

range was typically employed. It provides the two-photon imaging technology with a higher special resolution along with a deeper penetration in biological tissue. However, as the high intensity at the focal point could easily induce photo bleaching to the contrast agents, the development of stable contrast agents is of great necessity. The development of nanoparticle-based contrast agents (such as Au nanorods, quantum dots) have been reported to have an orders-of-magnitude-higher two-photon action cross section than that of organic dyes and a superior stability against photo bleaching.[3] As an outstanding example, Au nanorods could be imaged by two-photon luminescence imaging at single-particle level both i*n vitro* and *in vivo*. Their excitation mechanism has also been throughout studied. In a recent work by Xu and co-workers, the two-photon excitation process of Au nanorods was found to be the combination of two one-photon process.[4] Different from the organic dyes that absorb two coherent photons at the same time, the plasmatic Au nanorods were observed to sequentially absorb two photons with an actual intermediate state existing in between. The actual energy level of the intermediate state is provided by the *sp* energy band, while the LSPR could enhance the absorption of incident photons.

In this chapter, I demonstrated the two-photon luminescence imaging property of PdCu@Au tripods and their application in *in vitro* cancer cell imaging. With similar energy structure and LSPR future, I demonstrated the bright two-photon luminescence of PdCu@Au tripods. The PdCu@Au tripods were measured to have broad two-photon luminescence emission spectra with maximum emission at *ca.* 570 nm. By benchmarking to Au nanorods and organic dye of Rhodamine B, the PdCu@Au tripods were measured to have a two-photon action cross section of $1.83 \pm 0.15 \times 10^5$ GM (Göppert-Mayer, 1 GM =

1×10^{-50} cm^4s/photon), which is 3.6 ± 0.9 times higher than that from Au nanorods with same position on LSPR peak. This novel tripod structure was further demonstrated to have a good contrast enhancement capability in targeted cancer cell imaging. In combination with their LSPR properties and capability for Cu-64 incorporation and PET imaging, PdCu@Au tripods are expected to act as a new platform for cancer theranostic.

3.2 Results and Discussions

3.2.1 Preparation and Characterization of PdCu@Au Tripods

The PdCu@Au core-shell nanostructure studied in this research has a novel tripods morphology that is recently developed by our group.[5] It possesses a PdCu bimetallic core of tripod shape that is conformally coated by a uniform layer of Au. I modified our original synthesis of PdCu bimetallic tripods by employing nitrogen protection in the synthesis. In the modified protocol, 2 mL aqueous solution containing 38 mg Na_2PdCl_4 was introduced into 6 mL of pre-heated solution containing 6 mg $CuCl_2 \cdot 2H_2O$, 40 mg AA, 70 mg PVP, and 350 mg KBr. The reaction was then allowed to carry out under nitrogen protection at 80 °C for 2 h, before the product was harvested by centrifuge. The PdCu bimetallic tripods were prepared with high purity as well as good uniformity on arm number and arm length, with less small particle counterparts. It is hypothesized that the nitrogen protection could suppress the oxidative etching caused by the oxygen in atmosphere, preventing the breaking of particle arms. Measured by inductively coupled plasma-atomic emission spectrometer (ICP-AES) the synthetic yield, according to the metal contents, was found to increase from 20.3 % to 70.4 %. The length of the branched arms could be controlled with the amount of KBr and reaction time. In the current study, I used PdCu bimetallic tripods

with arm length of 25.4±4.1 nm and arm width of 5.4±0.8 nm for the preparation of PdCu@Au tripods (Figure 3.1a).

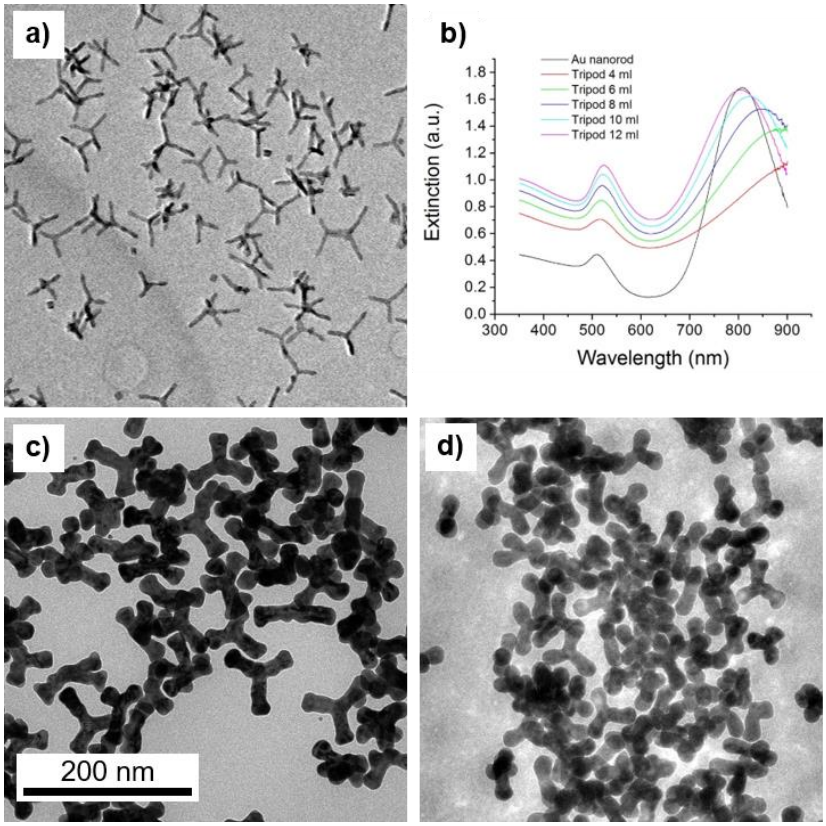

Figure 3.1. a) The TEM image of PdCu bimetallic tripods; b) the LSPR peaks of PdCu@Au tripods could be tuned by varying the amount of deposited Au. c) and d) shows the TEM image of PdCu@Au tripods corresponding to 12 mL and 6 mL in b), respectively.

The coating of PdCu bimetallic tripods was in turn conducted following our previous reported protocol. When a solution of $HAuCl_4$ (0.5 mM) was titrated into the aqueous suspension containing PdCu bimetallic tripods, AA, and PVP, the newly formed Au^0 atoms could conformally deposited onto the PdCu tripods creating a uniform Au coating. Along with the deposition of Au atoms, the main extinction peak, corresponding to the longitudinal mode of LSPR, could be continuously tuned in the NIR range from above 1,000 nm to *ca.* 800 nm. The reaction was immediately stopped once the main LSPR

peak reached the pre-determined wavelength. In this present study, I choose two kinds of PdCu@Au tripods with main LSPR peak at *ca.* 808 nm (Tripod 808) or *ca.* 880 nm (Tripod 880) for detailed assessment of their two-photon luminescence properties. The PdCu@Au tripods were characterized to have an average arm length of 45.3±5.6 nm and arm width of 24.1±3.0 nm for Tripod 808, as well as arm length of 35.3±4.5 nm and arm width of 19.3±1.8 nm for Tripod 880. (Figure 3.1 c,d) Commercially purchased citrate stabilized Au nanorods with a longitudinal peak centered at 809 nm and an average aspect ratio of 4.06 were acquired as benchmark. As shown in Figure 1b PdCu@Au demonstrated a similar UV-vis-NIR spectra with a slightly broader longitudinal peak. The PdCu@Au tripods were further conjugated to $mPEG_{5000}$-SH or FA-PEG_{5000}-SH for the following experiment.

3.2.2 Dependence of Two-Photon Luminescence on Excitation Intensity

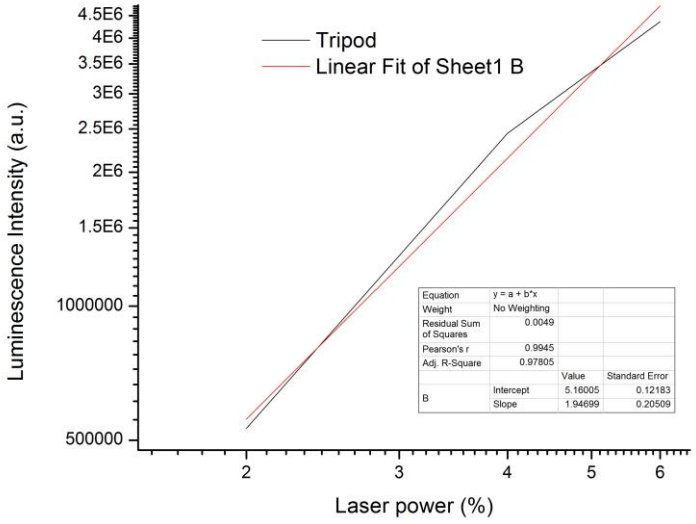

Figure 3.2. The two-photon luminescence intensity shows a Log-Linear dependency agent excitation power.

In the typical two-photon excitation process, contrast agents for two-photon imaging would absorb two photons from the coherent light to excite an electron from the ground state to the excited state. As such, the probability for an electron to be excited is proportional to the square of the intensity of incident laser. This relationship was first tested on PdCu@Au tripods using a commercial two-photon confocal microscope (LSM 710 NLO-FLIM, Carl Zeiss, Germany) equipped with a femtosecond Ti:Sapphire laser and a 34-channel photomultiplier tube-based detector module. By choosing the appropriate filter, suspension containing 1 nM PdCu@Au tripods were imaged at 800 nm excitation, with luminescence signal collected from 499 to 735 nm. The gray value of every image was integrated and compared. As shown in Figure 3.2, the photo luminescence signal displayed a linear relationship to the excitation power in the range of 2–6% when plotted in Log scale. The slope of the fitting curve was measured as 1.94 ± 0.21, indicating a two-photon excitation process. When the power was further increased to above 8%, the luminescence intensity began to slowly increase, indicating a loss of integrity of the PdCu@Au tripods as the result of photothermal heating.

3.2.3 The Emission Spectra and Two-Photon Action Cross Sections

I further measured the emission spectra of the two-photon luminescence from PdCu@Au tripods. In this experiment, an aqueous suspension containing 1 nM PdCu@Au tripods was sealed into sample holder, and subjected to two-photon microscopy with 800 nm excitation. By collecting photo luminescence images independently with different channels, luminescence intensity data was calculated from the sets of images with a spectral resolution of 4 nm. As shown in Figure 3.3a, PdCu@Au tripods shows a broad emission peak with a maximum emission at *ca.* 570 nm. I then prepared Au nanorods

suspension with maximum attenuation at 809 nm as benchmark. With the same setting, two-photon luminescence emission spectra of Au nanorods, which have the same attenuation value (5.85 a.u., 2.4 nM) at *ca.* 808 nm were measured. The emission spectrum of Au nanorods shows a maximum emission at *ca.* 500 nm, with a long tail extending to above 700 nm.(Figure 3.3a) This result corresponds well with previous studies that testified the reliability of the experimental setup. By comparing the emission spectra of PdCu@Au tripods and Au nanorods, I find that the maximum luminescence intensity from PdCu@Au tripods (1 nM) is 1.93 ± 0.35 times that from the Au nanorods (2.4 nM) in aqueous environment under 800 nm excitation. This result indicated a 3.6 ± 0.9 times higher two-photon action cross section of PdCu@Au tripods then that from Au nanorods of same LSPR peak position. To quantify the two-photon action cross section of the abovementioned nanoparticles, I also benchmarked the emission spectra to an organic dye, Rhodamine B (Figure 3.3b). Rhodamine B is a widely used organic dye with a two-photon action cross section measured as 153 GM (1 GM = 1×10^{-50} cm^4s/photon) in ethanol under 800 nm excitation. The two-photon action cross section of PdCu@Au tripods and Au nanorods were than measured as $1.83 \pm 0.15 \times 10^5$ GM and $3.97 \pm 0.39 \times 10^4$ GM, respectively. This results also correspond well with the works published by Xu and co-workers.[3] Taken together, PdCu@Au tripods possess a large two-photon action cross section 3.6 times higher than Au nanorods (Figure 3.4), within the range of that of quantum dots (2000-47000 GM).[6, 7]

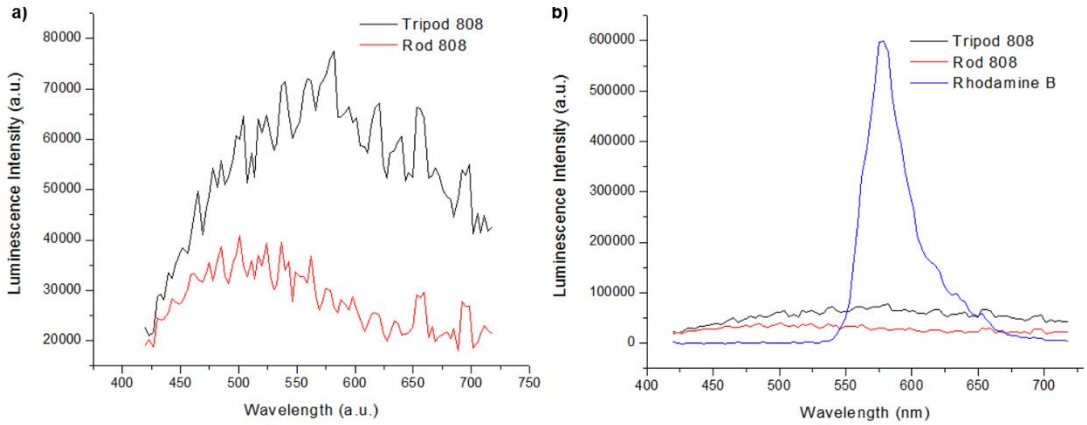

Figure 3.3. a) The two-photon luminescence emission spectra of PdCu@Au tripods and Au nanorods. B) The cooperation of two-photon luminescence excited from 1 nm PdCu@Au tripods, 2.4 nM Au nanorods, and 10 μM Rhodamine B.

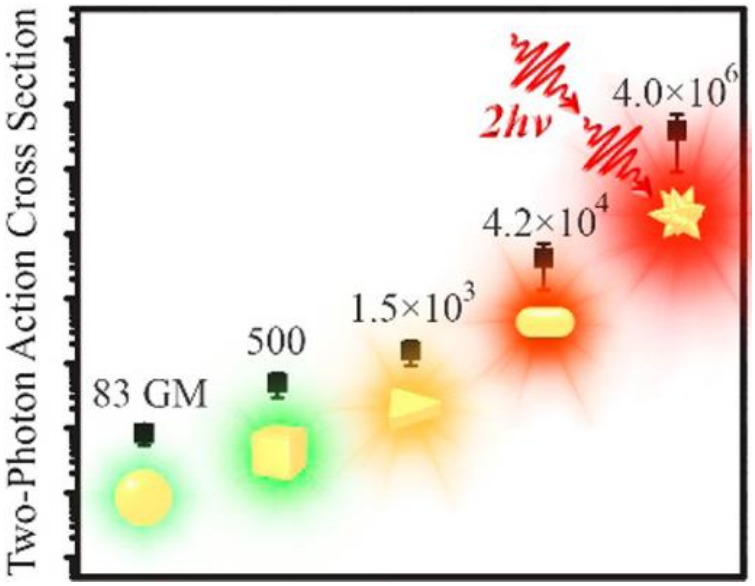

Figure 3.4. The comparison of two-photon action cross sections from different kinds of Au nanoparticles.

3.2.4 Measurement of the Two-Photon Quantum Yield

I further measured the two-photon quantum yield for PdCu@Au tripods and Au nanorods with the indirect method.[8, 9] The photoluminescence emitted from PdCu@Au

tripods and Au nanorods were compared to that from Rhodamine B of similar absorption. The extinction of Tripod 808, Au nanorods, and Rhodamine B were directly read out from their UV-vis extinction spectra. Based on numerical simulation in chapter 2 and previous report, about 91% of the total extinction of Tripod 808 was caused by the absorption at 800 nm, and is comparable to that ratio of Au nanorod.[5, 10] According to previous report, the two-photon quantum yield of Rhodamine B was reported to be 0.7.[11] The two-photon quantum yield of Tripod 808 and Au nanorods was determined as $2.1 \pm 0.2 \times 10^{-6}$ and $1.1 \pm 0.1 \times 10^{-6}$, respectively. This measurement for Au nanorods is slightly lower than that reported by Orrit and co-workers using single Au nanorod ($3.8–8.0 \times 10^{-6}$). It is worth pointing out that significant higher two-photon quantum yield (*ca.* 10^{-4}) were reported for Au nanorods. That could be the result of particle-particle interaction, caused by the aggregation of samples when deposited onto substrate.[12] In contrast, the dispersed particles and isolated deposited particles will not be affected by this enhancement caused by local electromagnetic field enhancement, thus the corresponding measurements of their two-photon quantum yield were lower.

3.2.5 Contrast Enhanced Two-Photon Luminescence Imaging In Vitro

The *in vitro* contrast enhancement capability was also demonstrated with PdCu@Au tripods on MDA-MB-435 breast cancer cells. After incubation with $mPEG_{5000}$-SH or FA-PEG_{5000}-SH coated PdCu@Au tripods for certain period of times, cells were washed out and fixed with 4% PFA solution. A green fluorescent dye, DiO (3,3'-dioctadecyloxacarbocyanine, perchlorate), was also applied to counterstain the cell membrane. As shown in Figure 3.5, the two-photon luminescence only associated with the cells stained with PdCu@Au tripods with low background signal. Comparing to the non-

targeted group, the FA conjugated group exhibit significant higher luminescence signals, indicating an elevated cell uptake of nanoparticles *via* folic acid receptor mediated endocytosis. A time dependent behavior of luminescence intensity was also observed for both groups, as the luminescence signal increases along with the time of incubation.

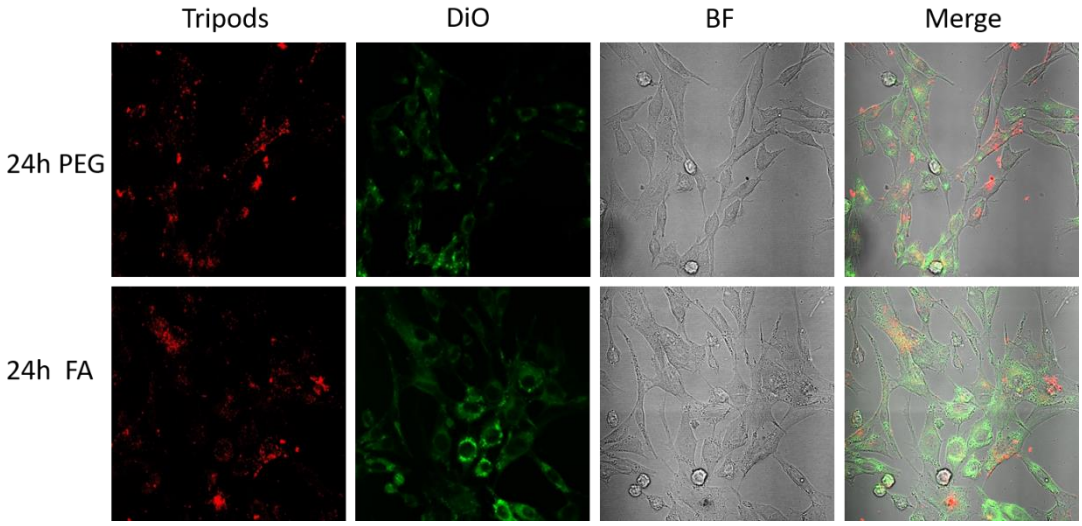

Figure 3.5. *In vitro* contrast enhancement with PdCu@Au tripods.

3.3 Summary

In this chapter, I have demonstrated the outstanding two-photon luminescence property of PdCu@Au tripods and applied it to cancer cell imaging. Based on the quantitative measurement, the PdCu@Au tripods exhibit a 3 order of magnitude higher two-photon action cross section than that from organic dyes (such as Rhodamine B). Comparing to the widely-used Au nanorods, which have been extensively studied for two-photon luminescence microscopy, the PdCu@Au tripods still shows a *ca.* 4.6 times higher two-photon action cross section and comparable two-photon quantum yield ($2.1 \pm 0.2 \times 10^{-6}$) indicating a superior two-photon luminescence property. By *in vitro* cancer cell

targeting experiment, the PdCu@Au tripods were also demonstrated to be delivered to cancer cells for contrast enhancement of two-photon luminescence imaging. In combination with the excellent LSPR property (tunable peak position in NIR region, photothermal generation capability) and PET imaging capability demonstrated in chapter 2, I validated that the PdCu@Au tripods could act as a novel multifunctional platform that holds great potential for cancer theranostics.

3.4 Experimental

3.4.1 Chemicals and Reagents.

Citrate stabilized Au nanorods with maximum extinction at 809 nm (Lot. # DMW0339) were obtained from NanoComposix (San Diego, CA). Folic poly(ethylene glycol)monomethyl ether thiol (FA-PEG_{5000}-SH, MW ≈ 5,000) was purchased from Nanocs Inc. (New York, NY), poly(ethylene glycol)monomethyl ether thiol ($mPEG_{5000}$-SH, MW ≈ 5,000) was obtained from ToYong Bio (Shanghai, China). Cell Counting Kit-8 (CCK-8) was obtained from Solarbio (Beijing, China), and DPBS was obtained from Hyclone (Logan, UT). 3,3'-dioctadecyloxacarbocyanine perchlorate cell staining kit (DiO) was obtained from Beyotime (Shanghai, China). Other chemicals and reagents, including Na_2PdCl_4 (99.998%), KBr, PVP(MW ≈ 55,000), $CuCl_2 \cdot 2H_2O$, AA, DMSO, were obtained from Sigma-Aldrich (St. Louis, MO). All chemicals were used as received.

3.4.2 Synthesis of the PdCu Alloy Tripods.

The PdCu tripods were prepared with a modified method of the synthesis originally reported by our group.[13] In the modified synthesis, 6 mL of aqueous solution containing

6 mg $CuCl_2 \cdot 2H_2O$, 40 mg AA, 70 mg PVP, and 350 mg KBr were preheated in a 20 mL glass vial at 80 °C under magnetic stirring. After 10 min, 38 mg Na_2PdCl_4 was dissolved into 2 mL ultrapure water and introduced into the reaction solution. The reaction was then allowed to carry on under nitrogen protection for 2 h at 80 °C. The reaction was stopped by rapidly cooling down the vial in ice bath, and the product was collected and washed by centrifuge. After three times of washing (8500 g, 30 min) with ultrapure water, the product was re-dispersed into 8 mL of ultrapure water as stock suspension for further use.

3.4.3 Synthesis of the mPEG-PdCu@Au and FA-PEG-PdCu@Au Tripods.

The PdCu@Au tripods were synthesized by directly coating PdCu tripods with Au *via* chemical deposition. In the modified synthesis, aqueous solution of $HAuCl_4$ was dropwisely (2 mL/h) added into the glass vial containing 24 mg PVP, 70 mg AA, 4.0 mL H_2O and 50 μL stock solution of PdCu tripods with the help of syringe pump at room temperature. The extinction spectra of the reaction solution were monitored using UV-vis-NIR spectrometer for the position of main LSPR peaks. The titration was stopped when the main LSPR peaks reached *ca.* 880 and *ca.* 810 nm, which corresponded to a titration volume of 6 and 12 mL, respectively. The products were harvest by centrifuge at 3200 g for 30 min. and washed 3 times with H_2O. The concentration of PdCu@Au tripods was quantified by ICP-AES (Profile Spec, Leeman, USA). The surface of as prepared PdCu@Au tripods was then functionalized by direct incubation with $mPEG_{5000}$-SH or the mixture of FA-PEG_{5000}-SH and $mPEG_{5000}$-SH (molar ratio = 1 : 5). The PdCu@Au tripods were allowed to react in 1 mL solution containing 14 mg of PEG derivatives at room temperature for 24 h, at a molar ratio of *ca.* 1 : 200,000. Excess PEG derivatives were removed with centrifuge.

3.4.4 Characterization of PdCu@Au Tripods.

The measurement of extinction spectra was carried out with a UV-vis spectrometer (UV-2550, Shimadzu, Kyoto, Japan) with wavelengths in the range of 400-900 nm. The size and morphology of PdCu@Au tripods were directly imaged under TEM (Tecnai F30, FEI) operated at 300 kV. Their composition was measured by ICP-AES analysis with Profile Spec (Leeman, USA).

3.4.5 Cell Culture.

The MDA-MB-435 breast cancer cell line was obtained from the American Type Culture Collection (ATCC, Manassas, VA, USA). The cells were cultured in DMEM medium, supplemented with 10% fetal bovine serum and 1% penicillin/streptomycin, at 37 °C in a humidified atmosphere of 5% CO_2.

3.4.6 Cell Proliferation and Cytotoxicity Assay In Vitro.

The MDA-MB-435 cells were seeded in 96-wall plates at a density of 1×10^4 cells/wall, and were allowed to grow for 24 h. Prior to the assay, the cells were washed with 100 μL fresh DPBS. Then, 100 μL culture medium containing mPEG-PdCu@Au tripods or FA-PEG- PdCu@Au tripods with concentration of 6.25 to 800 pM were added to different walls. After 24 h, the culture medium was removed and changed to 100 μL fresh culture medium containing 10 μL of the CCK-8 solution (final concentration of 1 mg/mL). after another hour of incubation, the attenuation at 450 nm was measured for each wall with a microplate reader (Spectramax M2E, Molecular Devices, Sunnyvale, CA). The

results were normalized to the attenuation from the control group to which no nanoparticles were introduced.

3.4.7 The Two-Photon Luminescence of PdCu@Au Tripods.

The two-photon luminescence properties of PdCu@Au tripods were observed and quantified using a commercial two-photon confocal microscope (LSM 710 NLO-FLIM, Carl Zeiss, Germany) equipped with a femtosecond Ti:Sapphire laser (Coherent, Santa Clara, CA). A 34-channel photomultiplier tube-based detector module was also integrated with the microscope for the measurement of emission spectra of the two-photon luminescence. In the typical process, 20 μl aqueous samples containing 1 nM mPEG-PdCu@Au tripods, 2.4 nM Au nanorods, 10 μM Rhodamine 6G, or 10 μM Rhodamine B were sealed onto slides, respectively. An aqueous solution of $mPEG_{5000}$-SH (1 mg/mL) was used as control to get the background signal. The height of the chamber was controlled to 150 μm by sandwiching a cover slip with two others. The laser beam was focused on the suspension by a 10× water-immersion objective. The data was collected as a series of gray-scale images, from which the gray value was summed up as the corresponding luminescence intensity. The two-photon luminescence emission spectra were collected when the 34-channel photomultiplier tube-based detector module was employed. By varying the wavelength and power of the excitation the two-photon luminescence under different excitation conditions was assessed.

3.4.8 Contrast Enhanced Two-Photon Luminescence Imaging In Vitro

To prepare the samples, the MDA-MB-435 cells were first cultured onto glass cover slips in 6-wall plates to a coverage of 60 %. Then the culture medium was changed to fresh

culture medium containing 20 pM of tripods. After certain time of incubation, the culture medium was removed. The slides were extensively washed with DPBS for 3 times to remove the loosely bond particles on the surface of cells and cover slips. The cells were subsequently fixed by incubation with 4% paraformaldehyde for 20 min. The green florescent lipophilic dye of DiO was then employed to stain the cells by incubation with 2 mL fresh DPBS containing 10 μL DiO stock solution (1 mM in DMSO) for 20 min at 37 °C. The cells were washed for 3 times after staining by incubation with fresh DPBS at 37 °C for 30 min. All the samples were sealed onto glass slides before subjecting to two-photon confocal imaging.

3.5 References

[1] Yang, X.; Yang, M.; Pang, B.; Vara, M.; Xia, Y. Gold nanomaterials at work in biomedicine. *Chem. Rev.* **2015**, 115, 10410–10488.

[2] Dreaden, E.C.; Alkilany, A.M.; Huang, X.; Murphy, C.J.; El-Sayed, M.A. The golden age: gold nanoparticles for biomedicine. *Chem. Soc. Rev.* **2012**, 41, 2740–2779.

[3] Gao, N.; Chen, Y.; Li, L.; Guan, Z.; Zhao, T.; Zhou, N.; *et al*. Shape-dependent two-photon photoluminescence of single gold nanoparticles. *J. Phys. Chem. C* **2014**, 118, 13904–13911.

[4] Jiang, X-F.; Pan, Y.; Jiang, C.; Zhao, T.; Yuan, P.; Venkatesan, T.; *et al*. Excitation nature of two-photon photoluminescence of gold nanorods and coupled gold nanoparticles studied by two-pulse emission modulation spectroscopy. *J. Phys. Chem. Lett.* **2013**, 4, 1634–1638.

[5] Pang, B.; Zhao, Y.; Luehmann, H.; Yang, X.; Detering, L.; You, M.; *et al*. ^{64}Cu-doped PdCu@Au tripods: a multifunctional nanomaterial for positron emission tomography and image-guided photothermal cancer treatment. *ACS Nano* **2016**, 10, 3121–3131.

[6] Wang, T.; Halaney, D.; Ho, D.; Feldman, M.D.; Milner, T.E. Two-photon luminescence properties of gold nanorods. *Biomed. Opt. Express* **2013**, 4, 584–595.

[7] Wang, H.; Huff, T.B.; Zweifel, D.A.; He, W.; Low, P.S.; Wei, A.; *et al*. *In vitro* and *in vivo* two-photon luminescence imaging of single gold nanorods. *P. Natl. Acad. Sci. USA* **2005**, 102, 15752–15756.

[8] Chandra Jha, P.; Wang, Y.; Agren, H.; Two-photon absorption cross-sections of reference dyes: a critical examination, *ChemPhysChem* **2008**, 9, 111–116.

[9] Mohamed, M.B.; Volkov, V.; Link, S.; El-Sayed, M.A. The `lightning' gold nanorods: fluorescence enhancement of over a million compared to the gold metal, *Chem. Phys. Lett.* **2000**, 317, 517–523.

[10] Cho, E.C.; Kim, C.; Zhou, F.; Cobley, C.M.; Song, K.H.; Chen, J.; Li, Z-Y.; Wang, L.V.; Xia, Y. Measuring the optical absorption cross-sections of Au-Ag nanocages and Au nanorods by photoacoustic imaging, *J. Phys. Chem. C* **2009**, 113, 9023–9028

[11] Xu, C.; Webb, W.W. Measurement of two-photon excitation cross sections of molecular fluorophores with data from 690 to 1050 nm, *J. Opt. Soc. Am. B* **1996,** 13, 481–491.

[12] Yorulmaz, M.; Khatua, S.; Zijlstra, P.; Gaiduk, A.; Orrit, M. Luminescence quantum yield of single gold nanorods, *Nano Lett.* **2012**, 12, 4385–4391.

[13] Zhang, L.; Choi, S-I.; Tao, J.; Peng, H-C.; Xie, S.; Zhu, Y.; et al. Pd–Cu bimetallic tripods: a mechanistic understanding of the synthesis and their enhanced electrocatalytic activity for formic acid oxidation. *Adv. Funct. Mater.* **2014**, 24, 7520–7529.

CHAPTER 4. AU-199 DOPED AU NANOPARTICLES AS CONTRAST AGENTS FOR TARGETED SPECT IMAGING

The choice of medical isotope in medical imaging will always affect the choice of imaging technology and radiolabeling chemistry. In previous chapters, I have demonstrated the incorporation of Cu-64 into the crystal lattice of PdCu@Au tripods at high efficiency. However, the labeling of Cu-64 in Au nanoparticles can hardly follow the same approach, as the size and morphology of Au nanoparticles would be altered. A possible solution to this issue is to develop new medical isotopes that has similar chemical properties. At the meantime, the different emission energy spectra of certain radionuclides will greatly affect the imaging quality and sensitivity. Thus, the choice of suitable medical isotopes and their radiolabeling chemistry play important roles in nuclear medicine. In this chapter, I demonstrated the use of Au-199 as novel medical isotopes for targeted SPECT imaging of cancer. The Au-199 has the same chemical properties that could be feasibly incorporate into Au nanoparticles without affecting their morphology.

4.1 Introduction

I have demonstrated the use of Au nanoparticle-based nanomedicine for various application such as contrast enhancement of nuclear imaging, optical imaging, and excellent tumor targeting capability, as well as photothermal generation capability. Their application in biomedical imaging has attract great interest as they can serve as platforms to further integrate other functions for cancer theranostics.[1, 2-6] In the context of nuclear medicine, Au nanoparticles have been widely used for contrast agents for PET and SPECT

imaging.[7, 8] Cancer lesion could be detected at a high sensitivity, with only trace amount of contrast agents administrated *in vivo*. As detailed in previous chapter, the radio labeling of Au nanoparticles typically relies on the chelating with a macrocyclic chelating ligand. The unstable labeling through this strategy could greatly affect the imaging-guided treatment of cancer, on the accuracy staging of disease, treatment plan designing, treatment response evaluation, as well as ultimately improvement of patient care. At the mean time. chelator-free approaches such as nuclear bombardment and radiochemical synthesis, have been designed and demonstrated with various kinds of radionuclides.[9-20]

Among the radioisotopes of Au, Au-198 and Au-199 have been found to be medically useful with their attractive nuclear properties.[21] Our group have recently reported the use of Au-198 for both SPECT and Cerenkov luminescence imaging.[12, 22, 23] However, its high-energy γ emission and abundant moderate-energy β^- emission suit better into the therapeutic applications rather than nuclear imaging.[17, 24] In comparison, Au-199 ($t_{1/2}$ = 3.2 d) emits less energetic γ and β^- emission, and can be prepared with high specific activity without carrier by the bombardment of enriched ^{198}Pt with neutrons. A recent study reported the use of low purity Au-199 and Au-198 mixture for the radiolabeling of graphene oxide through a chelating ligand for SPECT imaging.[25] However, both the radiolabeling stability of radionuclides and the image quality of SPECT need further improvement.

Comparing to other imaging modalities, nuclear imaging probes hold high sensitivity and minimal *in vivo* pharmacodynamics effect, which are favorable to the evaluation of progression and metastasis of breast cancer.[26, 27] However, there is still an urgent clinical need for a multivalent nanoparticle-based agent, to detect prognostic

biomarkers of breast cancer with improved specificity and sensitivity.[26, 28, 29] In recent studies, CCR5 has been reported as promising prognostic biomarker, which can be used to track the progression of breast cancer in both preclinical and clinical studies. Triple negative breast cancer, which could hardly be targeted *via* the widely-used biomarkers, could also been targeted with CCR5. Importantly, the expression of CCR5 is also shown to be closely associated with the metastasis of breast cancer, and possesses great potential as a therapeutic target for both primary and metastasis lesion.[30, 31, 32]

In this chapter, I demonstrate the synthesis of Au-199 doped Au nanoparticles and the assessment of their biodistribution profiles as well as contrast enhancement for SPECT imaging in 4T1 tumor bearing mice model. The incorporation of Au-199 into the crystal lattice of Au nanoparticles provide the resulted Au nanoparticle with outstanding radiolabeling stability. The unanimous chemical property of Au-199 and straightforward synthesis ensured a high uniformity in the size of Au nanoparticles and tight control over the specific activity. The *in vivo* targeting capability and favorable pharmacokinetics was also demonstrated with DAPTA conjugated Au nanoparticle for the detection of CCR5 in 4T1 tumor bearing mice model.

4.2 Results and Discussions

The Au nanoparticles used in this study were synthesized with high uniformity in size and shape, through a seed-mediated approach as recently reported by our group for the preparation of single-crystal Au nanospheres.[33] For the radiolabeling of Au-199, I introduced controlled amount of radioactive $H^{199}AuCl_4$ during the growth step of the synthesis, aiming to minimize the radiation exposure.[34] In a typical synthesis, a stock

suspension containing Au clusters was first prepared by rapidly mixing of fresh prepared $NaBH_4$ solution with $HAuCl_4$ solution in the presence of CTAB under vigorous stirring. Before the next step of growth, the resulted mixture was allowed to age for 3 h at room temperature to ensure a complete decomposition of $NaBH_4$. To prepare Au nanoparticle with 5 nm in diameter, the Au clusters were subjected to another round of growth in a solution containing CTAC, AA, and $HAuCl_4$. Upon the addition of Au clusters, the suspension turned rapidly into bright red indication the emerging of LSPR peak around 520-530 nm (Figure 4.1). This feature in LSPR is in good agreement with previous studies.[19] To prepare Au nanoparticles with 18 nm in diameter, 10 nm Au nanoparticles were first prepared by increasing the molar ratio of $HAuCl_4$ to the Au clusters. After substituting the stabilizer from CTAB to CTAC, 10 nm Au nanoparticles could be further grown into 18 nm Au nanoparticles with another round of growth following a similar procedure.

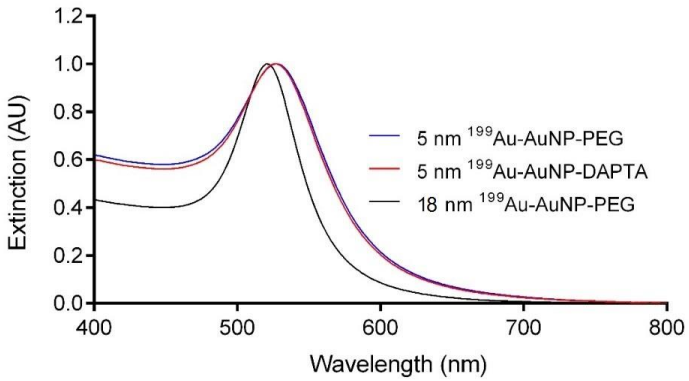

Figure 4.1. The UV-vis spectra of Au nanoparticles (shown as Au NPs) of 5 and 18 nm in diameter, with PEG (shown as AuNP-PEG) or DAPTA-PEG (shown as AuNP-DAPTA) conjugated on their surface.

For the synthesis of Au-199 doped Au nanoparticles, the same protocol where used except for the partial substitution of controlled amount of $H^{199}AuCl_4$ (^{199}Au : ^{197}Au = 1 :

1.65×10^5) during the secondary growth of Au nanoparticles. As shown in Figure 4.2 a,b by the TEM images, the Au-199 doped Au nanoparticles have a well-defined spherical shape together with a narrow size distribution. The Au nanoparticles used in this study were measured to have an average size of 4.7 ± 1.3 nm and 17.6 ± 0.9 nm, respectively. By controlling the amount of $H^{199}AuCl_4$, the specific activity of Au-199 doped nanoparticles could be readily labeled with controlled dose of radioactivity (Figure 4.2c), making it easy to handle in everyday use. At the meantime, the radiolabeling yield could reach to as high as 96.2 ± 0.2% (n = 8) when the $H^{199}AuCl_4$ was introduced to the synthesis directly. The fast protein liquid chromatography (FPLC) measurement, shown in Figure 4.2d, reveal a high chemical and radiochemical purity of about 100%, with a single overlapping peak on the UV and radioactive trace simultaneously. Since Au-199 possesses identical chemical properties to their stable Au-197 counterparts, this radiolabeling approach also provides the nanoparticles with the necessary chemical stability requirement for *in vivo* biomedical applications, as we previously demonstrated with Au-198 doped nanoparticles.[22]

Before the pharmacokinetic evaluation on 4T1 tumor bearing mice model, Au-199 doped Au nanoparticles were first PEGylated with poly(ethylene glycol) methyl ether thiol (HS-PEG_{5000}-OMe, MW ≈ 5000) according to our previously reported procedures.[18, 19] As shown by the pharmacokinetic data Figure 4.3, the Au-199 doped Au nanoparticles of different sizes both showed comparable biodistribution profiles at all the time points. Specifically, their blood retentions measured at 1 h post injection were 45.2 ± 5.8%ID/g and 48.0 ± 5.5%ID/g, respectively (sum of the signals from blood, lung, and heart). At 4 h post injection, the blood pool clearance of 5 nm Au nanoparticles was *ca.* 35% lower than that of the 18 nm counterpart, partially owning to their smaller size. Along with the slightly

lower liver accumulation, their spleen uptake was observed to be 78% higher. This result was in agreement with previous publications.[7, 19] After 4 h, the blood retention of Au nanoparticles began to drop, and the tumor uptake increased consequently. The tumor to muscle ratio for the 5 nm Au nanoparticles was observed to be 10.1 ± 2.3 (n = 4), similar to that of the 18 nm counterparts. This observation was also is consistent with previous publication.[19]

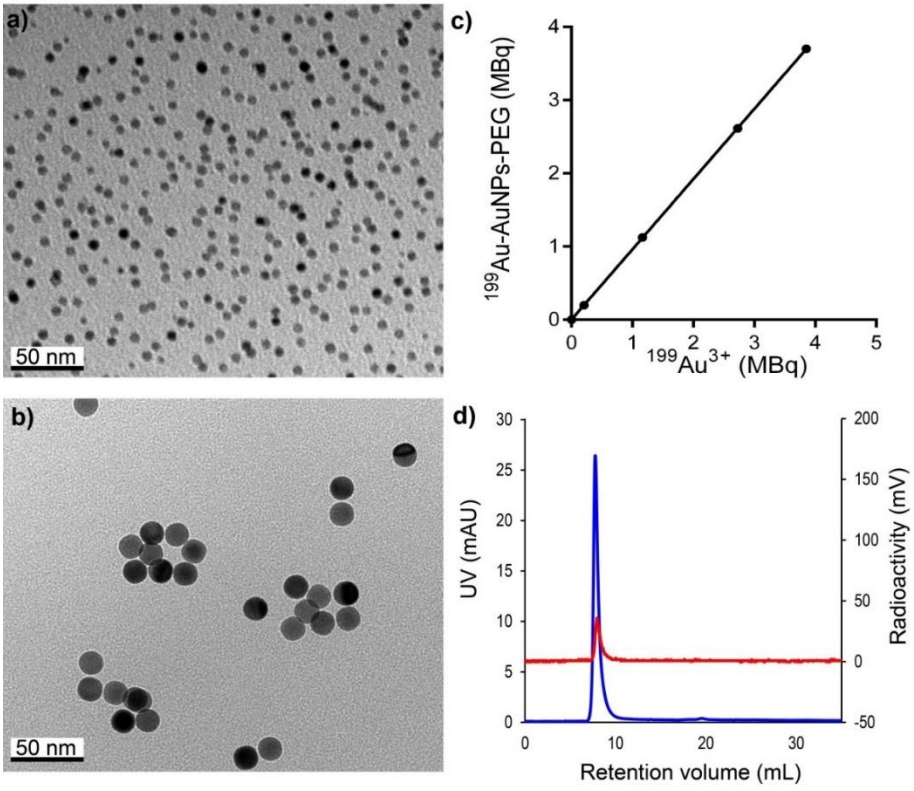

Figure 4.2. (a, b) The TEM micrographs showing the morphology of Au-199 doped Au nanoparticles of (a) 5 nm and (b) 18 nm in diameter, respectively, after 90 days of decay. (c) Plot of radioactivity in the $H^{199}AuCl_4$ precursor the resultant 5-nm ^{199}Au-doped Au nanoparticles. (d) The Radio-FPLC assay showing the high chemical and radiochemical purity of the 5-nm PEGylated ^{199}Au-doped Au nanoparticles. Blue: UV trace; red: radioactivity traces.

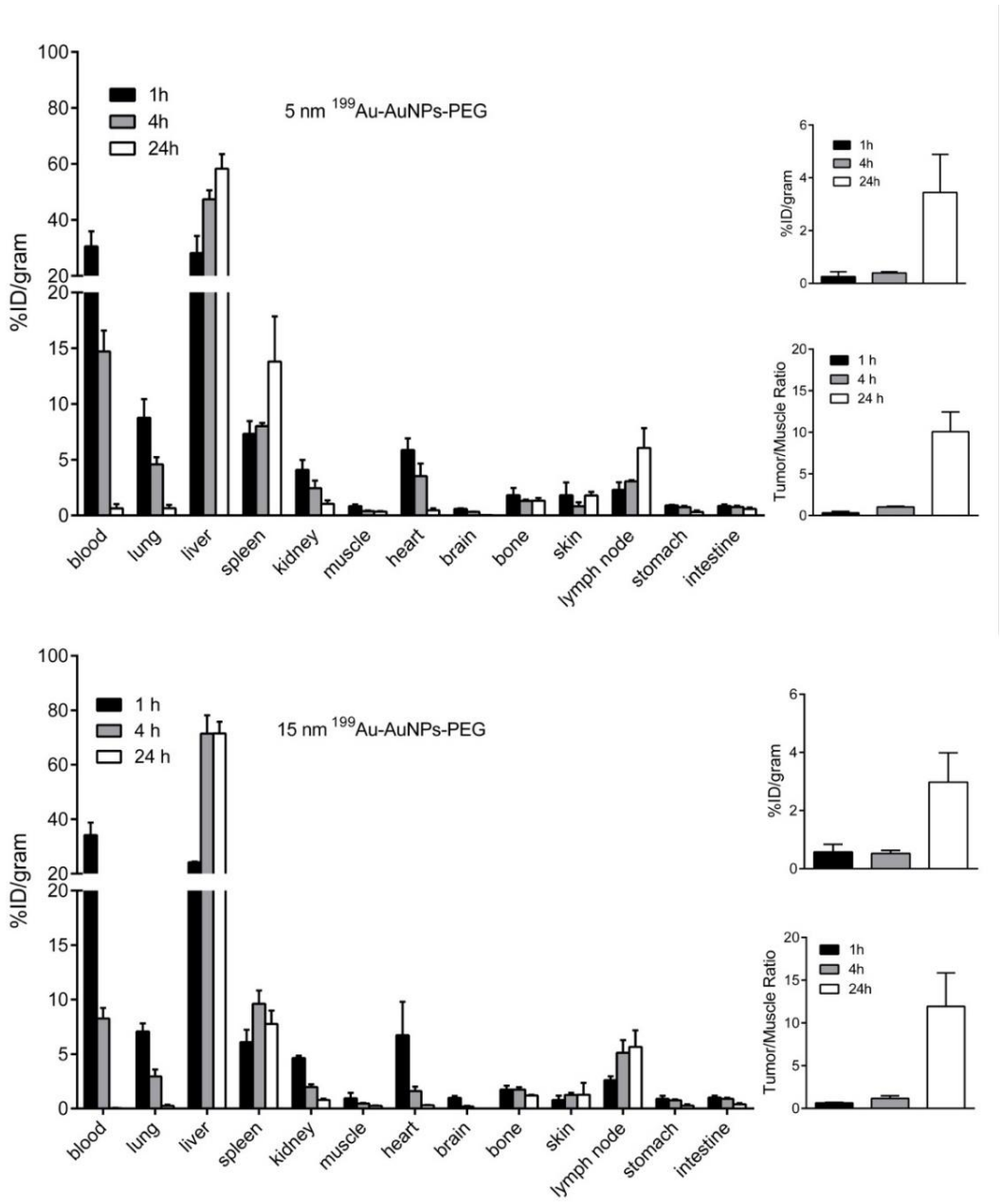

Figure 4.3. Biodistribution profiles of the Au-199 doped Au nanoparticles (left panels) and their tumor accumulation (right panels) in 4T1 tumor-bearing mice model at 1, 4, and 24 h post injection (n = 4 per group). The Au nanoparticles were conjugated with PEG chains, with 5 nm and 18 nm cores.

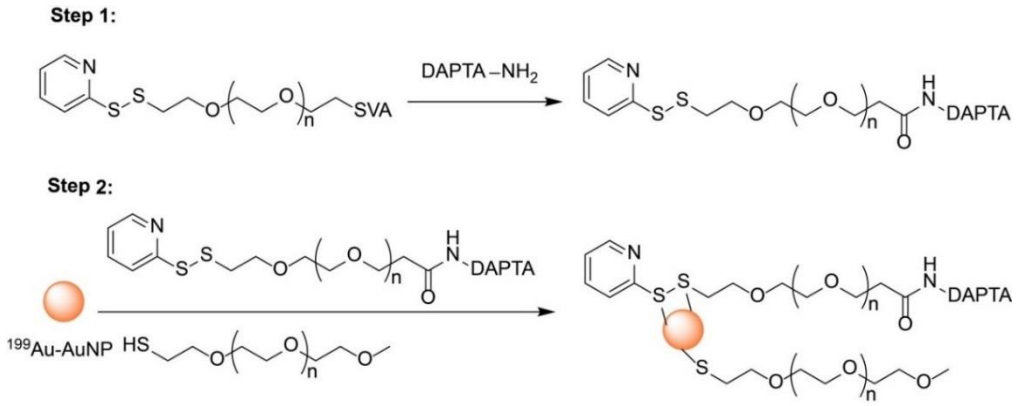

Figure 4.4. A schematic illustration of the synthesis and conjugation of DAPTA-conjugated Au nanoparticles (shown as ^{199}Au-AuNP-DAPTA).

Following the biodistribution study, I further assess the *in vivo* tumor targeting capability of DAPTA peptide-conjugated Au nanoparticle, following the approach previously reported by our group.[36] For the conjugation of DAPTA peptides, I first conjugated DAPTA to OPSS-PEG$_{5000}$-SVA (see Figure 4.4). The resultant PEG derivatives were mixed with HS-PEG$_{5000}$-OMe at a molar ratio of 1:3 and incubated with the Au-199 doped 5 nm Au nanoparticles. As shown in Figure 4.5, the biodistribution profile was substantially improved for DAPTA-conjugated Au nanoparticles, with elevated blood retention (4.77 ± 0.65%ID/g) that was two times higher than that from the PEGylated non-targeted counterparts, at 24 h post injection. The liver uptake was also observed to be *ca.* 60 % less than that of the non-targeted nanoparticles while the accumulation in spleen remained similar. It is suggested that the improvement of their blood retention and, further, the biodistribution profile could be the result of reducing liver accumulation of DAPTA-conjugated Au nanoparticles. This result was also testified by our recent research using polymeric nanoparticles, where the DAPTA conjugation altered the surface charge of nanoparticles and reduced the liver uptake.[36] It is worth noting that the tumor uptake of

DAPTA-conjugated Au nanoparticles was found to be more than doubled (7.13 ± 0.08%ID/g, n = 4), while the tumor to muscle ratio dramatically increased to 18.7 ± 1.69 (n = 4) clearly demonstrating the effectiveness of the targeting technique using CCR5 as cancer biomarker and DAPTA peptide as ligand. Taking together, the tumor uptake of PEGylated Au nanoparticles of 3.45 ± 1.44 %ID/g at 24 h post injection, the active targeting by DAPTA to CCR5 should be account for the most contribution than the passive targeting *via* the EPR effect. In that case, it is still of greater potential to further improve the targeting efficiency by optimizing the surface density of conjugated DAPTA peptide.

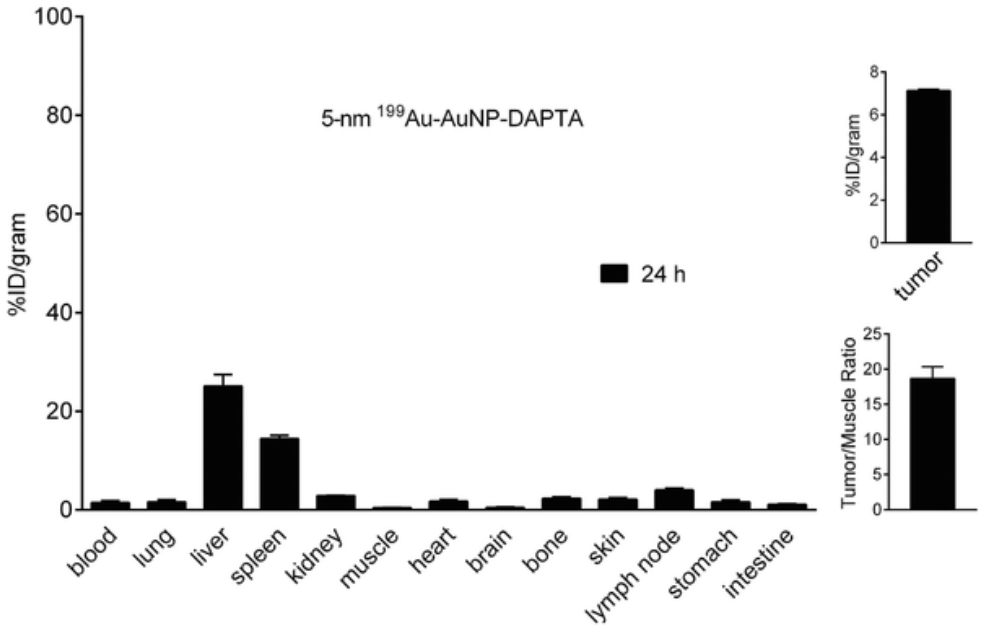

Figure 4.5. The biodistribution and tumor targeting selectivity of DAPTA peptide-conjugated Au nanoparticles in 4T1 tumor bearing mice model. Left: Biodistribution profile of the 5 nm DAPTA-conjugated Au nanoparticles (shown as ^{199}Au-AuNP-DAPTA) at 24 h post injection (n = 4). Right: Quantification of tumor uptake and tumor to muscle ratio of ^{199}Au-AuNP-DAPTA, showing the improved efficiency and selectivity for tumor targeting.

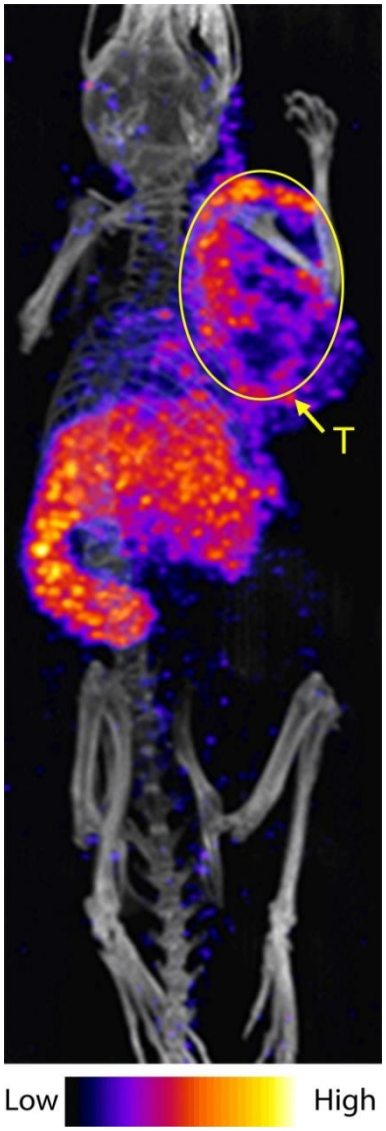

Figure 4.6. SPECT/CT image of a 4T1 tumor-bearing mouse injected with 5 nm DAPTA-conjugated Au nanoparticles showing the tumor targeting at 24 h post injection (T: tumor).

With 5 nm DAPTA-conjugated Au-199 doped Au nanoparticles, I further assessed the SPECT contrast enhancement capability of Au-199, with a targeted SPECT/CT imaging experiment on 4T1 triple negative breast cancer model. As shown in Figure 4.6, the DAPTA-conjugated Au nanoparticles demonstrated a high accumulation in tumor with a heterogeneous pattern of penetration. Significant accumulation in liver and spleen was

also observed in agreement with the biodistribution profile obtained beforehand. In addition, compared to the unsatisfied SPECT image acquired with a mixture of Au-198 and Au-199 on graphene oxide, the imaging quality was greatly improved with Au-199 doped Au nanoparticles as a result of elimination of high energy emission from Au-198.[25] Our work clear reveals the suitability of Au-199 as medical isotope for SPECT imaging, as well as the great potential using DAPTA-conjugated Au nanoparticles for accurate detection of CCR5 in triple negative breast cancer.

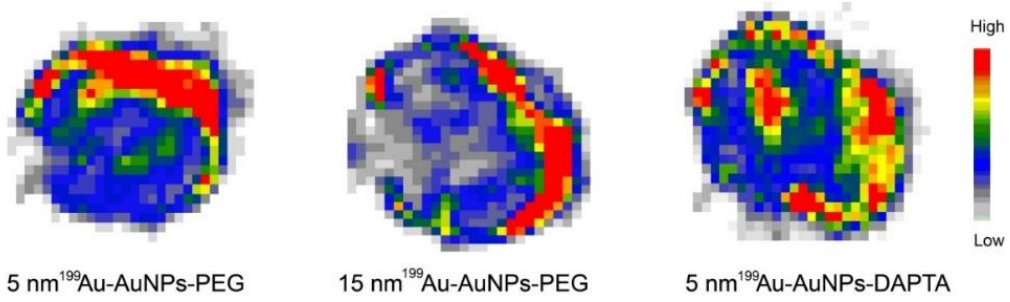

Figure 4.7. Autoradiography images showing the heterogeneous intratumoral distributions of three different types of Au-199 doped Au nanoparticles in the 4T1 tumors at 24 h post injection.

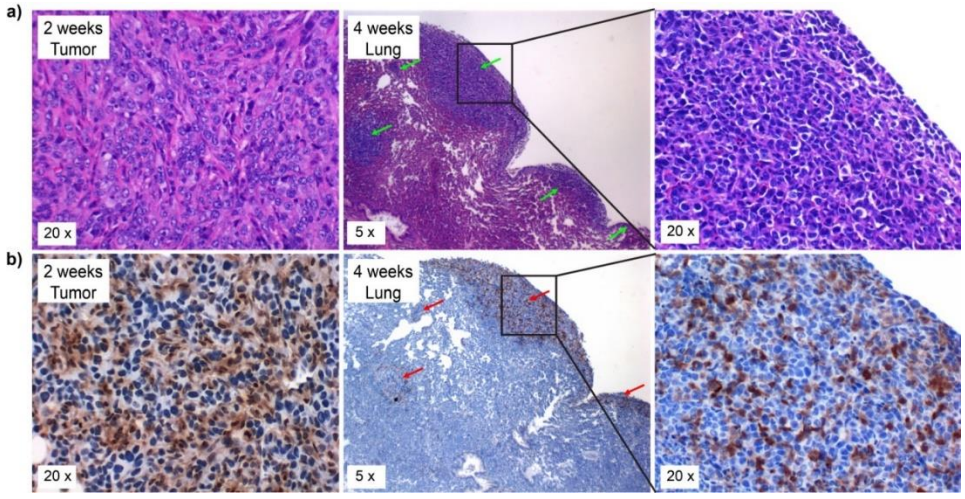

Figure 4.8. (a) H&E and (b) immunohistochemistry of the 4T1 mouse tumor and its lung metastasis, showing the high-level expression of CCR5 in both the primary tumor site and lung metastasis (Green: metastasis; Red: CCR5; Brown staining).

The intratumoral distributions of the different kinds of Au nanoparticles were also evaluated *via* autoradiography. Tumor tissues were extracted and sectioned into slices of 40 μm thick. As shown by the autoradiography in Figure 4.7, all three kinds of Au nanoparticles demonstrated heterogeneous distributions, while the 5 nm ^{199}Au-doped DAPTA-conjugated Au nanoparticles accumulated more homogeneously inside the tumor that is in agreement with the SPECT imaging results.

A significant connection between the up-regulation of CCR5/CCL5 and the progression of tumor has recently been reported by many groups, indicating a direct promotion effect in the progression of breast cancer.[31, 32] As shown by the immunohistochemistry staining data (Figure 4.8), an elevated expression of CCR5 was observed on both the cell membrane and the nuclei after 2 weeks of implantation. At 4 weeks post implant, noticeable metastasis lesion was found in lung. The up regulation of CCR5 was only observed at the metastasis lesion instead of the healthy lung tissue, indicating a direct association of CCR5 with cancer metastasis. This observation is in consistent with previous findings,[30, 36] in which CCR5-positive tumor cells were found to display increased invasiveness for metastasis. These biological studies confirmed that the specific role of CCR5 as progressive biomarker for primary cancer and metastasis lesion, indicating a great potential for CCR5 targeted diagnosis and therapy.

4.3 Summary

In this chapter, I demonstrated the synthesis and surface modification of DAPTA-conjugated Au-199 doped Au nanoparticles as well as their use for CCR-5 targeted tumor imaging with SPECT. The feasibility of using Au-199 as medical isotope for SPECT

imaging was also validated. The novel radiolabeling strategy of incorporating Au-199 into the crystal lattice of nanoparticles provides an extraordinary labeling stability with easily controlled radioactive dosage. This extraordinary labeling stability and moderate energy level of Au-199 enabled a high-quality SPECT imaging with low background for accurate quantification of the cancer biomarkers *in vivo*. The novel approach using DAPTA peptides for CCR5 targeting dramatically improved the biodistribution profile of Au-199 conjugated nanoparticles, enhanced their sensitivity and specificity in tumor targeted SPECT imaging. Our current work of using Au-199 doped nanoparticles for targeted SPECT imaging only served as a proof-of-concept demonstration for the merit of Au-199 as novel medical isotope in nuclear imaging. The long half-life of Au-199 also provides the imaging probes with the capability for a prolonged study duration. Despite the current focus of using DAPTA-conjugated Au-199 doped Au nanoparticles for the diagnosis of primary cancer with SPECT, future study could help to fully reveal the potential of CCR5 as the biomarker for sensitive detection of metastasis lesion.

4.4 Experimental

4.4.1 Chemicals

$HAuCl_4 \cdot 3H_2O$ (≥99.9 %), AA, $NaBH_4$, CTAB, and CTAC, ≥98.0 % were obtained from Sigma-Aldrich (St. Louis, MO). Ultrapure water was prepared using an E-Pure filtration system (Barnstead International, Dubuque, IA) with a resistivity of 18.2 MΩ/cm. The $mPEG_{5000}$-SH (MW ≈ 5000) was obtained from Nanocs (Boston, MA) and OPSS-PEG_{5000}-SVA (MW ≈ 5000) was obtained from Laysan Bio (Arab, AL). DAPTA was acquired as customized product from CPC scientific (Sunnyvale, CA). The $H^{199}AuCl_4$

aqueous solution was obtained from the Missouri University Research Reactor (Columbia, MO). All chemicals were used as received.

4.4.2 Preparation of Au Nanoparticles

The Au nanoparticles were prepared with a seed-mediated growth approach. In a typical synthesis, a suspension containing Au cluster was first prepared by rapidly adding 300 μL ice-cold $NaBH_4$ into the aqueous solution containing 2.5 mL of aqueous CTAB (200 mM) and 2.5 mL of aqueous $HAuCl_4$ (0.5 mM). After 3 h of aging to completely decompose $NaBH_4$. The Au clusters were subjected to further growth.

For the growth of Au nanoparticles of 5 and 10 nm, 1000 μL and 100 μL of the aqueous suspension containing Au clusters was added to a solution containing 2 mL of CTAC (200 mM), 2 mL $HAuCl_4$ (0.5 mM), and 1.5 mL AA (100 mM), respectively. The mixture was gently shaken for 2 min and allowed to react for 1 h. The as prepared Au nanoparticles were collected by ultrafiltration (Molecular weight cut-off (MWCO) ≈ 100 K, Amicon, 10,000 g, 5 min), and washed with 4 mL of ultrapure water before further use.

For the preparation of 18 nm Au nanoparticles, 10 nm Au nanoparticles were used as seeds. In a typical synthesis, 160 μL aqueous suspension containing 10 nm Au nanoparticles was mixed with 1 mL CTAC (200 mM), 1 mL H_2O, and 130 μL of AA (10 mM). After gentle mixing, 2 mL $HAuCl_4$ (0.5 mM) was dropwisely (at a rate of 2 mL/h) added into the mixture with the help of syringe pump under magnetic stirring. The as prepared Au nanoparticles were collected by centrifuge (13,200 rpm, 10 min), and washed three times with of ultrapure water before further use.

4.4.3 Preparation of Au Nanoparticles Doped with Au-199 Atoms

Using a similar protocol, The Au-199 doped Au nanoparticles were prepared by partially substituting the non-radioactive $H^{197}AuCl_4$ with radioactive $H^{199}AuCl_4$.

For the growth of ^{199}Au-Au nanoparticles of 5 nm, 1000 μL of the aqueous suspension containing Au clusters was added to a solution containing 2 mL of CTAC (200 mM), 2 mL $HAuCl_4$ (0.5 mM), 1.5 mL AA (100 mM), and 69.9 MBq of $H^{199}AuCl_4$. The mixture was gently shaken for 2 min and allowed to react for 1 h. The as prepared ^{199}Au-Au nanoparticles were collected by ultrafiltration MWCO ≈ 100 K, Amicon, 10,000 g, 5 min), and washed with 4 mL of ultrapure water before further use.

For the preparation of 18 nm Au nanoparticles, 10 nm Au nanoparticles were used as seeds. In a typical synthesis, 320 μL aqueous suspension containing 10 nm Au nanoparticles was mixed with 2 mL CTAC (200 mM), 2 mL H_2O, and 260 μL of AA (10 mM). After gentle mixing, 4 mL $HAuCl_4$ (0.5 mM) containing 81.6 MBq of $H^{199}AuCl_4$ was dropwisely (at a rate of 2 mL/h) added into the mixture with the help of syringe pump under magnetic stirring. The as prepared ^{199}Au-Au nanoparticles were collected by centrifuge (13,200 rpm, 10 min), and washed three times with of ultrapure water before further use.

All the experiments involving the use of radioactive species were conducted under appropriate protection according to the guidance from the Radiation Safety Office of Washington University in St. Louis.

4.4.4 PEGylation of Au Nanoparticles

Before the surface modification, the OPSS-PEG_{5000}-DAPTA molecules were first synthesized by conjugating the DAPTA onto PEG NHS ester derivative of OPSS-PEG_{5000}-SVA with their primary amine group. In a typical synthesis, the OPSS-PEG_{5000}-SVA was mixed with DAPTA peptides in DPBS at a molar ratio of 1:5 to react overnight at 4 ºC. The resulted mixture was used without further purification. The PEGylation was subsequentially conducted by incubating Au nanoparticles with a solution of a mixture of OPSS-PEG_{5000}-DAPTA and HS-PEG_{5000}-OMe (molar ratio = 1:3) or HS-PEG_{5000}-Ome at a molar ratio of 1:100,000 (nanoparticle : PEG) for the DAPTA-conjugated Au nanoparticles and PEG coated Au nanoparticles, respectively. The conjugation was allowed to react at room temperature overnight on the shaker. Excess PEG species were removed by ultrafiltration (MWCO ≈ 100 K, Amicon, 10,000g, 5 min), and washed for 3 times with 4 mL of ultrapure water. The purified nanoparticles were dispersed in saline (APP Pharmaceuticals, Schaumburg, IL) for animal study.

The PEGylation of 18 nm Au nanoparticles was conducted by following a similar procedure described above, besides the centrifugation (13,200 rpm, 10 min) was used for purification instead of ultrafiltration.

4.4.5 Characterization of Au Nanoparticles

The TEM imaging was conducted with a Hitachi HT7700 microscope operating at 120 kV to determine the size and morphology of Au nanoparticles. Radioactive samples were imaged after 90 days of decay. The UV-vis spectra were acquired using a Lambda 750 spectrometer (Perkin-Elmer, Wellesley, MA).

4.4.6 In Vivo Biodistribution Studies

Female BALB/c mice weighing 15−20 g were used to prepare the 4T1 tumor model. For each seven-week-old mouse, 5×10^6 cancerous cells were subcutaneously injected in 100 μL saline under the right front leg. The tumors were allowed to grow to a size of 200 and 300 mm^3 in 8-10 d before the animal studies. In the biodistribution study, each mouse was injected with 100 μL saline containing 111−185 KBq of ^{199}Au-Au nanoparticles *via* the tail vein. At series time points (1, 4, and 24 h post injection), the mice were sacrificed by cervical dislocation under anesthesia. Organs of interest were than collected, weighed, and subjected to γ counting using a Beckman 8000 gamma counter (Beckman, Fullerton, CA). The weight-normalized dosage was calculated as percentage of the %ID/g for each kinds of organ.

All the protocols for animal studies were approved by the Washington University Animal Studies Committee.

4.4.7 SPECT/CT Imaging

At 24 h prior to the imaging, each of the he 4T1 tumor bearing mice were anesthetized with isoflurane and injected with 100 μL of saline containing 29.6 MBq of ^{199}Au-doped DAPTA-conjugated Au nanoparticles *via* the tail vein. At 24 h post injection, SPECT/CT scans were performed using NanoSPECT/CT (Bioscan, Washington, DC) The images for CT and SPECT were reconstructed by InvivoScope software (Bioscan, Inc., Washington, DC) With voxel size of 0.4 and 0.6 mm, respectively.

4.4.8 Autoradiography Studies

After NanoSPECT/CT scan, the tumors were dislocated and frozen in optimal cutting temperature compound and sectioned into slices of 50 μm in thickness. The tumor slices were sealed to glass slides before subjecting to 2D autoradiography (InstantImager Electronic Autoradiography, Packard, Meriden, CT).

4.4.9 Immunohistochemistry and Histology Quantification

For the histochemistry assays, paraformaldehyde-fixed (24 h) and paraffin-embedded samples were sliced into a series sections of 5 μm thick. Before the antibody staining, a series of xylenes and graded alcohols treatments were conducted for the deparaffinization and rehydration of specimens. Antigen retrieval pretreatment (10 mM Tris, 1 mM ethylenediaminetetraacetic acid, 0.05% Tween, and at pH = 9.0 for 10 min) was then conducted. To prevent nonspecific binding all the slides were treated with 0.3% H_2O_2 for 30 min, and blocking serum for 1 h (Vectastain, Vector Laboratories, Burlingame, CA). Antibody staining was then carried out by incubating a primary antibody (anti-CCR5, 1:100 in blocking serum, Santa Cruz Biotechnology, Dallas, TX) at 4 °C overnight. After the staining of secondary antibody (Vector Laboratories) a horse radish peroxidase-based immunostaining kit (Vector Laboratories) was employed to develop a brown color. Counterstaining of nuclei was accomplished with hematoxylin for a blue color. Images were acquired with a light microscope (Leica Microsystems). Routine H&E staining was also performed on the slides to analyze the morphology of the tissue.

4.4.10 Statistical Analysis

Prism software (version 6.04, GraphPad) was used for all statistical analyses. One-way analyses of variance were conducted with a Bonferroni post-test between groups. Two- tailed student t-tests were conducted to determine the difference for individual group with a significance level of $p \leq 0.05$.

4.5 References

[1] Wang, Y.; Black, K.C.L.; Luehmann, H.; Li, W.; Zhang, Y.; Cai, X.; *et al*. Comparison study of gold nanohexapods, nanorods, and nanocages for photothermal cancer treatment. *ACS Nano* **2013**, 7, 2068–2077.

[2] Cobley, C.M.; Chen, J.; Cho, E.C.; Wang, L.V.; Xia, Y. Gold nanostructures: a class of multifunctional materials for biomedical applications. *Chem. Soc. Rev.* **2011**, 40, 44–56.

[3] Kumar, D.; Saini, N.; Jain, N.; Sareen, R.; Pandit, V. Gold nanoparticles: an era in bionanotechnology. *Expert Opin. Drug Del.* **2013**, 10, 397–409.

[4] Meir, R.; Motiei, M.; Popovtzer, R. Gold nanoparticles for *in vivo* cell tracking. *Nanomedicine (Lond.)* **2014**, 9, 2059–2069.

[5] Webb, J.A.; Bardhan, R. Emerging advances in nanomedicine with engineered gold nanostructures. *Nanoscale* **2014**, 6, 2502–2530.

[6] Trouiller, A.J.; Hebie, S.; El Bahhaj, F.; Napporn, T.W.; Bertrand, P. Chemistry for oncotheranostic gold nanoparticles. *Eur. J. Med. Chem.* **2015**, 99, 92–112.

[7] Liu, Y.; Welch, M.J. Nanoparticles labeled with positron emitting nuclides: advantages, methods, and applications. *Bioconj. Chem.* **2012**, 23, 671–682.

[8] Guo, Y.; Aweda, T.; Black, K.C.L.; Liu, Y.; Chemistry and theranostic applications of radiolabeled nanoparticles for cardiovascular, oncological, and pulmonary research. *Curr. Top. Med. Chem.* **2013**, 13, 470–478.

[9] Gibson, N.; Holzwarth, U.; Abbas, K.; Simonelli, F.; Kozempel, J.; Cydzik, I.; *et al*. Radiolabelling of engineered nanoparticles for *in vitro* and *in vivo* tracing applications using cyclotron accelerators. *Arch. Toxicol.* **2011**, 85, 751–773.

[10] Sun, X.; Cai, W.; Chen, X. Positron emission tomography imaging using radiolabeled inorganic nanomaterials. Acc. Chem. Res. 2015, 48, 286–294.

[11] Lipka, J.; Semmler-Behnke, M.; Sperling, R.A.; Wenk, A.; Takenaka, S.; Schleh, C.; *et al*. Biodistribution of PEG-modified gold nanoparticles following intratracheal instillation and intravenous injection. *Biomaterials* **2010**, 31, 6574–6581.

[12] Yang, S.; Sun, S.; Zhou, C.; Hao, G.; Liu, J.; Ramezani, S.; *et al*. Renal clearance and degradation of glutathione-coated copper nanoparticles. *Bioconj. Chem.* **2015**, 26, 511–519.

[13] Gao, F.; Cai, P.; Yang, W.; Xue, J.; Gao, L.; Liu, R.; *et al*. Ultrasmall [(64)Cu]Cu nanoclusters for targeting orthotopic lung tumors using accurate positron emission tomography imaging. *ACS Nano* **2015**, 9, 4976–4986.

[14] Goel, S.; Chen, F.; Ehlerding, E.B.; Cai, W. Intrinsically radiolabeled nanoparticles: an emerging paradigm. *Small* **2014**, 10, 3825–3830.

[15] Sun, X.; Huang, X.; Yan, X.; Wang, Y.; Guo, J.; Jacobson, O.; *et al*. Chelator-free (64)Cu-integrated gold nanomaterials for positron emission tomography imaging guided photothermal cancer therapy. *ACS Nano* **2014**, 8, 8438–8446.

[16] Shaffer, T.M.; Wall, M.A.; Harmsen, S.; Longo, V.A.; Drain, C.M.; Kircher, M.F.; *et al*. Silica nanoparticles as substrates for chelator-free labeling of oxophilic radioisotopes. *Nano Lett.* **2015**, 15, 864–868.

[17] Chanda, N.; Kan, P.; Watkinson, L.D.; Shukla, R.; Zambre, A.; Carmack, T.L.; *et al*. Radioactive gold nanoparticles in cancer therapy: therapeutic efficacy studies of GA-^{198}AuNP nanoconstruct in prostate tumor-bearing mice. *Nanomedicine (Lond.)* **2010**, 6, 201–209.

[18] Wang, Y.; Liu, Y.; Luehmann, H.; Xia, X.; Brown, P.; Jarreau, C.; *et al*. Evaluating the pharmacokinetics and *in vivo* cancer targeting capability of Au nanocages by positron emission tomography imaging. *ACS Nano* **2012**, 6, 5880–5888.

[19] Zhao, Y.; Sultan, D.; Detering, L.; Cho, S.; Sun, G.; Pierce, R.; *et al*. Copper-64-alloyed gold nanoparticles for cancer imaging: improved radiolabel stability and diagnostic accuracy. *Angew. Chem. Int. Ed.* **2014**, 53, 156–159.

[20] Zhao, Y.; Sultan, D.; Detering, L.; Luehmann, H.; Liu, Y. Facile synthesis, pharmacokinetic and systemic clearance evaluation, and positron emission tomography cancer imaging of ^{64}Cu-Au alloy nanoclusters. *Nanoscale* **2014**, 6, 13501–13509.

[21] Cutler, C.S.; Hennkens, H.M.; Sisay, N.; Huclier-Markai, S.; Jurisson, S.S. Radiometals for combined imaging and therapy. *Chem Rev.* **2013**, 113, 858–883.

[22] Black, K.C.L.; Wang, Y.; Luehmann, H.; Cai, X.; Xing, W.; Pang, B.; *et al*. Radioactive ^{198}Au-doped nanostructures with different shapes for *in vivo* analyses of their biodistribution, tumor uptake, and intratumoral distribution. *ACS Nano* **2014**, 8, 4385–4394.

[23] Wang, Y.; Liu, Y.; Luehmann, H.; Xia, X.; Wan, D.; Cutler, C.; *et al*. Radioluminescent gold nanocages with controlled radioactivity for real-time *in vivo* imaging. *Nano Lett.* **2013**, 13, 581–585.

[24] Chaudhry, I.A.; Liu, M.; Shamsi, F.A.; Arat, Y.O.; Shetlar, D.J.; Boniuk, M. Corneoscleral necrosis after episcleral Au-198 brachytherapy of uveal melanoma. *Retina* **2009**, 29, 73–79.

[25] Fazaeli, Y.; Akhavan, O.; Rahighi, R.; Aboudzadeh, M.R.; Karimi, E.; Afarideh, H. *In vivo* SPECT imaging of tumors by ^{198,199}Au-labeled graphene oxide nanostructures. *Mat. Sci. Eng. C* **2014**, 45, 196–204.

[26] Nienhuis, H.H.; Gaykema, S.B.; Timmer-Bosscha, H.; Jalving, M.; Brouwers, A.H.; Lub-de Hooge, M.N.; *et al*. Targeting breast cancer through its microenvironment: current status of preclinical and clinical research in finding relevant targets. *Pharmacol. Therapeut.* **2015**, 147, 63–79.

[27] Alcantara, D.; Leal, M.P.; Garcia-Bocanegra, I.; Garcia-Martin, M.L. Molecular imaging of breast cancer: present and future directions. *Front. Chem.* **2014**, 2, 112.

[28] Bardhan, R.; Lal, S.; Joshi, A.; Halas, N.J. Theranostic nanoshells: from probe design to imaging and treatment of cancer. *Acc. Chem. Res.* **2011**, 44, 936–946.

[29] van Uden, D.J.; van Laarhoven, H.W.; Westenberg, A.H.; de Wilt, J.H.; Blanken-Peeters, C.F. Inflammatory breast cancer: an overview. *Crit. Rev. Oncol./Hemat.* **2015**, 93, 116–126.

[30] Velasco-Velazquez, M.; Jiao, X.; De La Fuente, M.; Pestell, T.G.; Ertel, A.; Lisanti, M.P.; *et al*. CCR5 antagonist blocks metastasis of basal breast cancer cells. *Cancer Res.* **2012**, 72, 3839–3850.

[31] Fertig, E.J.; Lee, E.; Pandey, N.B.; Popel, A.S. Analysis of gene expression of secreted factors associated with breast cancer metastases in breast cancer subtypes. *Sci. Rep.* **2015**, 5, 12133.

[32] Norton, K.A.; Popel, A.S.; Pandey, N.B. Heterogeneity of chemokine cell-surface receptor expression in triple-negative breast cancer. *Am. J. Cancer Res.* **2015,** 5, 1295–1307.

[33] Zheng, Y.; Zhong, X.; Li, Z.; Xia, Y. Successive, Seed-mediated growth for the synthesis of single-crystal gold nanospheres with uniform diameters controlled in the range of 5–150 nm. *Part. Part. Syst. Char.* **2014**, 31, 266–273.

[34] Zhao, Y.; Pang, B.; Luehmann, H.; Detering, L.; Yang, X.; Sultan, D.; Harpstrite, S.; Sharma, V.; Cutler, C.S.; Xia, Y.; Liu, Y. Gold nanoparticles doped with ^{199}Au atoms and their use for targeted cancer imaging by SPECT. *Adv. Healthc. Mater.* **2016**, 5, 928–935.

[35] Luehmann, H.P.; Pressly, E.D.; Detering, L.; Wang, C.; Pierce, R.; Woodard, P.K.; *et al*. PET/CT imaging of chemokine receptor CCR5 in vascular injury model using targeted nanoparticle. Journal of nuclear medicine : official publication, *Soc. Nucl. Med.* **2014**, 55, 629–634.

[36] Velasco-Velazquez, M.; Pestell, R.G. The CCL5/CCR5 axis promotes metastasis in basal breast cancer. *Oncoimmunology* **2013**, 2, e23660.

CHAPTER 5. ARG-GLY-ASP CONJUGATED AU NANORODS FOR RADIO THERAPY

In previous chapters, I described the fabrication of Au nanoparticle-based nanomedicine and their radiolabeling as well as surface modification. With the innovative radiolabeling of novel medical isotopes, I also demonstrated the targeted imaging of cancer and imaging guided photothermal therapy. In this chapter, I would further present our study on the nanoparticle induced radiosensitization and it underlying mechanism. I hope to provide the readership with deeper understanding on the underlying mechanism beyond the mere observation of therapeutic effect from nanomedicine.

5.1 Introduction

Radiotherapy is a kind of therapy that has been proofed to be effective in clinics. However, local failure is often observed after irradiation as a result of intrinsic and acquired resistance to radiation treatment by tumor cells. As demonstrated by recent studies, radiation would affect cell adhesion to the extracellular matrix (ECM) by regulating the receptors presented on cell membrane (*e.g.*, integrins), in addition to the destruction of tumor cells.[1] Still, the damage caused by DNA damaging and apoptosis induction is often observed to have no significant selectivity in this approach.

As a well-studied biomarker, integrin is known to contain a single alpha and a single beta chain that can obtain either an activated or non-activated conformation. With the combination of 18 alpha subunits and 8 beta subunits over 24 kinds of mammalian integrin have been known till recently.[2] A substantial research revealed that integrins,

such as $\alpha_v\beta_3$, play a critical role in the regulation of tumor progression, metastasis, as well as angiogenesis.[3, 4] As a common biomarker in cancer, the expression of $\alpha_v\beta_3$ has been found to be up-regulated in a variety of cells, including human malignant melanoma, breast cancer, and advanced glioblastoma, on the surface of both endothelial cells as well as certain tumor cells.[4] In the context of radiotherapy, $\alpha_v\beta_3$ integrin has been found to direct associated with the tumor radiosensitivity,[5] and their acquired radioresistance after irradiation through the upregulation of their expression.[6, 7] Thus the theranostics targeting integrin $\alpha_v\beta_3$ has attracted particular interest, as this biomarker could be used for inhibition of angiogenesis while lowing the resistance.[3] As a specific ligand of integrin, RGD sequence is presented in many kinds of ECM protein allowing the adhesion of cells to ECM *via* integrin. It could also efficiently promote cell adhesion and particle attachment. Upon the binding of RGD to integrin, an integrin-mediated cell adhesion would be activated by the signal transduction between the ECM and cells, and further influence the cell behavior such as proliferation, differentiation, apoptosis, survival, and migration.[8] Aiming at the targeting of $\alpha_v\beta_3$ integrin, cyclic RGD-containing pentapeptides, have been widely studied as integrin inhibitor for enhanced radiotherapy of cancer.[9, 10]

Though RGD peptides is expected to be widely useful as processing radiosensitizer, it is still critical to maintain a low level of adverse side effects while increasing the treatment efficiency. An ideal radiosensitizer should also have the capability to be coupled to a drug delivery system for increased specificity. Recently, there is an emerging trend in the development of Au nanoparticle-based nanomedicine with increased targeting efficiency through RGD conjugation. These novel nanoparticle

platforms could also be integrated with ligands to cancer biomarkers and traditional anticancer drugs for enhanced targeting and therapeutic effect.[11] Among the various kinds of Au nanoparticle, Au nanorods have been extensively studied as therapeutic agents and drug delivery vehicles for the accurate detection and elimination of cancer.[12] After years of development, Au nanorods hold good biocompatibility, suitable physiochemical parameters, and can be prepared at large batch with high uniformity. With appropriate surface modification, Au nanorods may exhibit excellent tumor targeting capability and good penetration through biological barriers.[13, 14]

I would present our latest research on the clinical benefit of RGD-conjugated Au nanorods as effective radiosensitizer for the treatment of human melanoma. Possible mechanisms for the radiosensitization is also proposed and investigated. This research is hoped to bring new understanding to cancer biology and new hope to cancer patients.

5.2 Results

5.2.1 Cellular Toxicity and Uptake of RGD-Conjugated Au Nanorods

Au nanorods stabilized in CTAB were commercially purchased with an average length of 44.44 ± 4.7 nm and average width of 15.10 ± 1.7 nm Figure 5.1a. As the surface-coated CTAB holds high cytotoxicity and affects the further modification, a silica coating process was performed before further modification. The silica coating was conducted *via* a previously reported procedure to replace the surface capped CTAB.[15] The coating layer of silica was measured to have a thickness of *ca.* 31 nm under TEM (Figure 5.1b). The silica coated Au nanorods were further functioned with RGD peptides following a process previous reported.[16] The cell uptake experiment was conducted consequentially with

A375 melanoma cells to verify the cell uptake of RGD conjugated Au nanorods. After 1 h of incubation, RGD-conjugated Au nanorods were found both on the surface of cell membranes or in the cytoplasm as a result of integrin-receptor-mediated endocytosis (Figure 5.1c and d).[17, 18] The cell viability after the uptake of the RGD-conjugated Au nanorods was also assess with standard cell proliferation assay using MTT. As shown in Figure 5.2a, the cell viability of A375 cells showed a dose-dependent behavior, and the RGD-conjugated Au nanorods were slightly more toxic to cells than silica-coated Au nanorods ($P < 0.05$) at 48 h of incubation. The time-dependent cell proliferation assay was also conducted using 50 μg/mL RGD-conjugated Au nanorods or silica-coated Au nanorods for upto 48 h. No significant cytotoxicity was observed for both kinds of Au nanorods for upto 24 h (Figure 5.2b).

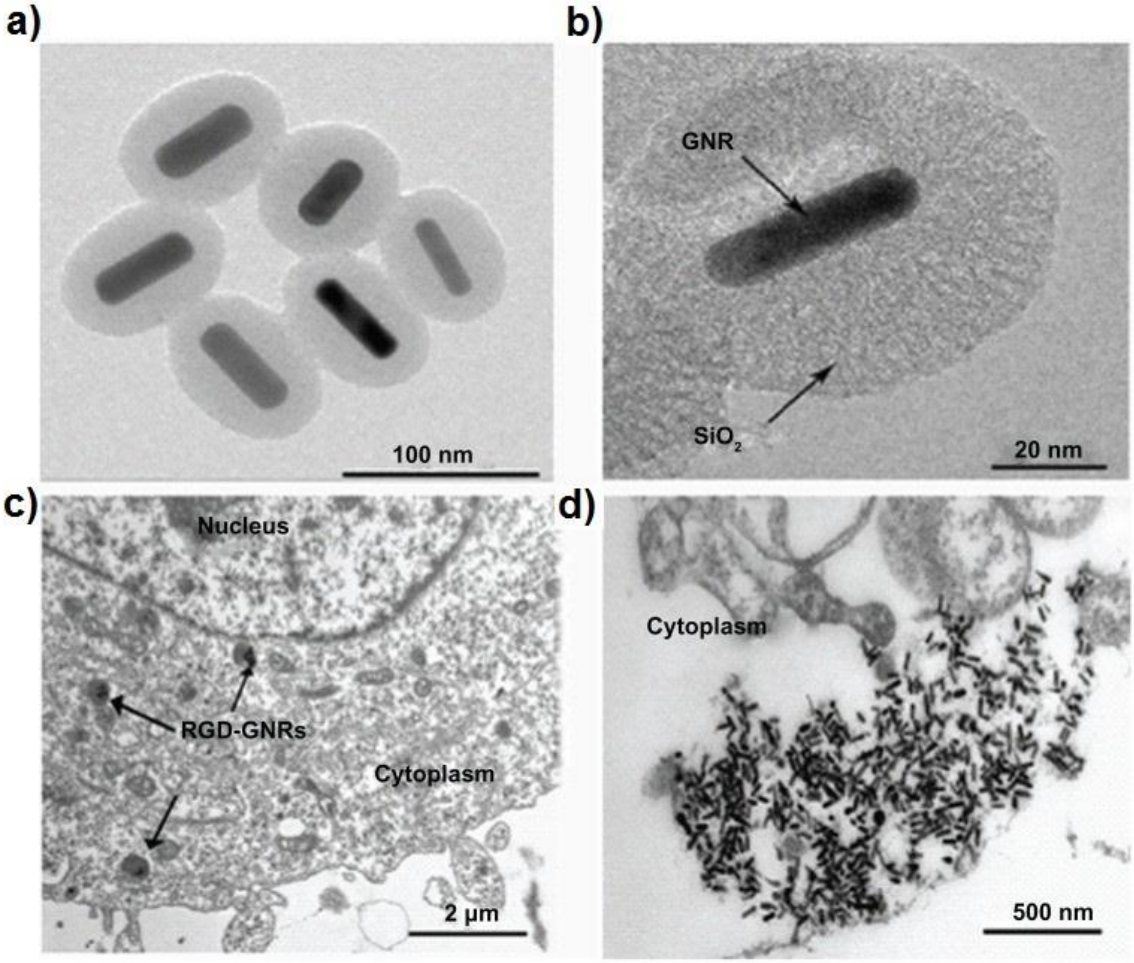

Figure 5.1. The morphology of as-prepared RGD-conjugated Au nanorods (shown as RGD-GNRs) and their cell uptake by A375 melanoma cells. (a) low magnification TEM image of RGD-conjugated Au nanorods. (b) high magnification TEM image of RGD-conjugated Au nanorods. The silica coating layer was measured to have a thickness of ca. 31 nm. (c and d) TEM images showing the A375 melanoma cells, showing the cell uptake of RGD-conjugated Au nanorods. The RGD-conjugated Au nanorods were mainly found in the cytoplasm.

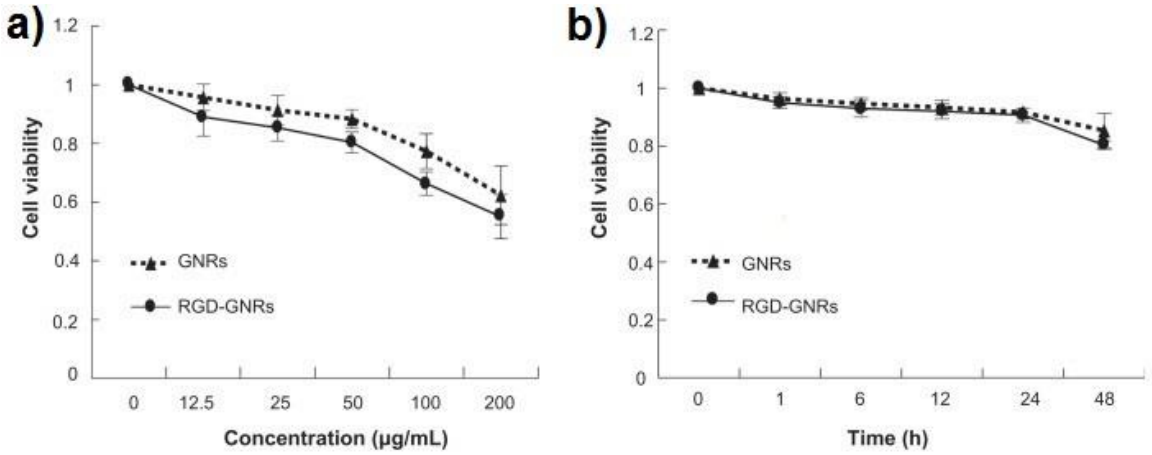

Figure 5.2. The cell proliferation assay using MTT. (a) The cell viability of A375 cells demonstrated a dose-dependent behavior with decreasing cell viability at high particle concentration. Data was collected and normalized to the control group (in absence of RGD-conjugated Au nanorods) at 48 hours. (b) The cell viability of A375 cells demonstrated a time-dependent behavior with decreasing cell viability at longer incubation times.

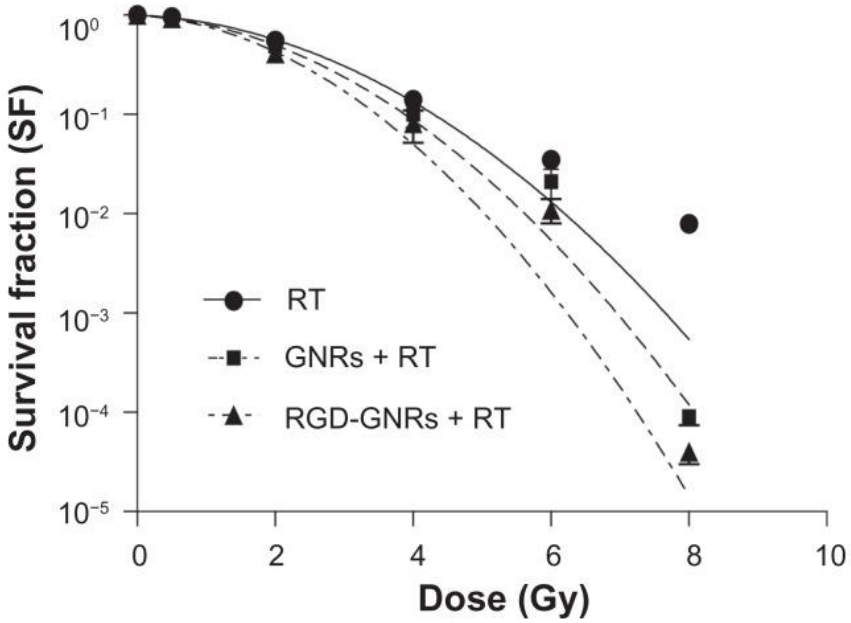

Figure 5.3. Radiosensitizing effect of silica-coated Au-nanorods or RGD-conjugated Au nanorods quantified by colony formation assay. A375 cells were treated with 50 μg/mL nanoparticles for 1 h prior to the irradiation. Colonies of >50 cells were counted at 2 weeks post treatment.

5.2.2 Radiosensitization of Melanoma Cells

To quantitatively compare the radiosensitizing effect of silica-coated Au nanorods and RGD-conjugated Au nanorods, a colony formation assay was employed to count the living cells at 2 weeks post treatment at 2 Gy. The survival rate of A375 cells was plotted and fitted to a dose-response curves as shown in Figure 5.3. A dose-modifying factor was derived for each kind of experimental condition with or without the addition of silica-coated Au nanorods or RGD-conjugated Au nanorods. Both silica-coated Au nanorods and RGD-conjugated Au nanorods demonstrated an enhancement in radiosensitivity of A375 cells to 6 MV X-rays with dose-modifying factor quantified as 1.14 and 1.35, respectively. In comparison to the control group, which had no nanoparticle, statistical significance was observed on both group with $P < 0.05$. From a one-way analysis of variance, the dose modification factor of RGD-conjugated Au nanorods was also significantly higher than that of the silica-coated Au nanorods and with $P = 0.001$.

5.2.3 Enhanced Radiation-induced Apoptosis

As shown in Figure 5.4, significant percentage of apoptosis cells were found from every treatment. However, the nanoparticles with or without RGD conjugation could not induce significant cell apoptosis in the absence of radiotherapy compared with the untreated control group ($2.23\% \pm 0.42\%$, $P < 0.05$). However, cells treated with both RGD-conjugated Au nanorods and radiation underwent significant cell apoptosis ($15.10\% \pm 0.96\%$), which is three and two times that from the groups treated with radiation or silica-coated Au nanorods and irradiation ($4.97\% \pm 0.83\%$ and $7.67\% \pm 0.31\%$, respectively).

5.2.4 Enhancement of Radiation-induced G_2 Cell Cycle Arrest

The radiosensitivity of tumor is also cell cycle-oriented, while cells in their G2/M typically holds higher radiosensitivity. As shown Figure 5.5, the treatment of silica-coated Au nanorods, RGD-conjugated Au nanorods, or radiation (6 MV X-rays,4 Gy) could elevated the percentage of cells arrested in their G_2/M phase (35% ± 2.65%, 36.14% ± 0.35%, and 40.9% ± 0.35%, respectively), in comparison with the control group (25.84% ± 0.49%; $P < 0.05$). The combination of irradiation and RGD-conjugated Au nanorods was also shown to further increase this percentage to 46.5% ± 1.2%. A statistical significance was observed with $P < 0.05$ between the group received irradiation after RGD-conjugated Au nanorods incubation and the and single treatment groups.

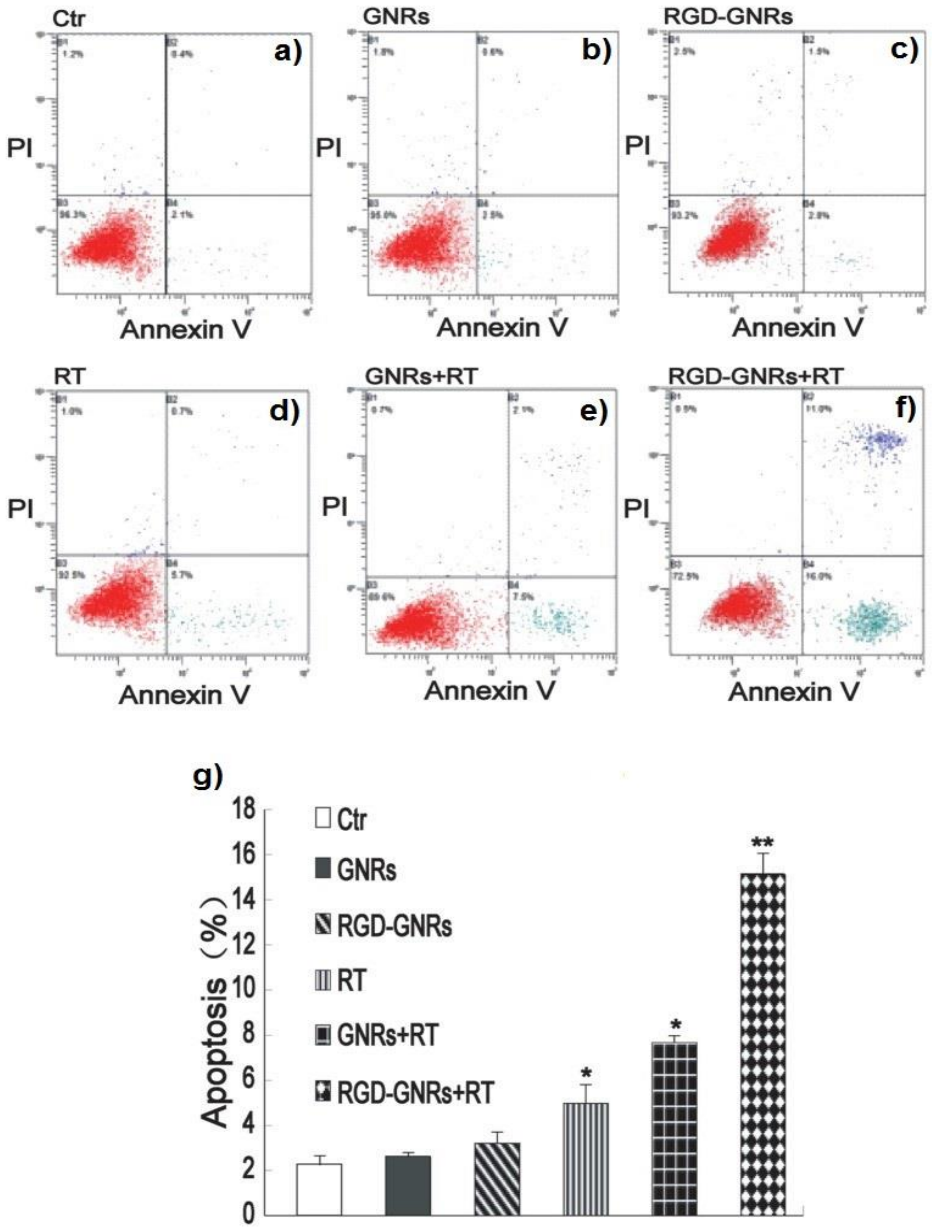

Figure 5.4. Enhancement of apoptosis by radiation and combined therapy with RGD-conjugated Au nanorods. A375 cells were incubated with either silica-coated Au nanorods or RGD-conjugated Au nanorods for 1 h prior to irradiation. The cells were quantified by flow cytometry with Annexin V and propidium iodide staining, at 24 h post treatment. (a–c) flow cytometry data showing the apoptosis in control cells and the cells containing either silica-coated Au nanorods and RGD-conjugated Au nanorods (50 μg/mL for 24 hours) without radiation. (d–f) flow cytometry data showing the apoptosis in cells receiving only irradiation or silica-coated Au nanorods and RGD-conjugated Au nanorods (50 μg/mL for 24 hours) prior to radiation. (g) Data from (a–f) presented in bar chart as the mean ± standard deviation (n = 3).

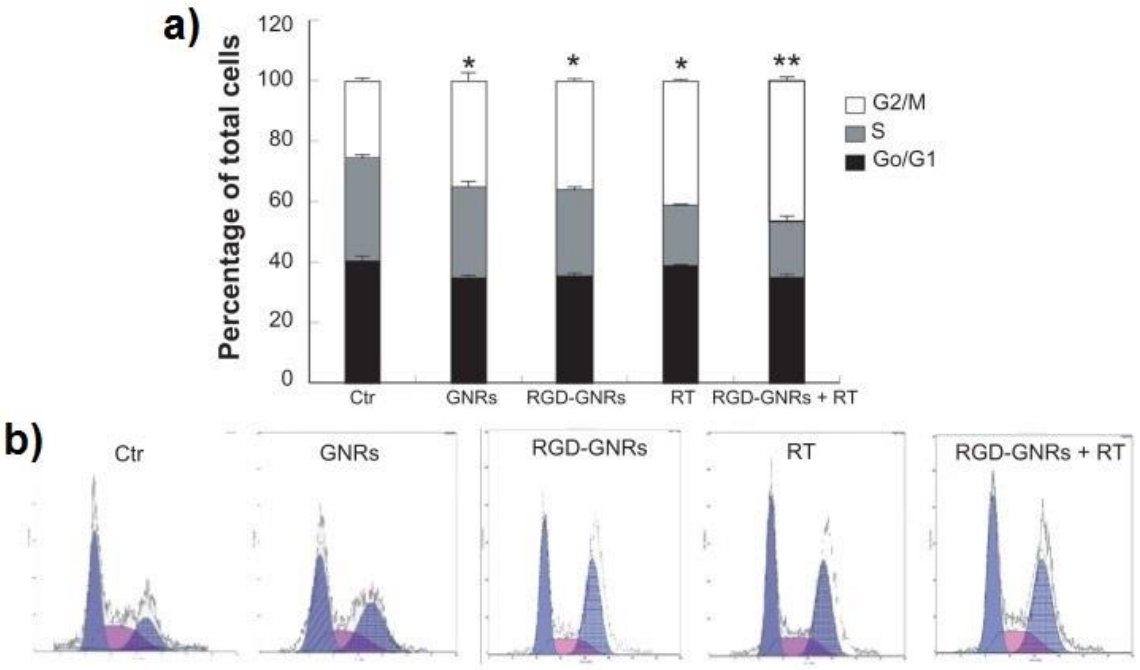

Figure 5.5 Enhancement of G_2/M cell cycle arrest induced radiosensitization in A375 cells. Flow cytometry were conducted at 24 h post irradiation to the A375 cells incubated with (ctr) DMEM, gold nanorods, silica-coated Au nanorods (50 μg/mL), or RGD-coated Au nanorods (50 μg/mL), without or with irradiation (6 MV X-rays with a dose of 4 Gy). (a) Percentage of different cell phases, presented in bar chart as the mean ± standard deviation (n = 3). (b) the corresponding flow cytometry data from (a).

5.2.5 Integrin $\alpha_v\beta_3$ Expression Levels

As a response to irradiation, the expression of $\alpha_v\beta_3$ integrin was found to be upregulated in a dose-dependent manner. As shown in Figure 5.6, RGD-conjugated Au nanorods could more effectively ($P < 0.05$) suppress the radiation induced expression of $\alpha_v\beta_3$ integrin relative to the silica-coated Au nanorods, which did not significantly affect the expression of $\alpha_v\beta_3$ integrin.

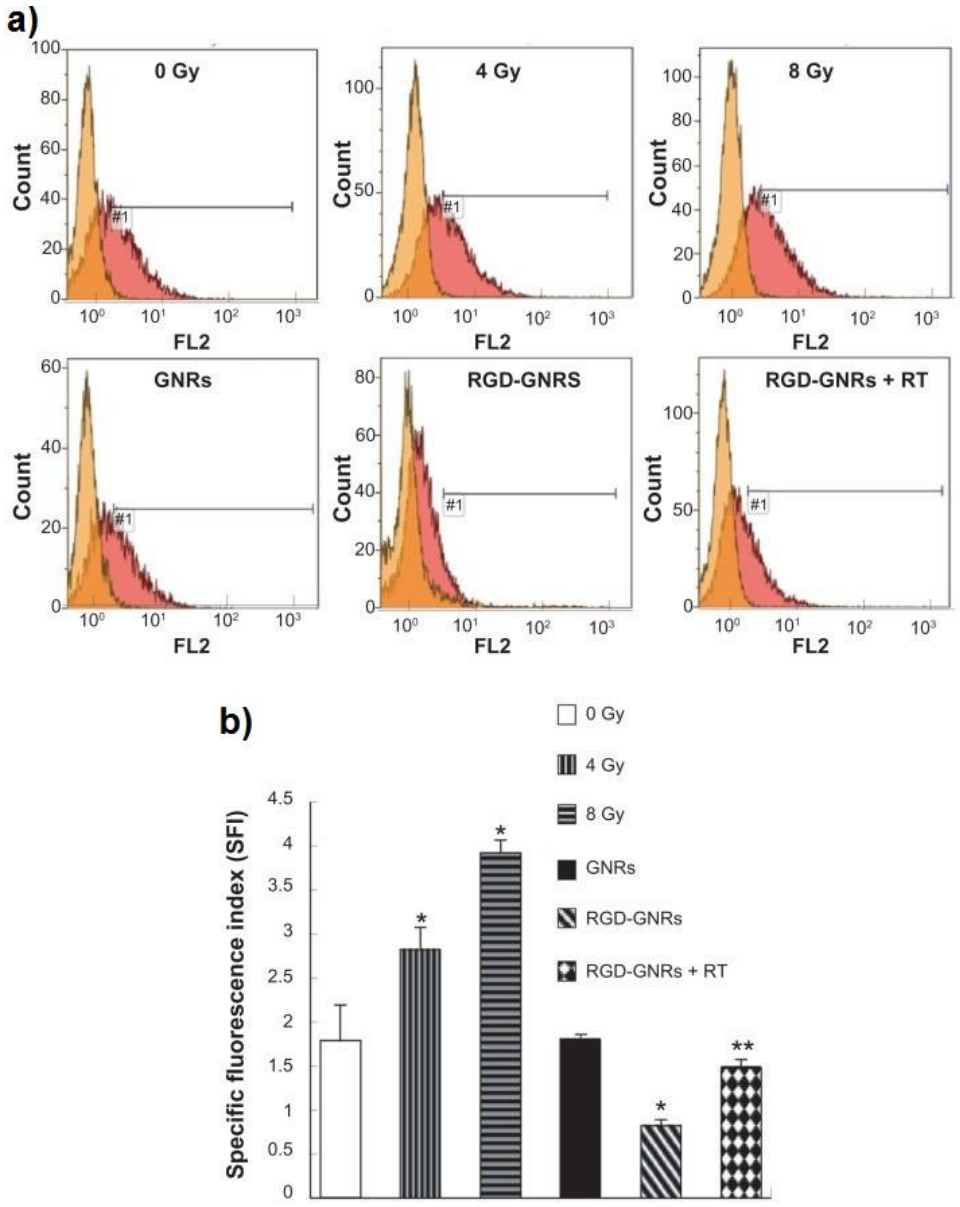

Figure 5.6. Suppression of expression level of $\alpha_v\beta_3$ integrin. (a) The flow cytometry data showing the expression level of $\alpha_v\beta_3$ integrin. The spontaneous and irradiation induced expression of $\alpha_v\beta_3$ integrin were suppressed by RGD-conjugated Au nanorods (50 µg/mL) upon irradiation. The cells were stained with anti-integrin $\alpha_v\beta_3$ antibody (LM609) or isotype-matched control antibody (DD7) at 24 h post treatment. (b) The expression level of $\alpha_v\beta_3$ was quantified with specific fluorescence intensity and plotted into bar chart as the mean ± standard deviation (n = 3).

5.3 Discussions

Human melanoma is well known to possess high degree of radioresistance that compromises treat effect. So the development of new radiosensitizer for improved treatment effect is of great interest and clinical benefit. In this current work, I presented the RGD-conjugated Au nanorods as novel radiosensitizers that can effectively target $\alpha_v\beta_3$ integrin.

As the capping agent and colloidal stabilizer, CTAB is typically needed for the wet chemistry synthesis of Au nanorods. However, their severe cytotoxicity could always be an issue in its biomedical application. One of the possible solution is to coat the surface of Au nanorods with silica through the chemical deposition. The surface modification strategy of silica coating has been reported to have low cytotoxicity with good colloidal stability, which is ideal for surface modification of Au nanorods.[20, 21] Along with the outstanding biocompatibility, silica was also reported to be easily modified for various surface properties. In that case, RGD peptides could be readily conjugated to the surface of silica-coated Au nanorods for improved targeting efficiency and internalization by cells. With the presence of RGD peptides, Au nanorods could be readily internalized *via* receptor-mediated endocytosis and be accumulated with in the endosomes. In that way, the treatment effect could be limited to the cancerous cells, leaving the healthy cells, except for endothelial cells, unaffected.[22]

In the present study, our results validated the internalization process through integrin $\alpha_v\beta_3$-receptor-mediated endocytosis. And the internalized RGD-conjugated Au nanorods could greatly enhance the treatment effect of radiotherapy with a dose

modification factor of 1.35. The use of RGD-coated Au nanorods was found to induce G_2/M arresting in A375 cells, and this enhancement could be added on top of the effect from radiation, giving out a higher percentage of cells arrested in their G_2/M phase. As the cancerous cells have been testified to have a higher radiosensitivity in their G_2/M phase than in the G0/G1 or S phase,[23] a increased radiation-induced cytotoxicity and therapeutic effect were observed from the group of cells receiving both RGD-coated Au nanorods and radiation. At the same time, the increased cells in their G_2/M phase could also explain the increase in vulnerability to radiation-induced DNA damage, as an increased expression of the DNA repair protein, γH2AX was recently found to be associated with radiotherapy.[24]

The radiosensitizing effect induced by the incubation of RGD-conjugated Au nanorods could also be explained by the inhibition of radiation induced $\alpha_v\beta_3$ integrin expression. In our experiment, A375 melanoma cells were found to have an upregulated expression of $\alpha_v\beta_3$ integrin after irradiation, comparing to their untreated counterparts. Through the flow cytometry data, an inhibition was found to the expression of $\alpha_v\beta_3$ integrin post treatment on the cells incubated with RGD-coated Au nanorods. It has been reported that a number of pathways in melanoma cells were closely associated with the resistance to radiation, one of which involves the activation of integrin. The integrin on the surface of cancerous cells could mediated the adhesion to ECM and the biding of growth factors that greatly impact the survival rate and radioresistance.[25] Integrin take effect through a pathway similar to the pathways triggered by growth factors.[26] Some research also showed a intimately interplay between $\alpha_v\beta_3$ and vascular endothelial growth factor receptor 2 on the activation of cellular response.[26, 27] The upregulation of vascular endothelial growth factor receptor 2 was also observed to induce a specific radioresistant effect in the $\alpha_v\beta_3$-

positive endothelial cells.[28] On the other hand, the upregulation of $\alpha_v\beta_3$ expression in response to irradiation could activate Akt, a key antiapoptic protein kinase, thus giving out a survival signal against radiation-induced destruction forming defense mechanism.[9] This helps to explain the acquired radioresistance of tumor cells after radiotherapy. The incubation of RGD-conjugated Au nanorods could inhibit the expression of $\alpha_v\beta_3$ integrin, and reduce the radioresistance after radiotherapy.

In addition to the improved therapeutic effect from the reducing of the radioresistance, RGD-conjugated Au nanorods could also minimize the adverse side effects to health tissue with their high selectivity to $\alpha_v\beta_3$ integrin. With the excellent targeting effect, the increased absorption of radiation energy could preferentially take effect in the cancerous cells when the RGD-conjugated Au nanorods were internalized.[24, 29] It has been realized that the introduction of material with high Z number could induce more photoelectron through the photoelectric effect causing more damage to the tissue with the resulted radicles.[30] Though the therapeutic effect was typically observed to be proportional to the dose of irradiaion, these results were mostly gathered from low-energy radiation as Au preferentially absorb kilovoltage X-rays. Megavoltage X-rays, which are widely used in clinics, are particularly suitable for the treatment of deep-seated tumors. And the radiosensitizing effect of megavoltage X-rays was a combination of multiple effect beyond just the Z number of material. In a recent study, Roa *et al* reported that the incorporated Au nanorods could affect the cell cycle of cancerous cells and facilitate the treatment.[31] This result is also in consistence with our observation. It is also proposed that the increased therapeutic effect of Au nanorods incorporation was the result of high level of intracellular reactive oxygen species, which are induced by irradiation and take effect

by elevating the level of oxidative stress.[32] An increased level of apoptosis could also be observed in consistent with the mechanism proposed as such. A recent work conducted in DNA plasmid models indicated that the sensitization was induced by the direct interaction between Au nanorods and megavoltage X-rays due to short-range electrons produced by the photoelectric effect.[24] The production of low-energy electrons and free radicals could cause more damage to DNA than the radiation alone. Our research validated the increased apoptosis and mitotic death in A375 cells, when the cancerous cells were incubated with RGD-conjugated Au nanorods.

In this chapter, I demonstrate the great potential of RGD-conjugated Au nanorods for the radiosensitization of cancerous cells on radiotherapy. Upon the irradiation of 6 MV x-ray, a dose-enhancement factor of 1.35 was observed on A375 melanoma cells. I further explored the underlying mechanism of the radiosensitization. It is revealed that the enhancement of treatment effect was mainly the result of cell cycle arresting on the G_2/M phase as well as the inhibition of radiation-induced $\alpha_v\beta_3$ integrin expression.

5.4 Experimental

5.4.1 Preparation of RGD-Conjugated Au Nanorods

The Au nanorods were commercially purchased from Sinopharm Chemical Reagent Co (Shanghai, China). The Au nanorods was stabilized in CTAB solution as they are prepared with the seed-mediated growth approach.[33, 34] The silica coating was then conducted *via* the hydrolysis and condensation of tetraethyl orthosilicate.[35] In a typical process, 20 mL of the stock solution containing Au nanorods was first centrifuged and redispersed into equal volume of ultrapure water (Millipore, Billerics, MA). After adjusting

the pH to 10–11, 1.1 mL of tetraethyl orthosilicate ethanol solution (10 mM, J & K Chemical Ltd, Shanghai, China) was introduced to 20 mL of the suspension containing Au nanorods. After 10 h of vigorous stirring at room temperature, a uniform silica coating layer of about 31 nm was found on the surface of the Au nanorod. Excess reactant was removed by centrifuge, in which the particles were washed with ultrapure water and ethanol for several times. The product was redispersed in ultrapure water before further modification. For the active targeting of $\alpha_v\beta_3$ integrin, cycle RGD peptides (Shanghai, China) were conjugated to the Au nanorods. Following the standard (1-Ethyl-3-(3-Dimethylaminopropyl)Carbodiimide Hydrochloride)/ N-Hydroxysuccinimide (EDC/NHS) reaction reported by Johnsson *et al*.[16] After 48 h of incubation, RGD-conjugated Au nanorods were washed by centrifugation at 6000 rpm for 15 minutes. The RGD-conjugated Au nanorods were then dispersed in DMEM (Hyclone, Carlsbad, CA) and stored at 4°C before further use.

5.4.2 Cell Lines and Culture

The A 375 human melanoma cells were obtained from the Shanghai Institute of Cell Biology and Chinese Academy of Sciences (Shanghai, China). Cell culture was conducted using DMEM supplement with 10% fetal bovine serum (Hyclone) at 37 °C in a humidified atmosphere containing 5 % CO_2.

5.4.3 TEM Analysis of Cells with Internalized Au Nanorods

For the preparation of cells for TEM imaging, A375 cells were washed three times with DPBS and fixed with 2.5% glutaraldehyde and 1% osmium tetroxide for 6 h and 2 h, respectively, after incubation with RGD-conjugated Au nanorods. Subsequentially, the

cells were dehydrated in ethanol, and embedded in agar resin (Agar Scientific, Stansted, Essex, UK). The sample was sections into slices of 60–70 nm thick and placed on copper grids. Lead citrate staining was also performed before visualized under TEM (Philips CM120).

5.4.4 Cellular Proliferation Assay

A standard MTT assay was performed to quantify the cytotoxicity of nanoparticles. In a typical experiment, A 375 melanoma cells were cultured in 96-well plate. Au nanorods with or without RGD conjugation was introduced at a series times to desired final concentration. Subsequentially, 15 μL of MTT stock solution (5 mg/mL; Sigma-Aldrich) was added to each wall and were allowed to incubate with the cells. After 4 h of incubation, the cells were then washed twice with DPBS. Then, 100 μL of DMSO (Sigma-Aldrich) was added to each wall to dissolve the formazan crystals. The absorbance at 570 nm were taken by plate reader and normalized to the untreated control group.

5.4.5 Irradiation

The radiotherapy was carried out by irradiating the cultured cells with 6 MV X-rays from linear accelerators (Siemens, Münich, Germany). During the treatment, the accelerator was set at a dose rate of 3 Gy/minute, with 1.5 cm bolus as compensator.

5.4.6 Clonogenic Assay

Prior to the irradiation, Au nanorods with or without RGD conjugation were added to the cells (5×10^5/well) in 6-well plate to a final concentration of 50 μg/mL. After 1 h of incubation, the nanoparticles were replaced with fresh DMEM and subjected to radiation

therapy under accelerator. The cells were digested and re-seeded into 6 wall culture plate which allowed the living cells to seed and grow into colonies. After another 2 weeks of culture, the living cells were stained with 0.4% crystal violet. Colonies with more than 50 cells were counted under fluorescent microscope for the calculation of the surviving fraction. The data was then fitted into a LQ model with Graphpad Prism software (version 5.0). Specifically, survival fraction at 2 Gy was used to quantify the radiosensitizing effect by calculating the dose-modifying factors.

5.4.7 Cell Cycle and Apoptosis Assays by Flow Cytometry

The sample for cell cycle analysis was prepared by fixing A375 cells (10^6 cells/mL) in 95% ethanol at −20 °C for 24 h, and stained with propidium iodide (50 μg/mL) in DPBS for 15 min at 4°C. Cellular DNA content was obtained using FACSCalibur flow cytometer (Becton-Dickinson, Franklin Lakes, NJ) and the cell cycle data was analyzed using multicycle system 2.0 software. In the apoptosis study, living cells were stained with Annexin-V-fluorescein isothiocyanate/propidium iodide (Invitrogen) before subjecting to flow cytometry measurement.

5.4.8 Integrin $\alpha_v\beta_3$ Analysis

A375 cells were stained with antihuman integrin $\alpha_v\beta_3$ mAb LM609 (Millipore, Shanghai, China) or isotype-matched control antibody DD7 (Millipore) before quantifiaction with flow cytometry. The staining was conducted by incubating mouse antihuman integrin $\alpha_v\beta_3$ mAb LM609 or isotype-matched control antibody DD7 with 200 μL DPBS suspension containing A375 cells (10^6 cells/mL) in the presence of 0.2% bovine serum albumin at 4 °C. After 45 min of incubation, the cells were washed three times with

DPBS and subject to flow cytometry (FACSCalibur) measurement. Fluorescence index were obtained by normalizing the mean fluorescence obtained with LM609 to that from the control group of DD7.[36]

5.4.9 Statistical Analysis

One-way analysis of variance was performed with SPSS statistical software (v13.0, SPSS Inc, Chicago, IL) to compare the means between two test groups. The test was set with a P value ≤ 0.05 for statistically significant.

5.5 References

[1] Nam, J-M.; Chung, Y.; Hsu, H.C.; Park, C.C. β_1 integrin targeting to enhance radiation therapy. *Int. J. Radiat. Biol.* **2009**, 85, 923–928.

[2] Hynes, R.O. Integrins: Bidirectional, Allosteric Signaling Machines. *Cell* **2002**, 110, 673–687.

[3] Hodivala-Dilke, K. $\alpha_v\beta_3$ integrin and angiogenesis: a moody integrin in a changing environment. *Curr. Opin. Cell Biol.* **2008**, 20, 514–519.

[4] Seftor, R.E.B. Role of the β_3 integrin subunit in human primary melanoma progression: multifunctional activities associated with $\alpha_v\beta_3$ integrin expression. *Am. J. Pathol.* **1998**, 153, 1347–1351.

[5] Monferran, S.; Skuli, N.; Delmas, C.; Favre, G.; Bonnet, J.; Cohen-Jonathan-Moyal E, *et al*. $\alpha_v\beta_3$ and $\alpha_v\beta_5$ integrins control glioma cell response to ionising radiation through ILK and RhoB. *Int. J. Cancer* **2008**, 123, 357–364.

[6] Wick, W.; Wick, A.; Schulz, J.B.; Dichgans, J.; Rodemann, H.P.; Weller, M. Prevention of irradiation-induced glioma cell invasion by temozolomide involves caspase 3 activity and cleavage of focal adhesion kinase. *Cancer Res.* **2002**, 62, 1915–1919.

[7] Hallahan, D.E.; Geng, L.; Cmelak, A.J.; Chakravarthy, A.B.; Martin, W.; Scarfone, C.; *et al*. Targeting drug delivery to radiation-induced neoantigens in tumor microvasculature. *J. Control. Release* **2001**, 74, 183–191.

[8] Makrilia, N.; Kollias, A.; Manolopoulos, L.; Syrigos, K.; Cell adhesion molecules: role and clinical significance in cancer. *Cancer Invest.* **2009**, 27, 1023–1037.

[9] Abdollahi, A.; Griggs, D.W.; Zieher, H.; Roth, A.; Lipson, K.E.; Saffrich, R.; *et al*. Inhibition of $\alpha_v\beta_3$ integrin survival signaling enhances antiangiogenic and antitumor effects of radiotherapy. *Clin. Cancer Res.* **2005**, 11, 6270–6279.

[10] Albert, J.M.; Cao, C.; Geng, L.; Leavitt, L.; Hallahan, D.E.; Lu, B. Integrin $\alpha_v\beta_3$ antagonist cilengitide enhances efficacy of radiotherapy in endothelial cell and non–small-cell lung cancer models. *Int. J. Radiat. Oncol.* **2006**, 65, 1536–1543.

[11] Peer, D.; Karp, J.M.; Hong, S.; Farokhzad, O.C.; Margalit, R.; Langer, R. Nanocarriers as an emerging platform for cancer therapy. *Nat. Nanotechnol.* **2007**, 2, 751–760.

[12] Wang, T.; Zhang, X.; Pan, Y.; Miao, X.; Su, Z.; Wang, C.; *et al*. Fabrication of doxorubicin functionalized gold nanorod probes for combined cancer imaging and drug delivery. *Dalton T.* **2011**, 40, 9789–9794.

[13] Chen, S.; Ji, Y.; Lian, Q.; Wen, Y.; Shen, H.; Jia, N. Gold nanorods coated with multilayer polyelectrolyte as intracellular delivery vector of antisense oligonucleotides. *Nano Biomed. Eng.* **2010**, 2, 15–23.

[14] Zhang, X.; Pan, B.; Wang, K.; Jing, R.; Bao, C.; Yang, H.; *et al*. Electrochemical property and cell toxicity of gold electrode modified by monolayer PAMAM encapsulated gold nanorods. *Nano Biomed. Eng.* **2010**, 2, 182–188.

[15] Dong, K.Y. A study of optothermal and cytotoxic properties of silica coated Au nanorods. *Mater. Lett.* **2011**, 65, 2319–2321.

[16] Bo, J.; Löfås, S.; Lindquist, G. Immobilization of proteins to a carboxymethyldextran-modified gold surface for biospecific interaction analysis in surface plasmon resonance sensors. *Anal. Biochem.* **1991**, 198, :268–277.

[17] Li, Z.; Huang, P.; Zhang, X.; Lin, J.; Yang, S.; Liu, B.; *et al*. RGD-conjugated dendrimer-modified gold nanorods for *in vivo* tumor targeting and photothermal therapy. *Mol. Pharm.* **2010**, 7, 94–104.

[18] Gormley, A.J.; Malugin, A.; Ray, A.; Robinson, R.; Ghandehari, H. Biological evaluation of RGDfK-gold nanorod conjugates for prostate cancer treatment. *J. Drug Target* **2011**, 19, 915–924.

[19] Xu, W.C.; Li, P.; Zhou, C.Q.; Cui, D.X.; Pang, B.; Ren, Q.S.; Fu, S. RGD-conjugated gold nanorods induce radiosensitization in melanoma cancer cells by downregulating $\alpha_v\beta_3$ expression. *Int. J. Nanomed.* **2012**, 7, 915-924.

[20] Tallury, P.; Payton, K.; Santra, S. Silica-based multimodal/multifunctional nanoparticles for bioimaging and biosensing applications. *Nanomedicine (Lond.)* 2008, 3, 579–592.

[21] Zhang, Q.; Qian J.; Li, X.; He, S. A study of mesoporous silica-encapsulated gold nanorods as enhanced light scattering probes for cancer cell imaging. *Nanotechnology* **2010**, 21, 055704.

[22] Ge, Y.; Kang, B. Surface plasmon resonance scattering and absorption of biofunctionalized gold nanoparticles for targeted cancer imaging and laser therapy. *Sci. China Technol.* **2011**, 54, 2358–2362.

[23] Sinclair, W.K. Cyclic x-ray responses in mammalian cells *in vitro*. *Radiat. Res.* **1968**, 33, AV112.

[24] Zheng, Y.; Hunting, D.J.; Ayotte, P.; Sanche, L. Radiosensitization of DNA by gold nanoparticles irradiated with high-energy electrons. *Radiat. Res.* **2008**, 169, 19–27.

[25] Cordes, N.; Meineke, V.; Integrin signalling and the cellular response to ionizing radiation. *J. Mol. Histol.* **2004**, 35, 327–337.

[26] Mahabeleshwar, G.H.; Feng, W.; Reddy, K.; Plow, E.F.; Byzova, T.V. Mechanisms of integrin–vascular endothelial growth factor receptor cross-activation in angiogenesis. *Circ. Res.* **2007**, 101, 570–580.

[27] Mahabeleshwar, G.H.; Feng, W.; Phillips, D.R.; Byzova, T.V. Integrin signaling is critical for pathological angiogenesis. *J. Exp. Med.* **2006**, 203, 2495–2507.

[28] Gorski, D.H.; Beckett, M.A.; Jaskowiak, N.T.; Calvin, D.P.; Mauceri, H.J.; Salloum, R.M.; *et al*. Blockade of the vascular endothelial growth factor stress response increases the antitumor effects of ionizing radiation. *Cancer Res.* **1999**, 59, 3374–3378.

[29] Chen, W.; Zhang, J. Using nanoparticles to enable simultaneous radiation and photodynamic therapies for cancer treatment. *J Nanosci Nanotechnol* **2006**, 6, 1159–1166.

[30] Spiers, F.W. The influence of energy absorption and electron range on dosage in irradiated bone. *Br. J. Radiol.* **1949**, 22, 521–533.

[31] Wilson, R.; Xiaojing, Z.; Linghong, G.; Andrew, S.; Xiuying, H.; Yeping, X.; *et al*. Gold nanoparticle sensitize radiotherapy of prostate cancer cells by regulation of the cell cycle. *Nanotechnology* **2009**, 20, 375101.

[32] Geng, F.; Song, K.; Xing, J.Z.; Yuan, C., Yan, S.; Yang, Q.; *et al*. Thio-glucose bound gold nanoparticles enhance radio-cytotoxic targeting of ovarian cancer. *Nanotechnology* **2011**, 22, 285101.

[33] Pan, B.; Ao, L.; Gao, F.; Tian, H.; He, R.; Cui, D. End-to-end self-assembly and colorimetric characterization of gold nanorods and nanospheres *via* oligonucleotide hybridization. *Nanotechnology* **2005**, 16, 1776–1780.

[34] Murphy, C.J.; Jana, N.R. Controlling the Aspect Ratio of Inorganic Nanorods and Nanowires. *Adv. Mater.* **2002**, 14, 80–82.

[35] Li, X.; Kao, F.J.; Chuang, C.C.; He, S. Enhancing fluorescence of quantum dots by silica-coated gold nanorods under one- and two-photon excitation. *Opt. Exp.* **2010**, 18, 11335–11346.

[36] Wiendl, H.; Mitsdoerffer, M.; Hofmeister, V.; Wischhusen, J.; Bornemann, A.; Meyermann, R.; *et al*. A Functional role of HLA-G expression in human gliomas: an alternative strategy of immune escape. *J. Immunol.* **2002**, 168, 4772–4780.

CHAPTER 6. SUMMARY AND FUTURE DIRECTIONS

6.1 Summary

In this dissertation, I explored the potential of using engineered Au nanoparticles with novel morphology and active targeting capabilities as theranostic agents for molecular imaging and cancer therapy. Various modifications were made to the nanoparticles and radiolabeling chemistry aiming to improve the functionality in their niche applications. These works improved the current understanding to cancer nanomedicine by inventing new kinds of nanomaterials, using new radio isotopes for molecular imaging, as well as developing new methodology for radiolabeling and biomedical assays. To summarize, I conclude the dissertation by highlighting the innovation and potential impact of the research works presented in this dissertation.

The whole work presented in this dissertation was dedicated to the integration of molecular imaging technology and the latest nano-chemistry with innovation on four aspects:

1) Developed new kinds of Au nanoparticles with well controlled tripod morphology (chapter 2 and 3): In these researches I prepared the PdCu tripods as the templets to grow PdCu@Au tripods with uniform size and morphology. This novel kind of nanoparticle possess merits like tunable LSPR peak, large absorption to extinction ratio, large two-photon luminescence cross section. The merits of Au nanoparticles are often associated with the anisotropic structure. According to the current research, the anisotropic growth of nanoparticle is hard to induce and control. Though the approach to fabricate Au nanoparticles of anisotropic morphologies with the help of templet materials has already been demonstrated, this technique is still restricted by the limited choices of templet materials. As the number of arms on Au

nanoparticles can hardly be controlled, the tripod shaped nanoparticles were seldomly reported but of great interest to biomedical applications.

2) For the first time, introduced Au-199 as a novel medical isotope for SPECT imaging (chapter 4): The imaging qualities of current nuclear imaging technologies are largely affected by the physical properties of the medical isotopes. Either the choice of technology, resolution limit, dosage preparation, treatment procedure, as well as the associated side effects are all closely related to the medical isotopes. I demonstrated the use of Au-199 as novel SPECT isotope with the tumor bearing animal model under the exist settings on commercial SPECT. The corresponding radiolabeling technique was also developed for Au-199 with good stability. The introduction of a new medical isotope would open up new possibilities to develop better radioactive tracer for improved imaging quality and radio safety.

3) Improved the radio labeling technology by incorporating radioactive isotopes (Cu-64, Au-199) into the lattice of nanoparticles (chapter 2 and 4): I demonstrated the chemistry to fix isotopes like Cu-64, Au-199 into the lattice of PdCu@Au tripods and Au nanospheres respectively. By incorporating radioactive isotopes into the lattice of Au nanoparticles, the labeling stability could be elevated. This technology does not require the use of additional reagents and will not cause undesired changes to the properties of nanoparticles. In comparison, the current radioactive labeling technology typically requires the use of chelating agents or specially designed chemistry to bond isotopes to the surface of nanoparticles. However, the binding stability of isotopes is always an issue resulting in high background noise and biased biodistribution profiles. With the conjugation of chelating agents, the designed surface properties of nanoparticles would also be altered. Thus, the new radiolabeling technology demonstrated superior potential for the application in molecular imaging.

4) Developed new targeting technology for improved biodistribution of nanoparticles (chapter 2, 4): This research established a new cancer biomarker and the corresponding targeting technology for the *in vivo* targeting of triple negative breast cancer. I demonstrated that CCR5 could be employed as biomarkers to target triple negative breast cancer with DAPTA peptide-conjugated Au nanoparticles *in vivo*.

Our works developed new materials with novel properties and targeting technology that can help to better understand the biology of cancer, improving the diagnosis and therapy. The successful completion of these researches would have the following impacts:

1) Provide a better understanding to the biology of cancer (chapter 5): Radiotherapy is one of the primary approaches in clinical cancer therapy. However, as a result of the poor selectivity between health tissue and cancer lesion as well as the adverse side effect, the therapeutic effect of radiotherapy is often limited. The means of sensitizing cancer cells to radiation and lowering the dose requirement is still under research. The RGD peptide-conjugated Au nanorods developed in this dissertation could effectively sensitize the human melanoma cells by downregulating the expression of radiation-induced $\alpha_v\beta_3$ and increasing the arresting of cells in G_2/M phase. The important role of radiation-induced $\alpha_v\beta_3$ expression was also testified. With this research, $\alpha_v\beta_3$ integrin was verified to be an effective therapeutic target in radiotherapy, in addition to its role of tumor angiogenesis biomarker currently understands by scientist.

2) PdCu@Au tripods could serve as a new platform for wider application in cancer theranostics with their novel tripod structure and excellent optical properties (chapter 2 and 3): The development of nanoparticles with tripod structure could bring new possibilities to the *in vivo* application for improved biodistribution. And with the newly developed

morphology, PdCu@Au tripods were found to exhibit outstanding optical properties like readily tunable LSPR peaks in NIR region, bright two-photon luminescence that could be utilized in both cancer diagnostics at *in vitro* and *in vivo* level. With their large absorption cross section facilitating the photothermal generation, PdCu@Au tripods could serve as the nano-transducer to treat cancer with photothermal therapy. With these properties, PdCu@Au tripods possess the capability to be a versatile platform for various biomedical applications.

6.2 Future Directions

This dissertation was dedicated to the integration of molecular imaging technology and the latest nano-chemistry with focuses on nanoparticle engineering, incorporation of novel isotope, as well as the development of new tumor targeting technology. Work accomplished in this dissertation made important progresses towards the ultimate goal of clinical application using Au nanoparticle for cancer theranostics. To achieve this goal, plenty of effort still needs to be devoted.

One of the future direction is to increase the clinical benefit of Au nanoparticle by the integration of more theranostic functions. As the decision of whether to put a nanomedicine into clinical use has essentially become a tradeoff between the clinical benefit and the side effect, we combine the clinical benefit of individual diagnostic and therapeutic modalities by integrating these capabilities into one single kind of Au nanoparticle. The further integration could follow the same strategy demonstrated in this work to put nuclear imaging modalities (PET, SPECT), photo-luminescence (fluorescence imaging, two-photon luminescence imaging), photoacoustic generation, and photothermal generation capabilities onto the same platform. As such we could achieve more clinical benefit with the same injected dose. At the meantime, with the help of multi-modality imaging we could also

monitor multiple cancer biomarkers simultaneously. It is expected to provide us with a comprehensive understanding to cancer biology.

Another direction is to improve the biodegradability of Au nanoparticles by modification and innovation on the nanoparticle synthesis. Though the good short-term biocompatibility and stability of Au nanoparticles have widely been demonstrated. The study on their long-term stability and toxicity is still missing. Their fate in biological system and final elimination from body is still uncertain. This uncertainty greatly hampers the application of Au nanoparticles in clinical trials. At this point, the good stability of Au becomes a unfavorable factor that compromise the biodegradability. Possible solutions should trace back to the initial design and fabrication of Au nanoparticle. Here we highlight two potential approaches in the following context with the hope to extend the works in this dissertation.

In one approach, Au nanoparticles could be synthesized as alloyed particles for better degradability. The degradation of other metal contents could cause the dealloy of metal contents breaking the integrity of nanoparticles. In a recent research, Liu and co-workers reported the synthesis of Cu-64 doped CuAu alloyed nanoparticles, and demonstrated their PET imaging capability as well as the high clearance.[1] The as prepared CuAu alloyed nanoparticle has a large Cu contents, which is tunable by varying the feeding ratio of different contents, of upto 80%. At 48 h postinjection, upto 38.4% of the injected dose were observed in the feces for the PEG (MW $\approx$ 1000) coated Au nanoparticles, demonstrated the existence of high hepatobiliary clearance. It is known that hepatocyte is the type of cell that is responsible for the clearance of Cu^{2+} and the biliary excretion.[2] The clearance of CuAu nanoparticles is most likely the result of hepatocytes uptake. It is also

reasonable to assume that the nanoparticles have lost their structural integrity after being processed by the hepatocytes, as a large portion of the Cu contents are excreted.

Another alternative approach is to assemble large nanoparticles from small Au nanoparticles or Au clusters, to allow the final clearance through the renal clearance process. In a recent work, Chan and co-workers reported the assemble of nanoparticles with the help of DNA linkers.[3] Recently our group also developed the technology to encapsulate phase-change material (PCM), *e*.g. stearic acid, tridecanoic acid. The florescent Au clusters could maintain their florescent property after the encapsulation. This novel kind of nanoparticle is expected to be biodegradable and clearable as the Au clusters possess the capability to be processed by renal clearance.

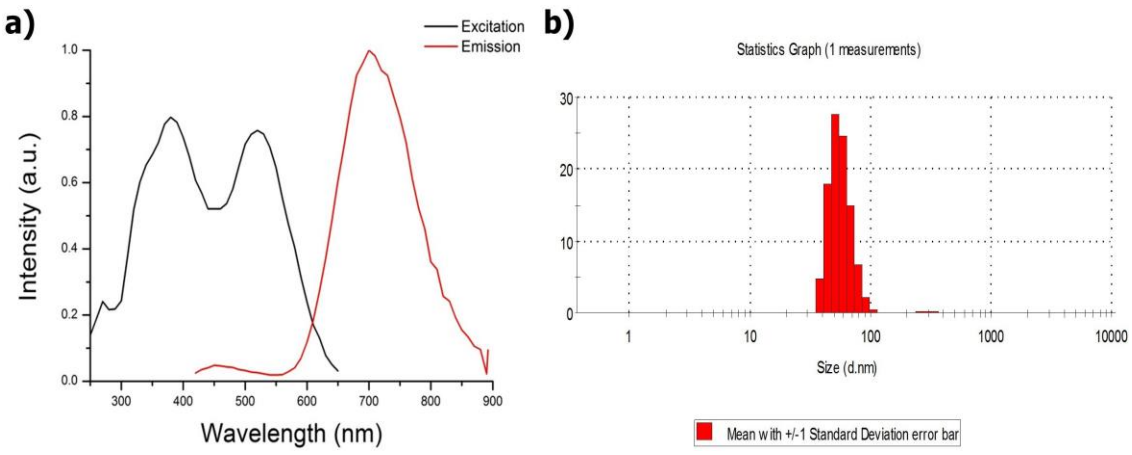

Figure 6.1 a) the fluorescence spectra of Au cluster enveloped PCM nanoparticles; b) the size distribution of Au cluster enveloped PCM nanoparticles measured by dynamic light scattering.

Following these directions, Au nanoparticle could obtain more merits with less side effects. And their clinical benefit could outweigh the side effects making them clinical viable as nanomedicine. The successful development of Au nanoparticle-based nanomedicine is expected to bring breakthroughs to the next generation cancer medicine.

6.3 References

[1] Zhao, Y.; Sultan, D.; Detering, L.; Luehmann, H.; Liu, Y. Facile synthesis, pharmacokinetic and systemic clearance evaluation, and positron emission tomography cancer imaging of ^{64}Cu-Au alloy nanoclusters. *Nanoscale* **2014**, 6, 13501–13509.

[2] Souza, F.S.D.; Botelho, M.C.S.N.; Lisbôa, R.S. Hepatology: hepatology principles and practice: history, morphology, biochemistry, diagnostics, clinic, therapy. *JAMA* **2002**, 288, 389-390.

[3] Chou, L.Y.T.; Zagorovsky, K.; Chan, W.C.W. DNA assembly of nanoparticle superstructures for controlled biological delivery and elimination. *Nat. Nanotechnol.* **2014**, 9, 148–155.

APPENDIX A. COPYRIGHT INFORMATION

Chapter 1; Figures 1.1 b and c:

Reprinted (adapted) with permission from Ref. 9. Copyright 2013 John Wiley and Sons.

Chapter 1; Figures 1.1d:

Reprinted (adapted) with permission from Ref. 16. Copyright 2009 American Chemical Society.

Chapter 1; Figures 1.1f:

Reprinted (adapted) with permission from Ref. 10. Copyright 2010 John Wiley and Sons.

Chapter 1; Figures 1.1g:

Reprinted (adapted) with permission from Ref. 13. Copyright 2006 American Chemical Society.

Chapter 1; Figures 1.1 h, l and p:

Reprinted (adapted) with permission from Ref. 17. Copyright 2006 Royal Society of Chemistry.

Chapter 1; Figures 1.1i:

Reprinted (adapted) with permission from Ref. 8. Copyright 2011 Royal Society of Chemistry.

Chapter 1; Figures 1.1j:

Reprinted (adapted) with permission from Ref. 11. Copyright 2007 American Chemical Society.

Chapter 1; Figures 1.1k:

Reprinted (adapted) with permission from Ref. 14. Copyright 2003 Annual Reviews.

Chapter 1; Figures 1.1n:

Reprinted (adapted) with permission from Ref. 12. Copyright 2010 Royal Society of Chemistry.

Chapter 1; Figures 1.1o:

Reprinted (adapted) with permission from Ref. 15. Copyright 2007 Nature Publishing Group.

Chapter 1; Figures 1.2:

Reprinted (adapted) with permission from Ref. 32. Copyright 2013 American Chemical Society.

Chapter 1; Figures 1.3:

Reprinted (adapted) with permission from Ref. 37. Copyright 2012 American Chemical Society.

Chapter 1; Figures 2.1-2.14:

Reprinted (adapted) with permission from Ref. 28. Copyright 2016 American Chemical Society.

Chapter 1; Figures 3.4:

Reprinted (adapted) with permission from Ref. 3. Copyright 2014 American Chemical Society.

Chapter 1; Figures 4.1-4.7:

Reprinted (adapted) with permission from Ref. 34. Copyright 2016 John Wiley and Sons.

Chapter 1; Figures 5.1-5.6:

Reprinted (adapted) with permission from Ref. 19. Copyright 2006 Dove Medical Press Ltd.

VITA

BO PANG

Pang was born in Beijing, China. He received his B.E. in mechanical engineering from College of Engineering of Peking University in 2010, and his B.S. in chemistry from College of Chemistry and Molecular Engineering of Peking University in 2011. He then pursued his Ph.D. degree in biomedical engineering in the joint Ph.D. program by Georgia Institute of Technology, Emory University, and Peking University under the supervision of Profs. Qiushi Ren and Younan Xia. His research interests focus on the use of gold nanoparticles for cancer therapy and nanoparticle-based contrast agents for molecular imaging. In spare time, he enjoys cooking, traveling, fencing, skiing, and squash.